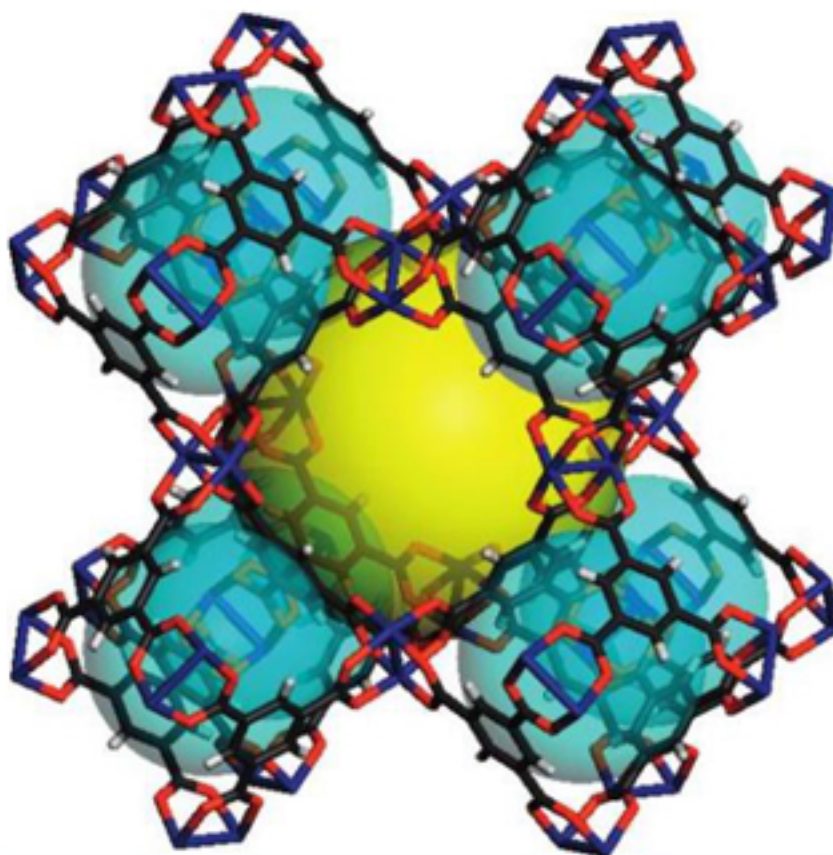


SCIENTIA BRUNEIANA



OFFICIAL JOURNAL OF
THE FACULTY OF SCIENCE
UNIVERSITI BRUNEI DARUSSALAM



ISSN : 1819 - 9550 (Print), 2519 - 9498 (Online) - Volume : 18(2), 2019

SCIENTIA BRUNEIANA

A journal of science and science-related matters published twice a year (January-June and July-December) by the Faculty of Science, University Brunei Darussalam. Contributions are welcomed in any area of science, mathematics, medicine or technology. Authors are invited to submit manuscripts to the editor or any other member of the Editorial Board. Further information including instructions for authors can be found in the Notes to Contributors section (the last three pages).

EDITORIAL TEAM

Editors-in-Chief

Professor David John Marshall, Universiti Brunei Darussalam, Brunei Darussalam
Professor Robert Hall, Royal Holloway University of London, United Kingdom

Managing Editor

Dr Malcolm Ringland Anderson, Universiti Brunei Darussalam, Brunei Darussalam

Production Editor

Dr Owais Ahmed Malik, Universiti Brunei Darussalam, Brunei Darussalam

Associate Editors

Associate Professor Minhaz Uddin Ahmed, Universiti Brunei Darussalam, Brunei Darussalam
Associate Professor Mohammad Mansoob, Universiti Brunei Darussalam, Brunei Darussalam
Associate Professor Monowarul Mobin Siddique, Universiti Brunei Darussalam, Brunei Darussalam
Associate Professor Akira Kinjo, Universiti Brunei Darussalam, Brunei Darussalam
Dr Md Aminul Islam, Universiti Brunei Darussalam, Brunei Darussalam
Dr Daphne Teck Ching Lai, Universiti Brunei Darussalam, Brunei Darussalam
Dr James Robert Jennings, Universiti Brunei Darussalam, Brunei Darussalam

Editorial Board

Dr Lee Hoon Lim, Universiti Brunei Darussalam, Brunei Darussalam
Associate Professor Basilios Tsikouras, Universiti Brunei Darussalam, Brunei Darussalam
Professor Serban Proches, University of Kwa-Zulu Natal, South Africa
Professor Michael Yu Wang, Hong Kong University of Science and Technology, Hong Kong
Professor David Young, University of Sunshine Coast, Australia
Professor Roger Hosking, University of Adelaide, Australia
Professor Rahmatullah Imon, Ball State University, United States
Professor Jose Rajan, Universiti Malaysia Pahang, Malaysia
Associate Professor Vengatesen Thiyagarajan, University of Hong Kong, Hong Kong
Dr Hartini Yasin, Universiti Brunei Darussalam, Brunei Darussalam

SCIENTIA BRUNEIANA is published by the Faculty of Science,
Universiti Brunei Darussalam, Brunei Darussalam BE 1410

ISSN 2519-9498 (Online), ISSN 1819-9550 (Print)
1. Research – Brunei Darussalam. 2. Science – Brunei Darussalam
Q180.B7 B788 2019

SCIENTIA BRUNEIANA

Publication Ethics Policy

The Editorial Board of *Scientia Bruneiana* is committed to implementing and maintaining the publication standards of a high-quality peer-reviewed scientific journal.

Each manuscript submitted to *Scientia Bruneiana* is examined by a referee with recognised expertise in the manuscript's subject area, and all communications between the referee and the author(s) must first pass through the Editorial Board, so that the identity of the referee remains confidential.

No one will be appointed as the referee of a manuscript if he or she is known to have a potentially compromising relationship with one or more of the authors of the manuscript, as for example in being related through blood or marriage to an author, or in being the research supervisor or research student of an author.

The Editorial Board of *Scientia Bruneiana* makes every effort to ensure that each paper published in the journal is free of plagiarism, redundant or recycled text, and fabricated or misrepresented data. Where possible, plagiarism detection software will be used to check for plagiarised or recycled text.

Provided that a manuscript is free of the ethical lapses described in the previous paragraph, the decision to publish it in *Scientia Bruneiana* is based entirely on its scientific or academic merit, as judged by the referee. The referee's assessment of the merit of the manuscript is final. While a full statement of the reasons behind the referee's decision will be passed on to the author(s), no appeals from the author(s) will be entertained.

Under no circumstances will the referee of a paper published in *Scientia Bruneiana* be credited as one of the authors of the paper, and other papers that have been authored or co-authored by the referee will be admitted to the paper's list of references only after an independent third party with expertise in the area has been consulted to ensure that the citation is of central relevance to the paper.

If a member of the Editorial Board of *Scientia Bruneiana* is listed as an author of a manuscript submitted to *Scientia Bruneiana*, that Board member will play no part whatsoever in the processing of the manuscript.

Where necessary, any corrections or retractions of papers previously published in *Scientia Bruneiana* will be printed in the earliest possible edition of the journal, once the need for a correction or retraction has been drawn to the attention of the Editorial Board.

SCIENTIA BRUNEIANA VOL. 18, NO. 2

2019

Table of Contents	Page Numbers
Petrography of aggregates in Luzon, Philippines: Identification of components and deleterious materials by Maria Ines Rosana Balangue-Tarriela, Cleodette L. Lagata, Raymond G. Leuterio and Ma. Lourdes Caluen-Abad	1
Reconnaissance geochemical and geophysical exploration for gold at Iri gold field, north central Nigeria by Sidi Aliyu Ahmed, Nuhu Musa Waziri, Hadiza Liman Mohammad, Mohammed Abubakar Mohammed and Apeh Aromeh Gideon	19
Partitioning of iron and zinc in the catchment alluvial sediments of the River Gbako flood plains around Baddegi, central Bida basin, Nigeria by Sidi Aliyu Ahmed, Nuhu Musa Waziri, Hadiza Liman Mohammad and Mohammed Abubakar Mohammed	32
Different synthetic approaches, designs and applications of metal-organic frameworks with selected organic ligands by Ubaidullah Hj. Mat Yassin, Malai Haniti Sheikh Abdul Hamid, Zainab Ngaini and Ai Ling Tan	40

Petrography of aggregates in Luzon, Philippines: Identification of components and deleterious materials

Maria Ines Rosana Balangue-Tarriela, Cleodette L. Lagata,
Raymond G. Leuterio and Ma. Lourdes Caluen-Abad*

*National Institute of Geological Sciences, College of Science, University of the Philippines,
Diliman, Quezon City, 1101 Philippines*

**corresponding author email: mdbalanguetarriela@up.edu.ph*

Abstract

Petrography is one of a series of standard tests used to assess an aggregate's components, mechanical qualities, durability, chemical stability, and alkali reactivity. In this study, aggregate materials were collected from rock exposures and/or alluvial deposits from four areas near Metro Manila, Philippines: Bulacan, Rizal, Pampanga, and Zambales. Transmitted light microscopy was conducted to identify rock types and characterise physical and chemical properties that may present potential problems when used as aggregate materials. The results show that the aggregates vary in terms of rock types and alteration type. Samples from Bulacan are mostly porphyritic basalt and fine to coarse-grained sandstone with veinlets of silica and carbonate. The presence of cavities and microfractures caused mainly by vesicles from the volcanic rocks was also observed. Rizal aggregates are composed predominantly of chloritized basalts and andesites with minor clastic rocks and tuffs. The aggregates from Zambales are products of erosion of the Zambales Ophiolite, mixed with the lahar deposits from the Pinatubo eruption. On the other hand, Pampanga aggregates are mostly lahar deposits, containing pumice, a poor choice for aggregate composition due to its low hardness, brittleness and vesiculated texture. Aside from the lithological classification, potentially alkali-reactive constituents were also observed in selected samples from the four sampling areas.

Index Terms: aggregates; Luzon; petrography

1. Introduction

The Philippine government has launched a "Build, build, build", program which aims to enhance the infrastructure of the country, leading to more robust economic development. The key projects under the programme include railways, industrial parts, energy facilities, water resource and flood control projects. These are considered massive construction projects, which will require high quality raw materials, especially aggregates.

Aggregate is any granular material, such as sand, gravel, crushed stone, or iron-blast furnace slag. It is combined with asphalt cement or Portland cement to form asphalt concrete or cement concrete, respectively, and is used in subbases and bases of roadway structure, drainage

structures and concrete blocks. The quality of aggregates significantly affects the properties of concrete since it constitutes about 70%-80% of the volume of the concrete¹ and is therefore controlled based on a series of standard tests. Through these tests, the aggregates' compositional, textural and structural characteristics will be assessed to provide data on their mechanical performance, durability, chemical stability, alkali reactivity, and harmful substance content.

One of the standard tests used in the assessment is petrography, or the use of microscopic examination of thin section of rocks, basically for rock identification, description and classification. Petrography provides useful information for

understanding the physico-mechanical properties of the rocks being used as aggregates. These properties depend on the degree of alteration and deformation as well as other petrographic characteristics, such as the mineralogical composition, texture, size, shape and arrangement of the mineral grains, the nature of the grains' contacts and the degree of grain interlocking, of the source rock¹. Knowledge of the relations between petrography and aggregate properties is important to ensure strength and durability of the finished product. As mentioned by Bérubé², concrete aggregates must generally satisfy a number of specifications:

- a. Mechanical performance: Resistance to fragmentation, abrasion, and polishing
- b. Durability: Resistance to environmental conditions, particularly freezing/thawing cycles
- c. Chemical stability: Resistance to any deleterious reaction (e.g., dissolution, sulfation)
- d. Alkali-aggregate reactivity: Reaction with the highly basic and alkaline concrete pore solution

- e. Harmful substances: Soft and friable particles, organic matter, low-density matter
- f. Particle shape and surface texture: Sphericity and angularity, toughness and alteration
- g. Particle size distribution: Grain size and proportion of fines (% < 80 mm)
- h. Other useful (for concrete proportioning) or specified properties (for special uses): surface moisture, water content, absorptivity, specific gravity, bulk density, and percentage of voids

In this paper, petrographic assessment of aggregates collected from four provinces in the Philippines: Bulacan, Rizal, Pampanga, and Zambales will be presented (see *Figure 1*). These areas are identified as major aggregate suppliers in Metro Manila, where there is substantial demand for aggregates used in the construction of both horizontal and vertical structures.

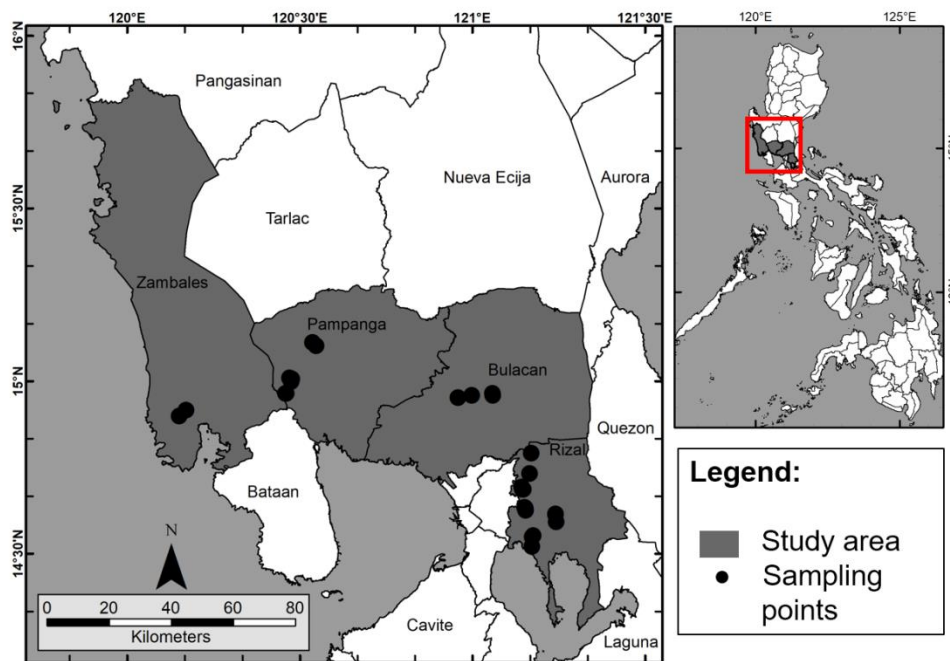


Figure 1. Location map of the study area. Bulacan, Rizal, Pampanga and Zambales are the main aggregate suppliers for Metro Manila.

2. Aggregate quarries

Fieldwork in various aggregate quarries was conducted, mainly to collect samples. There were two general types of sources for the aggregates used in this study: (1) alluvial deposits and (2) rock exposures.

2.1 Bulacan

In Bulacan, four (4) operating quarries in Dona Remedios Trinidad (DRT) and Angat were sampled (see **Figure 2**). In the DRT, the quarries are extracted from exposures of the Madlum Formation (Middle Miocene), whereas the Angat River quarries in Marungko and Niugan River are working on alluvial deposits (see **Figure 3**). The Madlum Formation is a sequence of shale, siltstone, wacke and conglomerate exposed along Madlum River in the vicinity of Barangay Madlum, San Miguel, Bulacan. Included in this

formation are the upper metavolcanic member of the Sibul Formation along Madlum River and the upper tuffaceous member of the Quezon Formation in the Angat River area.^{4,5} The samples collected in this area are mostly porphyritic basalt with intercalated lamina of very fine to coarse grained sandstone.

On the other hand, in the Marungko and Niugan River Quarries, cobble to boulder samples were randomly selected from the stockpiles. Samples collected vary from igneous to sedimentary rocks, with variations as well within the rock suites. The igneous samples included porphyritic basalt with euhedral plagioclase phenocrysts more than 4mm across, with microphenocrysts of pyroxene and plagioclase laths embedded in volcanic glass.

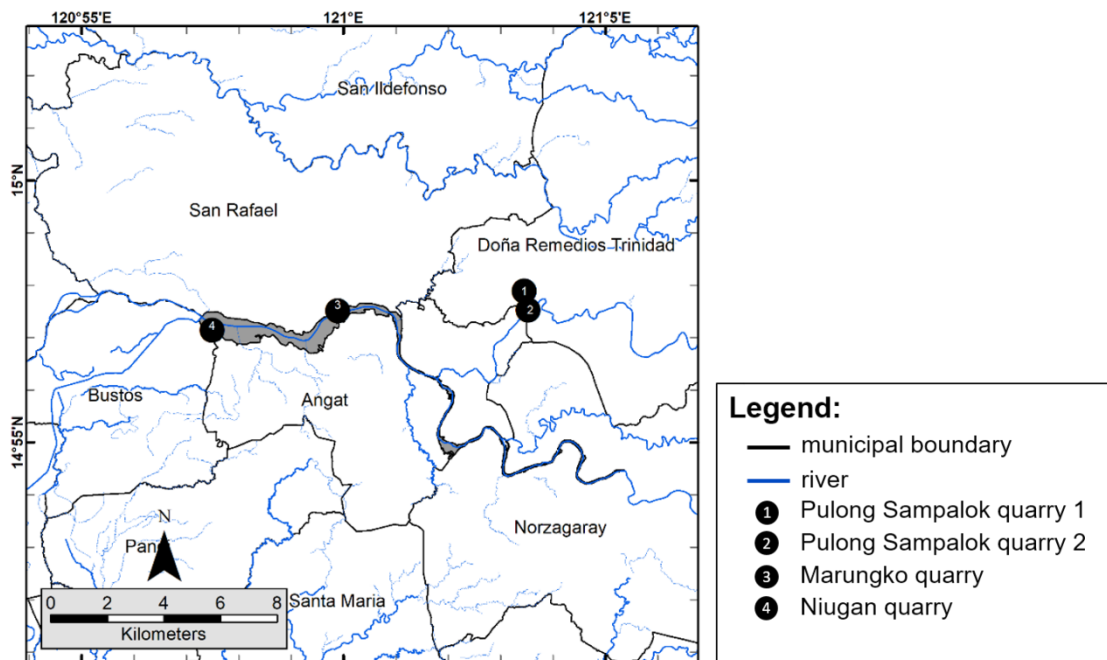


Figure 2. Sample location map in the province of Bulacan. Sampling stations 1 and 2 are located in the town of Dona Remedios Trinidad while sampling stations 3 and 4 are situated in the alluvial deposits of Angat River.

2.2 Rizal

Seventeen (17) aggregate quarries were sampled in Antipolo, Angono, San Mateo, and Rodriguez (see **Figure 4**). Most of the quarries are mining rock exposures belonging to the Montalban Ophiolitic Complex, Madlum Formation and Kinabuan Formation. The Middle Miocene Madlum Formation consists of a thick sequence

of sandstone, shale and minor conglomerates as well as andesite flows, pyroclastic breccia, tuff, greywacke and argillite, with massive cavernous limestone with occasional thin beds of crystalline limestone. The Montalban Ophiolitic Complex is the name given by the Mines and Geosciences Bureau³ to describe the incomplete ophiolitic sequence in the Southern Sierra Madre. It

consists of layered and massive gabbro, sheeted diabase dikes, pillow basalts and turbiditic sedimentary rocks. The Late Cretaceous Kinabauan Formation a sequence of sandstone,

shale, limestone, calcarenite and calcilutite, is considered the sedimentary cover of the Montalban Ophiolitic Complex⁴.



Figure 3. (left) Rock exposure in Dona Remedios Trinidad, Bulacan. This is a member of the Madlum Formation, a sequence composed clastics, metavolcanics and tuffs. (right) Alluvial quarry along the Marungko River in Angat. It is composed of Quaternary alluvium deposits.

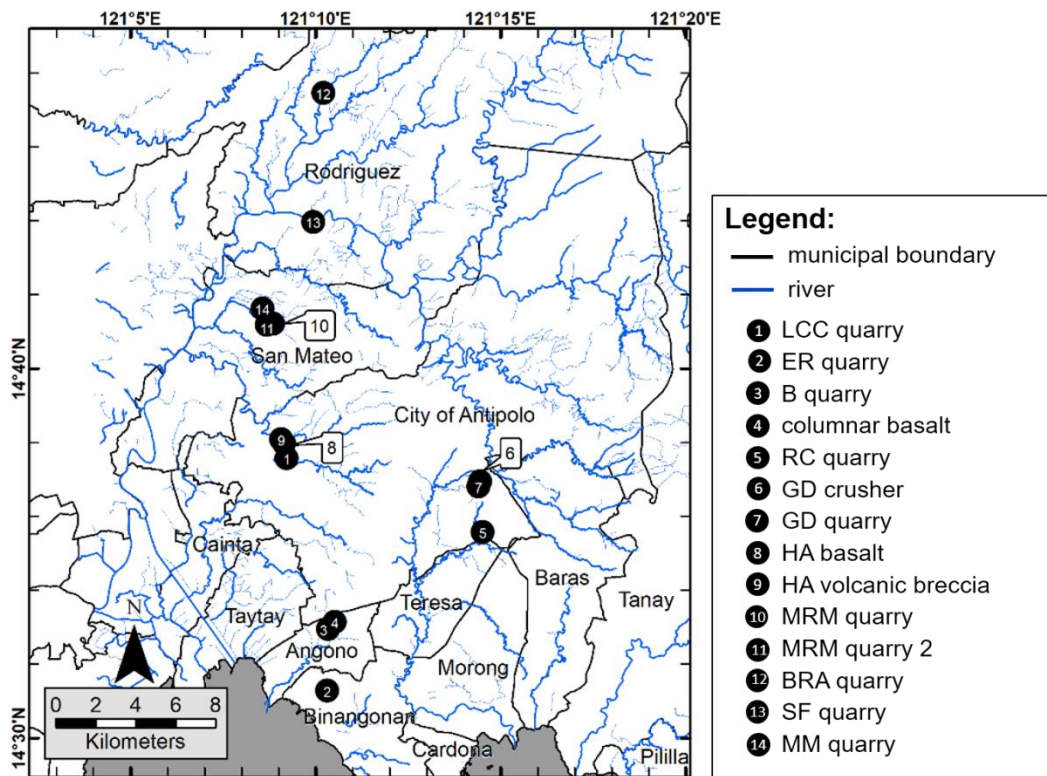


Figure 4. Sample location map of the samples from the towns of Rodriguez, San Mateo, Antipolo and Angono.

2.3 Zambales

In Zambales, aggregate materials were collected from a quarry situated in Barangay Looc, Castillejos, Zambales (**Figure 5**). Samples from this site are mainly products of erosion of the

ophiolite from the Zambales Range mixed with the lahar deposits from the Pinatubo eruption. Different kinds of igneous rocks identified here are silicified basalts and serpentinized ultramafics. The company is conducting alluvial

quarrying and hauled aggregates are crushed and sized at the crusher near the site. This crusher produces three (3) aggregates products, S -1, 3/4, and G -1, with increasing size respectively.

2.4 Pampanga

Aggregate samples from Pampanga were taken directly from the alluvial source. There were two locations in which these aggregates were

collected: from the Floridablanca and Pasig-Protero rivers where the 1991 Pinatubo lahar were deposited (see **Figure 6**).

The samples were mainly lahar deposits combined with alluvial deposits (microporphyrific andesites, amygdaloidal basalt and pumice). Different kinds of igneous rocks were identified here (see **Figure 7**).

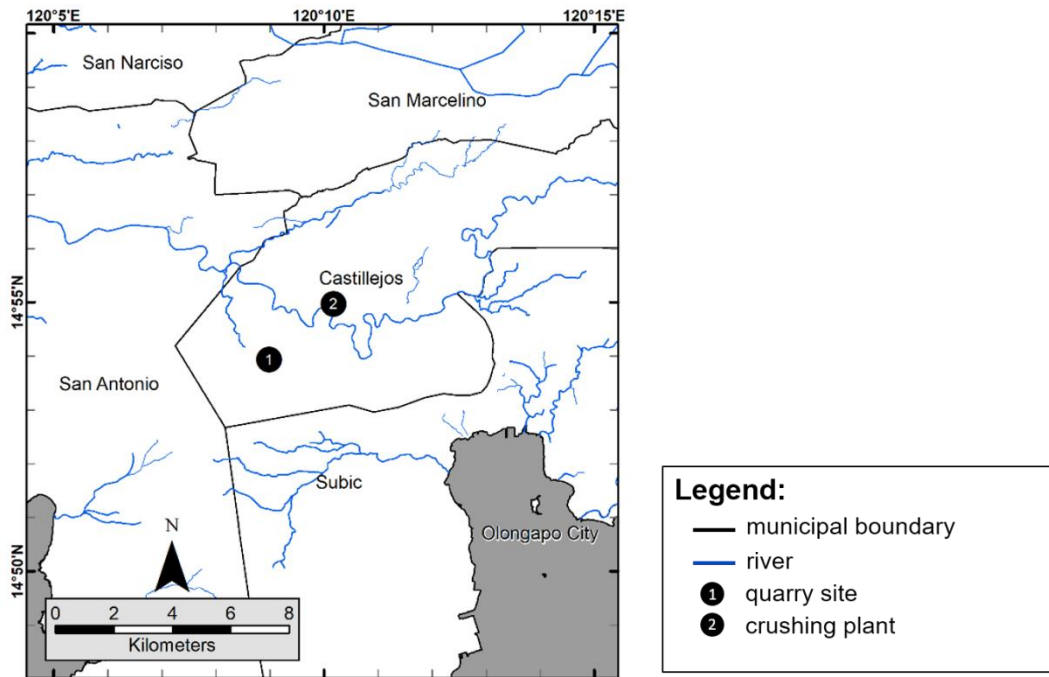


Figure 5. Sample location map of the aggregate samples in Zambales. 1 was collected from the quarry site while 2 was from the crushing plant.

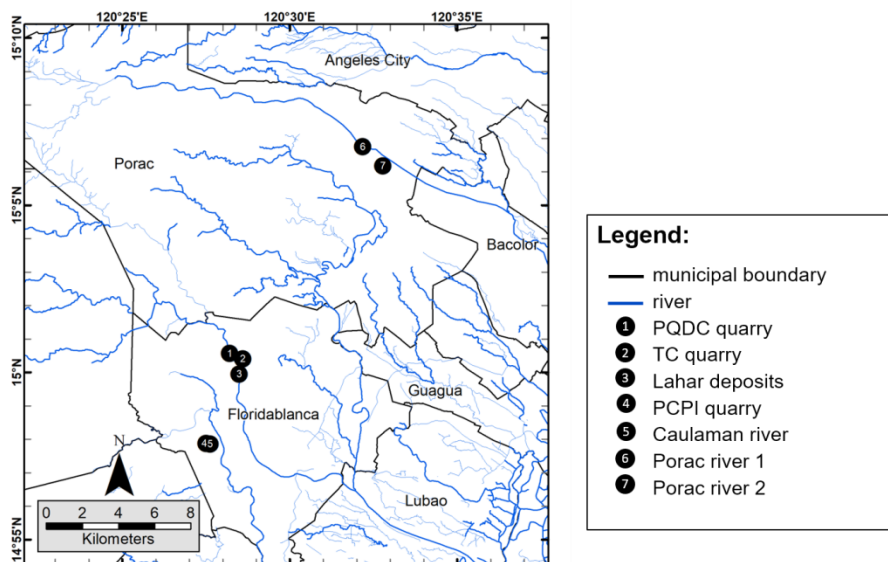


Figure 6. Sample location map of the samples collected from the province of Pampanga. Most of them are lahar deposits along the rivers of Caulaman and Floridablanca.



Figure 7. Lahar deposit quarry at Gumain River.
Aggregates ranges from boulder to clay size and are mostly andesites and pumice.

3. Results: Petrography of the aggregates

Transmitted light microscopy of the aggregate samples showed variations in the rock types from the different sites. Focused petrographic examinations were performed on the mounted thin section slides such as:

- 1) Identification of components (primary and secondary)
- 2) Identification of potentially deleterious features and components
 - a) Textural: presence of microfaults and other possible failure features such as cavities; presence of alteration minerals such as clay.
 - b) Compositional: identification of constituents that may be potential to reactions such as alkali-silica and alkali-carbonate reactions in concrete and other components that may affect the strength of the concrete.

3.1 Bulacan aggregates

Table 1 lists the sample name and petrographic identification of the samples. The dominant rock types in the DRT samples were porphyritic basalt and fine to coarse grained sandstone of the Madlum Formation (see **Figure 8**).

Samples BUL 10-01, -02, -05, -06, -13, -28, and -35 comprise vitrophyric to porphyritic basalts containing clusters of phenocrysts of clinopyroxenes, euhedral laths and twinned plagioclases and opaque minerals embedded in a groundmass of volcanic glass with plagioclase laths. Chlorite replaced some of the primary minerals. Some amygdaloidal basalts (samples BUL 10-18, -21, -23, -24 and -25) contain irregularly shaped vesicles filled with silica. Subhedral to euhedral microphenocrysts of plagioclases (1 mm across) were observed in microcrystalline groundmass. The vitroporphyritic basalt contains clustered phenocrysts of euhedral clinopyroxene (30%) crystals up to 5mm across with some crystals twinned; euhedral laths, twinned plagioclase (15%) which are altered to clay minerals; and opaque minerals (15%) embedded in a groundmass (40%) of volcanic glass with feldspar microlaths. Some samples collected are amygdaloidal with irregularly shaped vesicles lined with silica minerals.

Sandstones and wackestones of the Madlum Formation were also quarried as aggregates (BUL 10-03, -04, -07, -08, -09, -10, -11 and -12). Angular lithic fragments of volcanic porphyritic rocks and mudstone are present. Crystal

fragments of pyroxenes, plagioclases and quartz, with the rare occurrence of foraminifera, can be observed in the wackestones. The matrix ranges from sandy, with sparry calcite cement, to clayey.

Cobbles to boulders of fine-grained diorites were collected from the Angat alluvial quarry. They contain anhedral twinned plagioclases and green hornblende and clinopyroxenes altered to chlorite and epidote.

Table 1. Samples collected in Bulacan Province, with petrographic identification and potentially deleterious features and components.

Dona Remedios Trinidad		Marungko, Angat		Niugan, Angat	
BUL 10-01 BUL 10-02 BUL 10-05	Porphyritic basalt	BUL10-13	Porphyritic basalt	BUL 10-21 BUL 10-23 BUL 10-24 BUL 10-25	Amygdaloidal basalt
BUL 10-03 BUL 10-09 BUL 10-10	Wacke	BUL 10-14 BUL 10-17 BUL 10-19 BUL 10-20 BUL 10-22	Diorite	BUL 10-22 BUL 10-26 BUL 10-27 BUL 10-28 BUL 10-33 BUL 10-34	Diorite
BUL 10-04 BUL 10-08	Siltstone	BUL 10-15 BUL 10-16	Dacite	BUL 10-29	Andesite
BUL 10-06 BUL 10-11 BUL 10-12	Sandstone	BUL 10-18	Amygdaloidal basalt	BUL 10-30	Quartz vein cobble
				BUL 10-31 BUL 10-36	Very altered rock
				BUL 10-35	Chloritized basalt

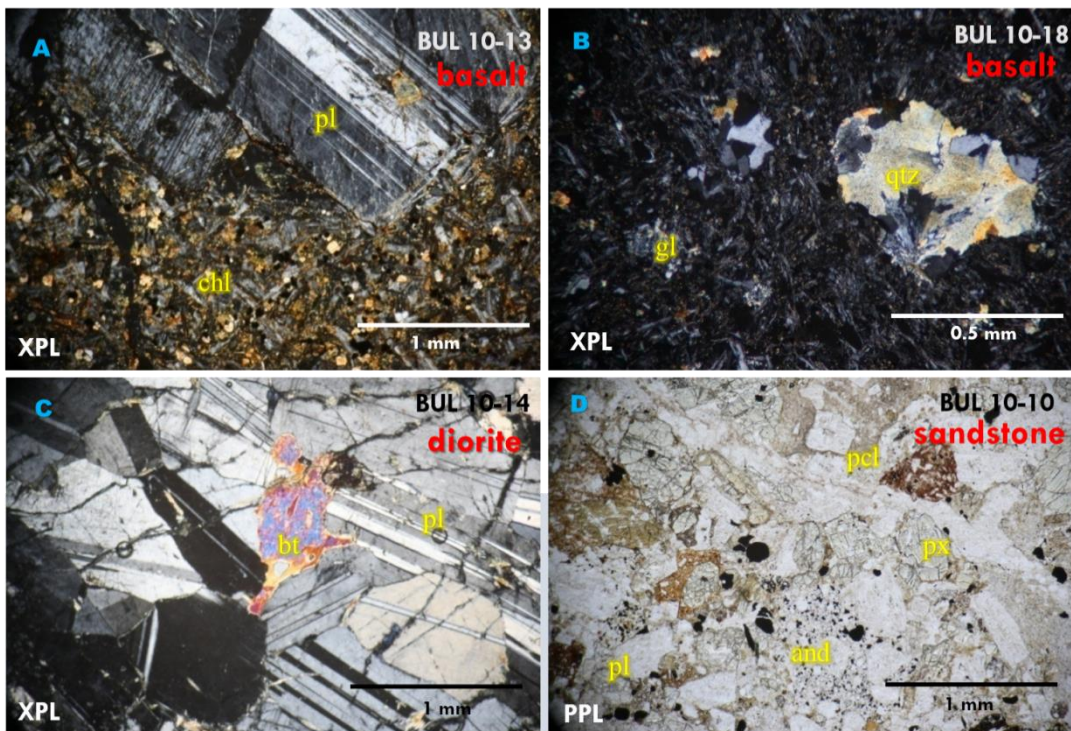


Figure 8. (A) Sample BUL 10-13. 50x. XPL. Porphyritic basalt showing plagioclase (pl) grains in chloritized (chl) groundmass. (B) Sample BUL 10-18. 100x. XPL. Amygdaloidal basalt showing quartz amygdales and volcanic glass (gl) groundmass. (C) Sample BUL 10-14. 50x. XPL. Diorite showing biotite (bt) grain surrounded (pl). (D) Sample BUL 10-10. 50x. Sandstone in PPL showing lithic fragments of andesite (and) and pyroclastics (pcl) with crystal fragments of pyroxenes (px) and plagioclases (pl).

Under a polarizing microscope, the Bulacan aggregates show cavities and microfractures (see **Figure 9**). The amygdaloidal basalt contains irregular- to spherical-shaped cavities which are filled with secondary minerals like chlorite, silica and/or carbonates (see **Table 1**). Fractures filled up with silica and carbonate minerals are also observed (BUL 10-02, -04, -05, -27 and -29).

The presence of clay minerals in the aggregates may also weaken the aggregates as these are soft materials in a flaky habit. Clay minerals occur mainly as alteration products of the original rocks. Some of the samples taken from the Marungko and Niugan alluvial quarries include altered samples with clay minerals.

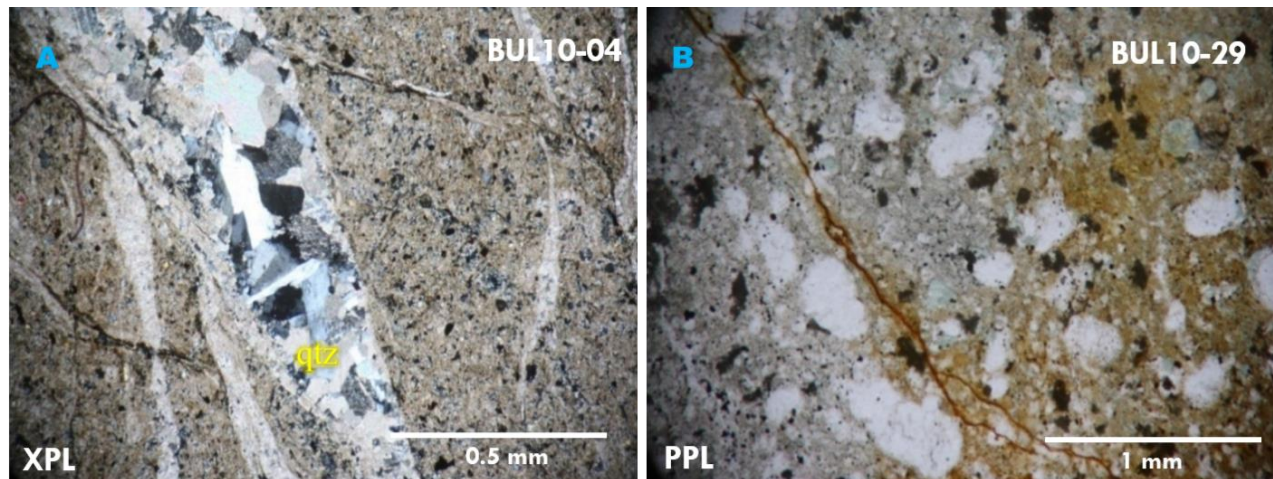


Figure 9. (A) Sample BUL 10-04. 100x. XPL. Sample showing a fracture filled in with quartz (qtz) vein. (B) Sample BUL 10-29. 100x. PPL. Altered sandstone with microcracks (brown).

3.2 Rizal aggregates

Rizal is one of the main sources of aggregates for the construction industry in Metropolitan Manila. The aggregate quarries work mainly on rock outcrops of the Kinabuan Formation (Late Cretaceous). **Table 2** gives the information on the Rizal aggregates.

The Antipolo basalts are vitrophyric and porphyritic hypocrySTALLINE, with phenocrysts (0.5-4mm across) composed of subhedral to euhedral twinned plagioclase, euhedral polygonal olivine and euhedral twinned clinopyroxene. Microphenocrysts (0.1 mm across) include plagioclase, clinopyroxene and olivine and trace amounts of thin laths of potassium feldspar. Some of them are also amygdaloidal with irregular to spherical amygdules of clay and chlorite (see **Figure 10**). Moderate alteration occurs with clay minerals, quartz, calcite and chlorite as secondary phases. Other rocks sampled include laminated claystone and fine-grained wacke. Angular crystal fragments of

quartz and feldspars less than 0.1 mm across are embedded in a clayey matrix.

An amygdaloidal microporphyrritic basalt with fine grained twinned plagioclase microphenocrysts in a volcanic glass groundmass was collected from a non-operating quarry in Angono. The amygdules contain chlorite. A potential aggregate quarry site in Angono was also visited for this study. The studied outcrops show intercalations of amygdaloidal porphyritic basalt and lithic tuff.

Aggregates from the San Mateo quarries consist mainly of aphyric porphyritic basalt. Samples CON-01, -02, and -03 are fine-grained hypocrySTALLINE with subhedral laths of twinned slender plagioclase (65%) laths as phenocrysts, with anhedral quartz in a vitric groundmass. MON-10-01 is glomeroporphyritic andesite with phenocrysts of subhedral laths (up to 4mm), with the characteristic twinning and sieve texture plagioclase and subhedral to euhedral prismatic

crystals of clinopyroxene in a devitrified groundmass.

The OXF aggregate samples from Rodriguez include mainly aphyric to porphyritic basalt with subhedral to euhedral plagioclase and pyroxenes. Plagioclase (45%) up to 0.5 mm across occurs as thin laths in the groundmass. Clinopyroxenes (10%) occur as subhedral to euhedral crystals 0.5 mm across. Smaller olivine, up to 1 mm occurs as subhedral to euhedral crystals. VUL samples exhibit crystalline, porphyritic texture with twinned subhedral plagioclase (< 0.1 mm across), subhedral prismatic pyroxene (< 0.1 mm across), and relict olivine phenocrysts in a feldspathic

groundmass, while one of the samples is amygdaloidal porphyritic with microlaths of feldspars in a glassy groundmass. The PAC sample is a pyroclastic rock with lithic clasts (0.5 to 4 mm) in a crystal tuff matrix. Lithic clasts (20%) are subangular to angular fragments of porphyritic and amygdaloidal basalts. Crystal fragments (10%) of pyroxenes are also present. The SUP samples are amygdaloidal porphyritic aphyric basalts, with anhedral to subhedral crystals phenocrysts of subheral thin plagioclase laths, anhedral olivine and clinopyroxene. The groundmass includes microlaths of plagioclase and clinopyroxene crystals with volcanic glass. Amydules contain chlorite + quartz + calcite.

Table 2. List of samples collected from Rizal.

Antipolo		Angono		Rodriguez		San Mateo	
ANTJ10-01	Porphyritic basalt	ANGJ10-01	Amygdaloidal basalt	PAC 10-01	Lithic tuff	CON 10-01	Basalt
ANTJ10-02	Amygdaloidal basalt	ANGJ10-02	Porphyritic basalt	OXF 10-01	Altered rock	CON 10-02	Basalt
ANTJ10-04	Amygdaloidal basalt	ANGJ10-07	Amygdaloidal basalt	OXF 10-02	Porphyritic basalt	CON 10-03	Porphyritic andesite
ANTJ10-05	Porphyritic andesite	ANGJ10-08	Amygdaloidal basalt	OXF 10-03	Basalt	MON 10-01	Andesite porphyry
ANTJ10-08	Amygdaloidal basalt	ANGJ10-10	Amygdaloidal basalt	OXF 10-06	Basalt		
ANTJ10-13	Laminated claystone and sandstone	ANGJ10-12	Amygdaloidal basalt	OXF 10-07	Basalt		
ANTJ10-14	Sandstone	TERJ10-01	Amygdaloidal basalt	VUL 10-01	basalt		
ANTJ10-24	Claystone	TERJ10-02	Amygdaloidal basalt	VUL 10-02	Basalt		
GOZ 10-01	Crystal tuff			VUL 10-03	Amygdaloidal basalt		
GDS 10-01	sandstone			VUL 10-04	Basalt		
ACE 10-01	Amygdaloidal basalt			VUL 10-05	basalt		
				VUL 10-06	Porphyritic basalt		
				SUP 10-01	Amygdaloidal basalt		
				SUP 10-02	Amygdaloidal basalt		
				SUP 10-03	Amygdaloidal basalt		
				SUP 10-04	Basalt		
				SUP 10-05	Amygdaloidal basalt		
				SUP 10-06	Amygdaloidal basalt		
				RODJ 10-11	Amygdaloidal basalt		
				RODJ 10-12	Amygdaloidal basalt		

Cavities are in the form of vesicles in the basalts. Some are filled up with secondary minerals such as chlorite, silica and carbonates forming amygdules. The shapes vary from irregular to spherical. Some of the aggregates have fractures

which run through the samples. Some of these fractures are already filled with silica and carbonate minerals forming veins, veinlets and stringers. Microstructures such as microfractures and cavities occur, too (see *Figure 11*).

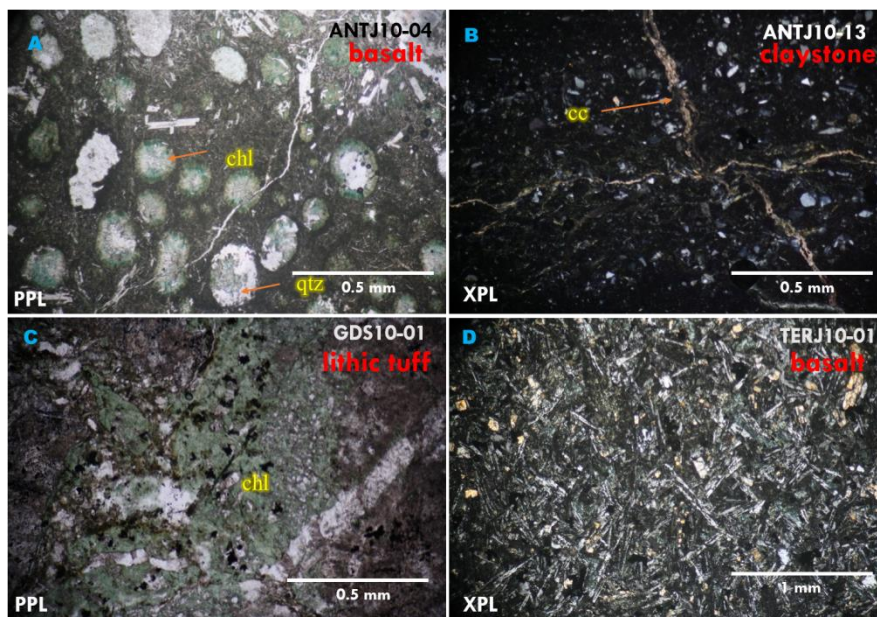


Figure 10. (A) Sample ANTJ10-04. 100x. PPL. Amygdaloidal basalt showing rounded cavities filled with quartz (qtz) and chlorite (chl). These amygdales are surrounded by volcanic glass groundmass. (B) Sample ANTJ10-13. 100x. XPL. Claystone sample with criss-crossing calcite (cc) veins. (C) Sample GDS10-01. 100x. PPL. Chloritized (chl) lithic tuff with quartz veins. (D) Sample TERJ10-01. 50x. XPL. Porphyritic basalt showing the twinned, euhedral plagioclase laths and some chlorite grains.

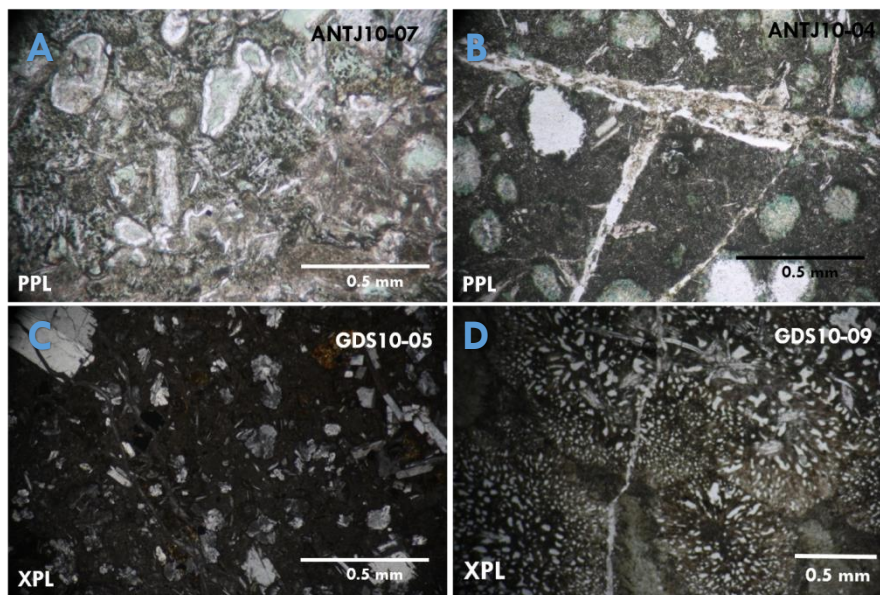


Figure 11. (A) Sample ANTJ10-07. 100x. PPL. Chloritized porphyritic basalt. Cavities are filled with silica and feldspars and the matrix is altered to clay. (B) Sample ANTJ10-04. 100x. PPL. Amygdaloidal with amygdules filled with chlorite and quartz. It also contains cracks and microfractures. (C) Sample GDS10-05. 100x. XPL. Porphyritic basalt with plagioclase crystals. (D) Sample GDS10-09. 100x. XPL. Porphyritic basalt showing myrmekitic texture of silica.

3.3 Zambales aggregates

The aggregates were collected mainly from a rock quarry and crushing plant. **Table 3** summarizes the properties of the rocks found in the Zambales quarry.

The basalts (CAS-01, -04, -06) are mostly silicified aphanitic to porphyritic hypocrystalline with subhedral to anhedral pyroxene (augite) crystals as phenocrysts where some of the crystals are chloritized. Rare fine-grained plagioclases occur in the devitrified volcanic glass groundmass.

Variably serpentinized ultramafic and altered mafic rocks are observed (CAS-02 -03 and -07) in the same quarry (see **Figure 12B**), including harzburgite and gabbro, respectively (see **Figure 12C**), where the feldspars and anhedral pyroxene crystals are observed to be disseminated. CAS -08 is a harzburgite composed of orthopyroxene and olivine altered to serpentine and chlorite. Chlorite is found in the cracks of the crystals

while serpentine forms the mesh texture. Drusy quartz veins are also observed (see **Figure 12A**).

Samples from the crushing plants are composed of several fragments of serpentinized harzburgite. Serpentine is identified by its low relief, low birefringence and a typical serpentine appearance (see **Figure 12B**).

The aggregates from the Unirock quarry exhibit features which may affect their strength and durability. The physical features that were identified include cavities and microfractures, which are observed in almost all the samples. The fractures are filled with silica and carbonate minerals forming veins and veinlets that run through the samples (see **Figure 13**).

The samples are also intensely altered to clay and serpentine minerals. This could affect the chemical property of aggregates as they are easier materials to weather.

Table 3. Samples collected in Zambales Province with petrographic identification.

Quarry Site		Crushing plant		
CAS-01 CAS-04 CAS-06	Basalt	S-1	Several rock fragments	Serpentinized ultramafic with several pyroxene crystals (85%) Disaggregated pyroxene crystals (5%) Very altered rock (10%)
CAS-02	Serpentinite	3/8	Several rock fragments	Heavily serpentinized ultramafics
CAS-03 CAS-07	Serpentinized peridotite	3/4	Several rock fragments	Peridotite
CAS-05	Gabbro	G-1		Chloritized rock, some parts are silicified, remnants of plagioclases and pyroxenes were observed
CAS-08	Harzburgite			

3.4 Pampanga aggregates

There are two aggregate sources in Pampanga: the municipalities of Floridablanca and Porac. In Floridablanca, samples were collected from the Gumain and Caulaman River quarries. Gumain aggregates are mostly alluvial and lahar deposits,

with different igneous rocks as cobbles and boulders and some minerals fragments of quartz and magnetite. These igneous rocks are identified as microporphyritic andesites, amygdaloidal basalts and pumice. The Caulaman River aggregates are mostly fresh andesites and basalts.

The basalts from both sources are vitrophyric with subhedral to euhedral plagioclases and pyroxenes phenocrysts embedded in an altered volcanic glass (see *Figure 14A*). The andesites are hypocrySTALLINE and porphyritic with clays, calcite and epidote replacing some of the pyroxene, and plagioclase phenocrysts and the

chlorite filling up the cavities in between crystals (see *Figure 14B*). Crystal tufts contain crystal fragments of iron oxides and clay minerals which replace amphiboles and plagioclases, respectively (see *Figure 14C*). *Table 4* summarizes the samples collected from Pampanga.

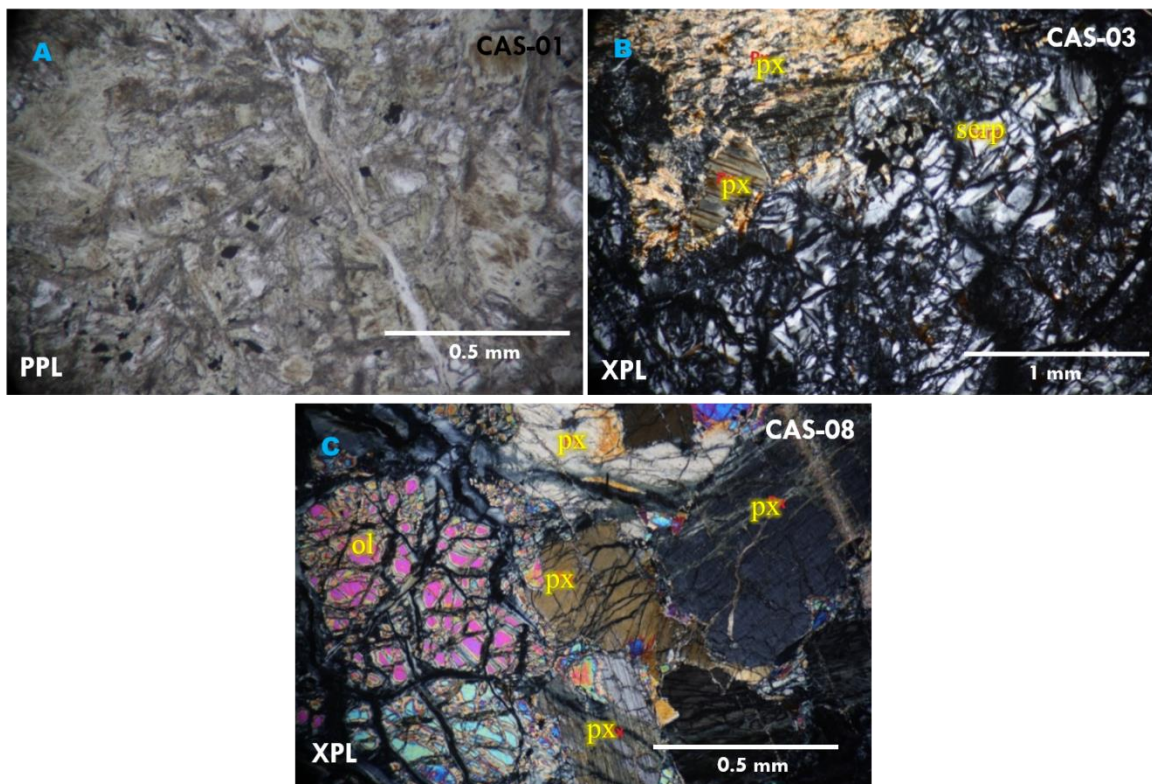


Figure 12. (A) Sample CAS-01. 100x. PPL. Section of basalt characterized by anhedral to subhedral pyroxenes and anhedral plagioclases. (B) Sample CAS-03. 50x. XPL. Heavily altered rock with serpentine (serp) as the main component. Several heavily altered pyroxenes (px) can also be observed. (C) Sample CAS-08. 100x. XPL. Slightly weathered harzburgite characterized by the presence of olivine (ol) and pyroxene (px) crystals. Serpentine can also be observed surrounding the mafic minerals and along mineral fractures.

In Porac, the aggregates are pyroclastic rocks, with gabbro, andesite, amygdaloidal basalt and pumice clasts. The andesitic fragments found are porphyritic with large zoned plagioclase and twinned amphibole grains. “White sand” was also collected from the quarry, which is basically lahar deposit with abundant pumice (see *Figure 15*).

The Pampanga aggregates contain cavities which may be due to the vesicles in the pumice and basalts. These are filled with secondary minerals like silica, chlorite and carbonates. Most of the

samples are also intensely altered to clay minerals.

4. Discussion: Assessment of potentially deleterious materials

A thorough petrographic examination of the constituents and textural characteristics can give indications of the quality, condition, and chemical stability of the aggregates. The mineral composition plays a significant role in the physical characteristics and engineering properties. A prior knowledge of the aggregate mineral properties would be helpful in the selection of aggregate sources.

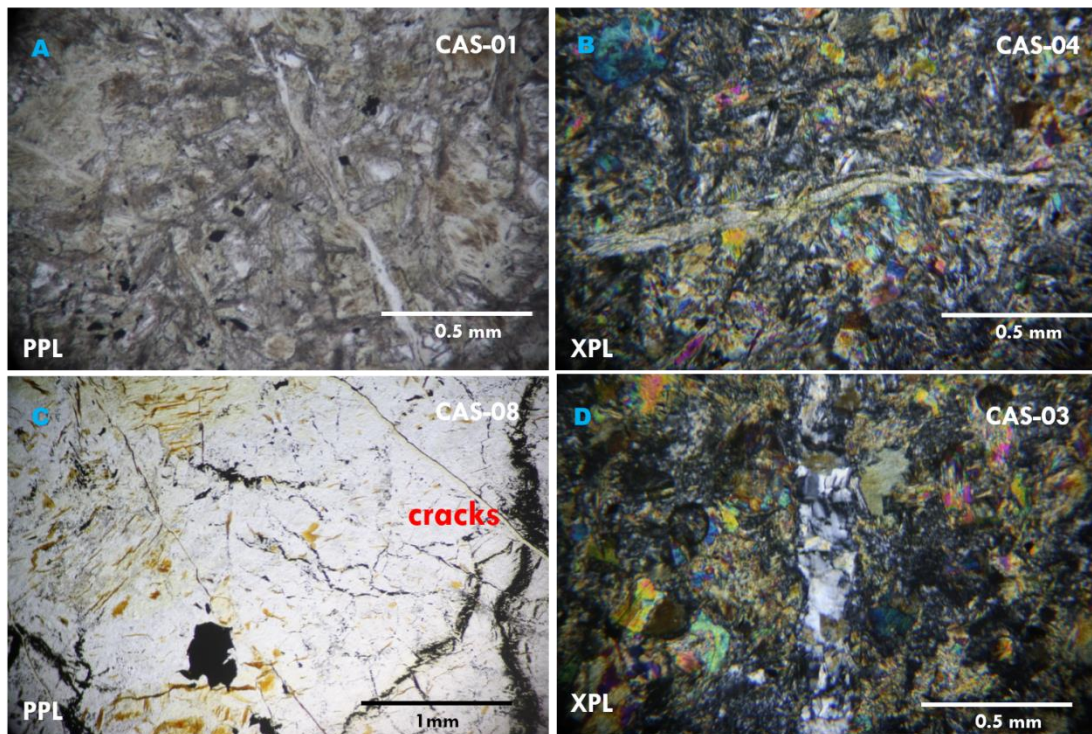


Figure 13. (A) Sample CAS-01. 100x. PPL. Chloritized basalt cut across by silica veins. (B) Sample CAS-04. 100x. XPL. Heavily altered rock also cut by carbonate vein. (C) Sample CAS-08. 50x. PPL. Rock with several cracks and microfractures. (D) Sample CAS-03. 100x. PPL. Heavily altered rock cut by a silica vein.

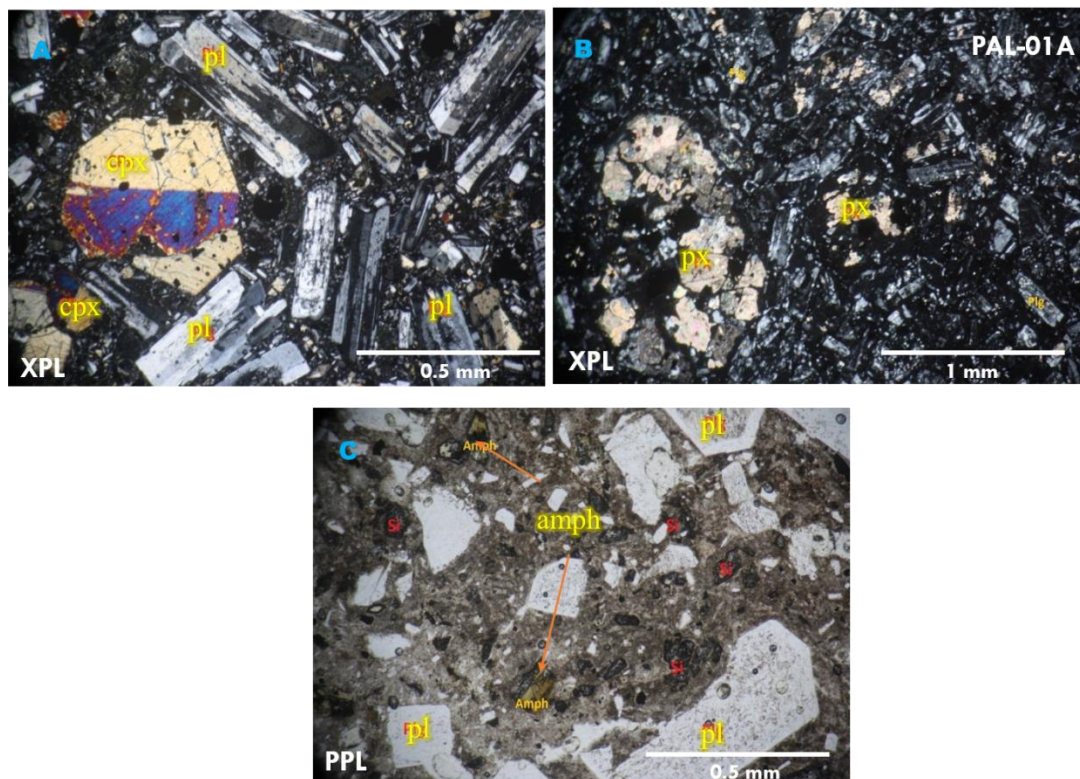


Figure 14. (A) Vitrophyritic basalt from the Pacific Concrete Products, Inc. XPL, FOV 2.2mm, 100x. (B) Highly weathered andesite porphyry with plagioclase as phenocryst. Taken from sample PAL-01A, one of the aggregates from Palakol Quarry Dev't Corp. XPL, FOV: 4.4mm, 50x. (C) Picture of a porphyritic hypohyaline rock with plagioclase and amphibole as phenocrysts. Some fragments are silicified. PPL, FOV: 2.2mm, 100x.

As a cheaper and quicker way of roadbuilding, asphalt is commonly used in the Philippines. This results in a huge demand for aggregates for the construction of infrastructure like roads to transport local products to market. Roberts *et al.*⁶ provide some general guidelines for aggregate used in Hot Mix Asphalt (HMA). Aggregate surface chemistry is used to determine how well an asphalt cement binder will adhere to an

aggregate surface. Poor adherence or stripping can cause premature structural failure. However, some aggregate chemical properties can change over time, especially after the aggregate is crushed. A newly crushed aggregate may display a different affinity for water than the same aggregate that has been crushed and left in a stockpile for a year. **Table 5** summarizes the desirable properties of rocks for HMA.

Table 4. List of samples collected from the Pampanga province.

Floridablanca			Porac		
Gumain River			Pasig-Protero River		
PAL-01A	Source	Andesite porphyry	GS-01	Source	Andesite and pumice
PAL-01B	Source	Amygdaloidal basalt	GS-02A	Source	pumice
S-1 Gumain	Crusher	Several rock fragments (porphyritic andesite, silica, pyroclastic materials)	GS-02B	Source	Porphyritic andesite
¾ Gumain	Crusher	Several rock fragments (pyroxenite, gabbro, lithic sandstone)	4mm	Crusher	Porphyritic basalt and andesite
¾ B red Gumain	Crusher	Oxidized porphyritic andesite	3/8 GS	Crusher	Pumice and amygdaloidal basalt
G-1 Gumain	Crusher	Basalt	Lahar WS	Crusher	Pumice, andesite, basalt
NS-1	Crusher	Pyroclastic materials (magnetite, white ash, plagioclase and amphibole fragments)			
NS-2	Crusher	Composed of pyroclastic materials with relatively more magnetite sand than NS-1			
LAH-01	Crusher	Reworked pumice			
Caulaman River					
NS-3	Source	Porphyritic andesite			
S-1 Caulaman	Crusher	Fragments of magnetite, pumice, quartz, and lithic fragments			
3/8 Caulaman	Crusher	Andesite and pumice			
¾ Caulaman	Crusher	Several rock fragments (andesite, conglomerate, magnetite)			
G-1 Caulaman	Crusher	Gabbro and andesite			
TRE-01	Source	basalt			

On the other hand, when used in concrete, aside from the dominant constituents of the aggregates, it is equally important to identify potentially alkali-silica reactive and alkali-carbonate reactive constituents. These reactive components produce hygroscopic gel which, when moisture is present,

absorbs water and expands⁷. The gel expansion causes cracking in the concrete. ASTM C295 identified the possible alkali-silica and alkali-carbonate reactive constituents. These reactants include: opal, chalcedony, cristobalite, tridymite, highly strained quartz, microcrystalline quartz,

volcanic glass, and synthetic siliceous glass which are commonly found in glassy to cryptocrystalline intermediate to acidic volcanic rocks, some argillites, phyllites, greywacke, gneiss, schist, gneissic granite, vein quartz, quartzite, sandstone, and chert. Potentially deleterious alkali-carbonate reactive rocks are usually calcareous dolomites or dolomitic limestones with clayey insoluble residues⁸. Furthermore, the mineral composition of aggregates may also give vital indicators of the stability of the components to local weathering conditions. The aggregates also need to be assessed texturally for microfractures and other possible failure features that could compromise the overall strength of the aggregates.

The aggregates collected from Bulacan are mostly basalts and diorites. Though basalt is

considered a good rock type for mixture with HMA because of its toughness, resistance to stripping, and good crushed shape⁴, the basalts in Bulacan are mostly amygdaloidal which means that there are cavities present and most are filled with silica, a potential alkali-silica reactive constituent. The diorites have good hardness and have a fair resistance to stripping which make them a fair component of aggregates. Sandstones are also good constituents of aggregates in Bulacan because of their fair hardness and good resistance to stripping, surface texture, and crushed shape. The presence of clay minerals as alteration products in the aggregates may also weaken the aggregates due to their soft nature and flaky habit¹. Furthermore, feldspars, silica and carbonates, which occur in some samples, are considered potential alkali reactive minerals to concrete.

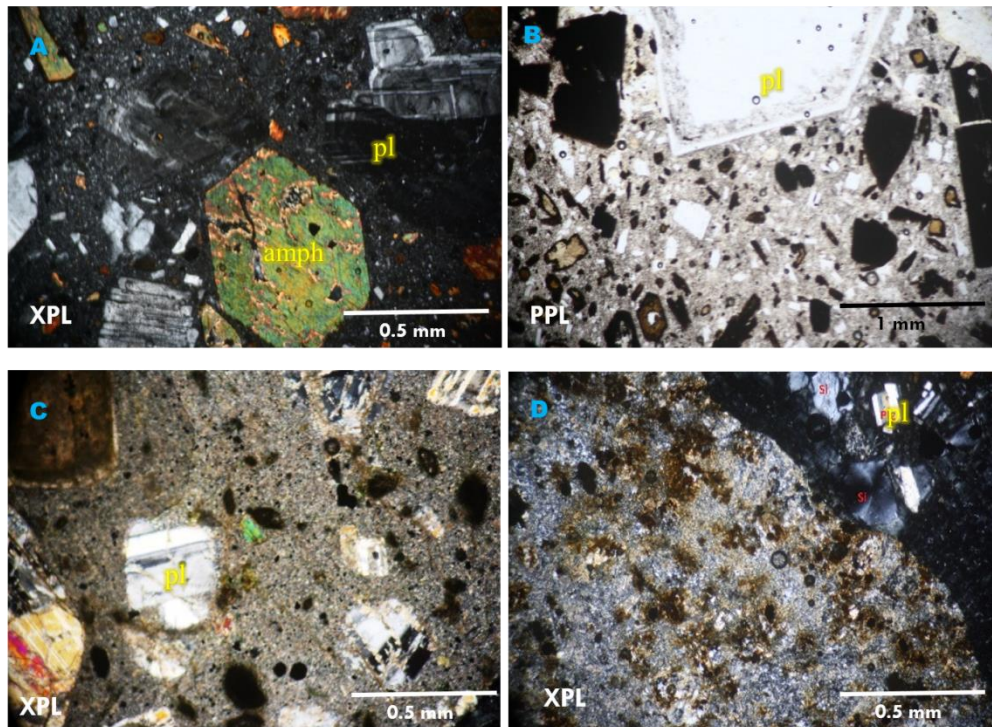


Figure 15. (A) Sample GS02B. 50x. XPL. Porphyritic andesite with large plagioclase (pl) and amphibole (amph) grains.

The groundmass is contains of volcanic glass. (B) Sample LAHAR. 50x. PPL. This sample was taken from the “white sand”. This photo only shows one of the components of the lahar deposit. This one is oxidizes porphyritic andesite, with large plagioclase (pl) grains and opaque minerals. (C) Sample Caulaman 3/8. 50x. XPL. Porphyritic volcanic rock fragment with plagioclase (pl) as phenocrysts and the groundmass is altered to sericite. (D) Sample S-1 Gumain. 50x. XPL. Heavily altered rock with silica and plagioclase (pl) crystals.

Aggregates from Rizal are also composed of amygdaloidal and porphyritic basalts, as well as

porphyritic andesites. Some of the samples are already heavily altered to chlorite and clay

minerals which may affect the toughness of the rocks. The volcanic glass groundmass is also a source of silica that is an alkali-silica reactive constituent. Aside from that, the presence of

criss-crossing veins of calcite and quartz in the studied basalts, andesites and some claystones may be considered as adverse factors.

Table 5. Desirable Properties of Rocks for HMA (from Cordon, 1979 as referenced in Roberts *et al.*⁵)

Notes: 1. Aggregates that are hydrophilic (water-loving) tend to strip more readily since water more easily replaces the asphalt film over each particle. 2. Freshly crushed aggregates with many broken ionic bonds tend to strip more easily.

Rock Type	Hardness, Toughness	Resistance to Stripping ^{1,2}	Surface Texture	Crushed Shape
<i>Igneous</i>				
Granite	Fair	Fair	Fair	Fair
Syenite	Good	Fair	Fair	Fair
Diorite	Good	Fair	Fair	Good
Basalt (trap rock)	Good	Good	Good	Good
Diabase (trap rock)	Good	Good	Good	Good
Gabbro (trap rock)	Good	Good	Good	Good
<i>Sedimentary</i>				
Limestone	Poor	Good	Good	Fair
Sandstone	Fair	Good	Good	Good
Chert	Good	Fair	Poor	Good
Shale	Poor	Poor	Fair	Fair
<i>Metamorphic</i>				
Gneiss	Fair	Fair	Good	Good
Schist	Fair	Fair	Good	Fair
Slate	Good	Fair	Fair	Fair
Quartzite	Good	Fair	Good	Good
Marble	Poor	Good	Fair	Fair
Serpentine	Good	Fair	Fair	Fair

Basalts and gabbros are the dominant rock-types in the Zambales samples. These, according to Roberts *et al.*⁶, are good components for aggregates. However, the basalts and gabbros contain serpentine, a secondary mineral which plays a critical role in determining the moisture

content in a rock. Its phyllosilicate structure allows more water to be captured, which can create surfaces of weakness and as a result lowers the rock strength⁹. The physical features that were identified include cavities and microfractures, while the chemical features are

mostly alterations of primary minerals to serpentine and clays. The fractures are filled with silica and carbonate minerals, forming veins and veinlets cross-cutting the samples. The silica and carbonate contents may be the source of alkali-silica and alkali-carbonate reactive components when mixed with concrete.

In the aggregates from Pampanga, the dominant rocks are basalts and andesites. They may be good components of aggregates; however, they are mixed with pumice, which is known for its low hardness, brittleness and vesicular texture, which make it a poor choice for aggregates. The lahar deposits also contain abundant quartz grains, which is an alkali-silica reactive component. Cavities from the vesicles of pumice and basalts are mostly filled up with secondary minerals like silica, chlorite and carbonates, which are potential ASR components.

5. Conclusions

Variable rock-types with different degrees and patterns of alteration occur in the four provinces of Philippines, which include the major aggregate quarries. Potential alkali reactive constituents were observed in some samples such as silica (including quartz) from devitrification of groundmass, veins, and amygdules. Potential durability of the aggregates may be influenced by the presence of microfractures, cavities and clay minerals. Further testing of the aggregates for durability and strength is suggested as per use of the aggregates. The employment of X-ray diffractometry and other analyses to test the compositions can also be used to confirm the presence of potential deleterious materials. Petrographic examination can also be directed specifically at the possible presence of contaminants in aggregates, such as synthetic glass, cinders, clinker, or coal ash, magnesium oxide, calcium oxide, or both, gypsum, soil, hydrocarbon, chemicals that may affect the setting behaviour of concrete or the properties of aggregate, animal excrement, plants or rotten vegetation, and any other contaminant that may be undesirable in concrete.

References

- [1] P. Petrounias, P. P. Giannakopoulou, A. Rogkala, P. M. Stamatis, P. Lampropoulou, B. Tsikouras and K. Hatzipanagiotou, "The effect of petrographic characteristics and physico-mechanical properties of aggregates on the quality of concrete," *Minerals*, 8(12), 2018.
- [2] M. A. Bérubé, "The mineralogical and petrographic analysis of concrete aggregates," *JOM*, 53(12), 45-47, 2001.
- [3] Mines and Geosciences Bureau (MGB), *Geology of the Philippines*, Mines and Geosciences Bureau – Department of Environment and Natural Resources (MGB–DENR), Quezon City, Philippines, 2004.
- [4] R. Pena, *Lexicon of Philippine Stratigraphy*, Mines and Geosciences Bureau – Department of Environment and Natural Resources (MGB–DENR), Quezon City, Philippines, 2004.
- [5] G.W. Corby, R. M. Kleinpell, W.P. Popenoe, R. Merchant, H. William, J. Teves, R. Grey, B. Daleon, F. Mamacalay, A. Villongco, M. Herrera, J. Guillen, J. S. Hollister, H. N. Johnson, M. H. Billings, E. M. Fryxell, E. F. Taylor, C. N. Nelson, D. C. Birch, R. W. Reed, and R. Marquez, "Geology and Oil Possibilities of the Philippines". *Technical Bulletin 21*, Bureau of Mines, DANR, 1951.
- [6] F. L. Roberts, P. S. Kandhal, E. Ray Brown, D. Lee and T. W. Kennedy, *Hot Mix Asphalt Materials, Mixture Design and Construction*, NAPA Research and Education Foundation, Lanham, MD, 1996.
- [7] Corps of Engineers Washington D.C., "Engineering and Design. Standard Practice for Concrete for Civil Works Structures." *Engineer Manual*, 1994. <http://www.dtic.mil/dtic/tr/fulltext/u2/a402916.pdf>
- [8] ASTM Committee D-30 on Composite Materials, *Standard test method for tensile properties of polymer matrix composite materials*, ASTM International, 2008.

- [9] P. P. Giannakopoulou, P. Petrounias, A. Rogkala, B. Tsikouras, P. M. Stamatis, P. Pomonis, and K. Hatzipanagiotou, “The influence of the mineralogical composition of ultramafic rocks on their engineering performance: A case study from the Veria-Naousa and Gerania ophiolite complexes (Greece),” *Geosciences*, 8(7), 2018.

Reconnaissance geochemical and geophysical exploration for gold at Iri gold field, north central Nigeria

Sidi Aliyu Ahmed^{1*}, Nuhu Musa Waziri², Hadiza Liman Mohammad³,
Mohammed Abubakar Mohammed⁴, Apeh Aromeh Gideon⁵

¹Department of Geology and Mining, Ibrahim Badamasi Babangida University, Lapai, Nigeria

²Department of Geology, Federal University of Technology, Minna, Nigeria

³Department of Geography, Ibrahim Badamasi Babangida University, Lapai, Nigeria

⁴Division of Graduate Studies and Research, Khazar University, Azerbaijan

⁵Adex Resources Limited Minna, Nigeria

*corresponding author email: saakusogi@gmail.com, aasidi@ibbu.edu.ng

Abstract

Field geological mapping and reconnaissance geochemical and geophysical exploration for gold was carried out at IRI Gold field north central Nigeria. Results of the geological mapping show the major lithology in the area is silicified sheared rocks and large quartz veins. Undifferentiated schist was intruded by quartzite at different locations and possibly during a major geological event which left shattering of the rocks all around two major ridges within the study area. Preliminary geochemical characterization revealed the rocks have weak geochemical anomalies of gold (Au), except in two locations where positive anomalies of gold (L3B=455ppb and L14=582ppb) were observed and identified as targets for further exploration. Interpretation of the aeromagnetic data gives the orientations of the structural features, and the major structural trend in the area is NE-SW. The lineaments extracted from the magnetic data range in length from 46.43m to about 1251.66m. Most of the lineaments extracted from the area are subsurface within the quartz-mica and migmatites while some of them have surface expressions, even though they are not clearly defined. Overall, the interpreted, geochemical signatures coincide with the geophysical signatures and were used to delineate the target prospective areas.

Index Terms: Gold mineralization, aeromagnetic data, geochemical data, schist belt, Nigeria

1. Introduction

Gold mineralization in the Nigerian schist belt is prominent. Pegmatite research in Nigeria by Ajibade¹ and Matheis *et al.*⁶ used rare elements as indicators for tin mineralization without adequate information on the petrology. Most of the gold mineralization in the pegmatite is associated with sulphides and confined to pegmatite intrusions as veins. Iri, the study area, is part of the Zuru Schist belonging to the Nigerian schist belt. Artisanal gold mining has been well established in most of the localities in the study area, exploiting shallow alteration zones and quartz intruded veins and pegmatite. Pegmatites are coarse grained igneous and metamorphic rocks and represent the end product

of the magmatic stage in the evolution of granitic melt. The pegmatite at Iri Village is the first mineralized pegmatite to be found in northern Nigeria and one of the few mineralized pegmatite fields in Nigeria.⁶ Other pegmatite fields are at Elbe, Ijero and Jema'a. Preliminary geochemical and geophysical exploration has been carried out in the area to identify possible prospective targets. The combination of geochemical studies of rocks and sediments and the interpretation of aeromagnetic data can give information about prospective targets for detailed gold exploration in the area. This research was therefore aimed at carrying out reconnaissance geochemical evaluation and aeromagnetic data

interpretation of parts of the Iri Gold field so as to identify mineralized targets.

1.1 The study area

The area is located near Iri village, in Rijau Local Government Area, North Central, Nigeria. It is located within latitude (4° 58' 00"N to 4° 58' 45"N) and longitude (11° 7'45"E to 11° 8'45"E) and covers an area of about 2.52 km² (see **Figure 1**). The area can be accessed through the Minna-Kontagora and Kontagora-Rijau Roads; it can also be accessed through the Kontagora-Bin Yauri-Rijau Road and borders the town of Zuru in Kebbi State. The nearest business centres are

Rijau and Zuru. The climate of the area is characterised by two distinct seasons, rainy and dry. The rainy season starts in April and ends in September. The peak of the rainfall period is between July and August. The temperature in the area varies between 30°C and 35°C. The coldest temperatures are experienced during the harmattan periods, when the temperature drops to 18°C. During the harmattan, the winds are cold, dry, dusty and strong. The area is made up of typical savannah vegetation.

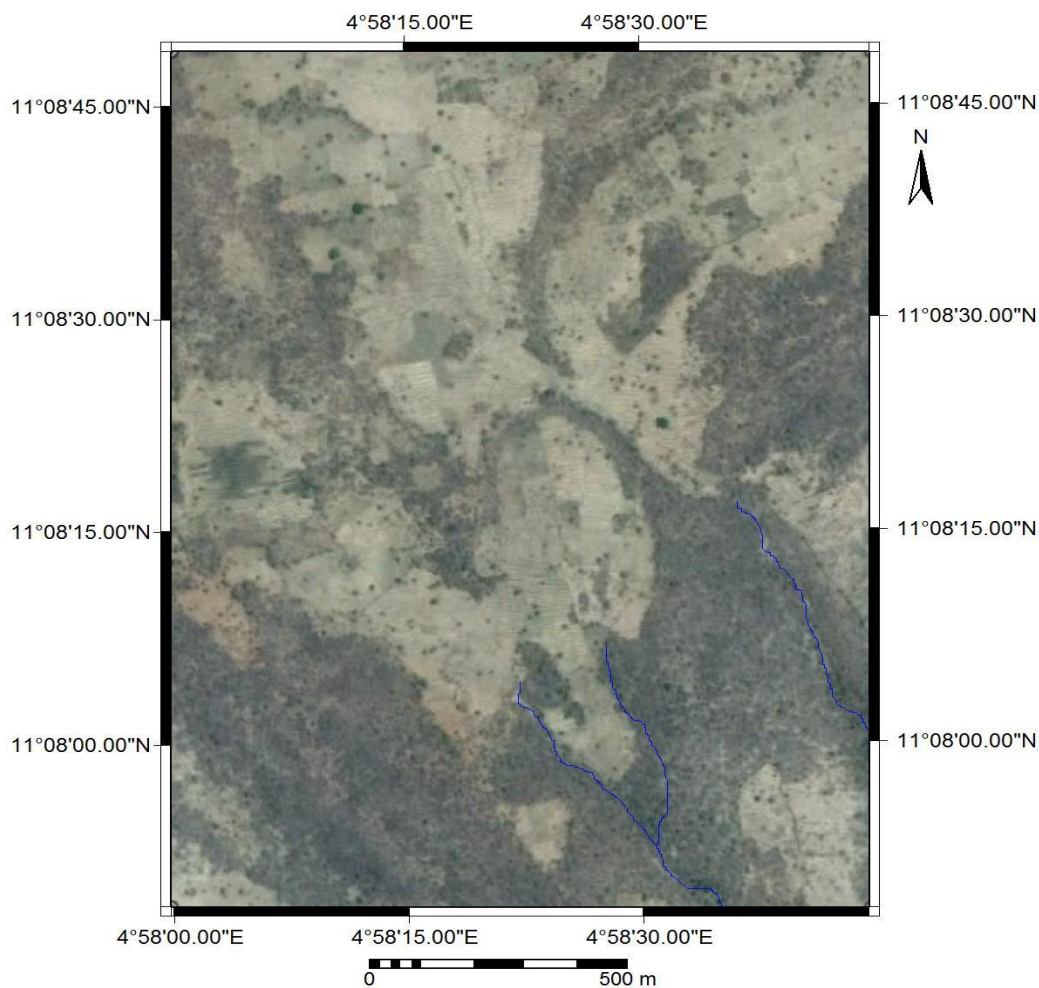


Figure 1. The study Area (modified from Google Earth, 2018).

1.2 Regional geological setting

The study area is part of the Nigerian schist belt. The Schist Belts in Nigeria comprise low grade, metasediment-dominated belts trending N-S which are best developed in the western half of

Nigeria. Oyawoye¹³ and McCurry¹⁸ consider the schist belts as relicts of a single supracrustal cover. Olade and Elueze¹¹ consider the schist belts to be fault-controlled rift-like structures. Grant,¹⁴ Holt¹⁶ and Turner,⁴ based on structural

and lithological associations, suggest that there are different ages of sediments. Ajibade *et al.*² disagree with this conclusion and showed that both series contain identical deformational histories. The structural relationships between the schist belts and the basement were considered by Truswell and Cope⁸ to be conformable metamorphic fronts and it was Ajibade *et al.*² who first mapped a structural break.

The geochronology of the schist belts remains problematic, although the ages of the intrusive cross-cutting Older Granites provide a lower limit of *ca* 750 Ma. A Rb/Sr age of $1,040 \pm 25$ Ma for the Maru Belt phyllites has been accepted as a metamorphic age by Ogezi³. The schist belt rocks are generally considered to be Upper Proterozoic. The geochemistry of the amphibolite complexes within the schist belts has also led to controversy. Klemm *et al.*⁵ have concluded that the Ilesha belt may be an Achaean greenstone belt. Olade and Elueze,¹¹ Ogezi³ and Ajibade¹ have favoured dominantly ensialic processes in the evolution of the schist belts, while Ajayi,¹⁷ Rahaman¹⁴ and Egbuniwe⁷ have stressed that some include oceanic materials with tholeiitic affinities. Some metallogenic features of the schist belts are relevant to these problems; the apparent absence of subduction related mineral deposits may be indicative of a limited role for the ensimatic processes; the distribution of primary gold occurrences in some belts but its marked absence in others may indicate that they do not represent a single supracrustal sequence.

The schist belts are confined to a NNE-trending zone about 300 km wide. The area to the west of this zone is made up of gneisses and migmatites that constitute the Dahomeyan of Burke *et al.*¹⁰ Similarly, to the east, no schist belts are known for a distance of 700 km until in Cameroun, where a number of schist belts, considered to be Upper Proterozoic, occur in the Pan-African granite-migmatite terrain north of the Congo Craton. The schist belts have been mapped and studied in detail in the following localities: Maru, Anka, Zuru, Kazaure, Kuseriki, Zungeru, Kushaka, Isheyin Oyan, Iwo, and Ilesha where

they are known to be generally associated with gold mineralization.

2. Material and Methods

2.1 Geological Mapping

Geological mapping was conducted in the area and geological information was recorded and further processed to produce the geological map, study field relations among lithological units and collect rock and soil samples for geochemical analysis.

2.1.2 Rock Sampling

Nineteen (19) rock samples (L3A, L3B, L5, L6, L9, L12, L14, L16, L18, L19, L20, L28, L29, L29B, L33, L36, L37, L38 and LDR) were collected at different locations during the geological mapping. The sampled rocks include pegmatite veins, quartz veins, quartzite and schist. At each location, the coordinates of the outcrop were recorded, hand specimen descriptions of the rocks were done and information on the texture, mineralogy and colour were recorded, the deformation structures on the rocks were observed and their orientations recorded.

2.1.3. Soils and Sediments Sampling

Twenty six (26) soil samples (L1S, L2S, L3S, L4S, L5S, L6S, L7S, L8S, L9S, L10S, L11S, L14S, L15S, L21S, L22S, L23S, L24S, L25S, L26S, L27S, L28S, L30S, L31S, L32S, L34S, and L35S) were collected in a 100 metre by 100 metre survey plan round the foot hills of the two ridges, One (1) pan concentrate stream sediment (L39BS) was collected at the stream beds of the river that drained in the area.

2.2. Geochemistry

At the sample preparation laboratory of MS Analytical in Abuja, Nigeria, all the samples collected were prepared for geochemical analysis. The procedure involved drying the samples and crushing to the particle size required. This was followed by grinding and milling of the rock samples to achieve the desired texture, and sieving of the soil and sediments. The samples were all transported to the MS

Analytical Laboratory in Canada for geochemical analysis using Au, Fire Assay, 30g fusion, AAS and Trace Level. For this purpose, the samples were crushed to pulverized fine before the analysis was carried out.

2.3. Aeromagnetic Data

The aeromagnetic data for the area covered by the study was acquired at a flight line spacing of 200 metres and a terrain clearance of 80 metres. The data available for this study was taken from the Shuttle Radar Topography Mission (SRTM), which was flown by the National Aeronautics and Space Administration (NASA) and obtained digital elevation models of the earth's surface. It is useful in surface mapping, especially in areas where a detailed geological map is not available. The data was acquired for this purpose from the Nigerian Geological Survey Agency (NGSA) Abuja, Nigeria, and is in gridded format, not flight line format.

3. Results and discussion

The sample locations map is presented in *Figure 2*, the geological map is presented in *Figure 3*, while the lineament map is presented in *Figure 4*.

3.1 Geology

Two anticlinal ridges occurred in the area. They are in the south-western and north-eastern parts of the area. Regolith overburden indicating a high degree of weathering covers the bedrocks. The top of the ridges are characterized by floated boulders of different sizes, mainly remnants of shattered quartzite. The quartzite boulders are massive, and whitish with yellow stains of iron incrustation. The textural composition of the quartzite boulders is fine grained. Isolated occurrences of Phyletic-Schist were observed in the area and believed to be intruded by quartzite during orogenic events. The schist was dark, containing mafic minerals and fine grained, dipping at 70°E and oriented to the S-W. Pegmatite and quartz veins occur as minor intrusive bodies which could be prospected for gold mineralization. Structural analysis of the aeromagnetic data indicates

that some of the rocks are well deformed and are either folded or faulted, trending N-S to NE-SW, which coincides with the disposition of the Pan African Basement structures². North-East trending fractures and faults were also exposed and are exploited by most of the pegmatite veins. The lineaments extracted from the magnetic data range in length from 46.43m to about 1251.66m. The structures suggest predominantly northeast-southwest tectonic trends (see *Figure 4*). Some of the lineaments derived from the magnetic data have surface expressions, even though they are not clearly defined.

3.2 Geochemistry

The Gold (Au) concentration maps in rocks and soils are presented in *Figure 5* and *Figure 6* respectively.

The concentration level of gold (Au) in the rock samples shows that all the samples analysed were mineralized with Au. Although the mineralization is quite above the crustal abundance of Au in normal geological materials of (4ppb),⁹ it is far from the minimum value to be referred to as ore (2000ppb).⁷ Therefore, the rocks show a weak anomaly, except in samples L3B and L14 (see *Figure 7*). Possible mineralization with depth is expected. Locations L3B and L14 were identified as target areas for detailed exploration work involving pit sampling. The Au concentrations in the samples from locations L3B and L14 were 455ppb and 582ppb respectively, which are well above the Clarke value of 4ppb. Plots of the concentration of Au in both rocks and soils are shown in *Figure 7* and *Figure 8*, and the target locations for further exploration were identified. The rock samples collected from L3B, L14, and L14P indicate moderate anomalies of Au. The soil samples from L2S, L14S, L24S, and L35S also indicate moderate anomalies, which coincide with the anomalies in the rocks. Comparison between the interpreted aeromagnetic data and interpreted geochemical data shows close agreement, and the results can be superimposed (see *Figure 9*).

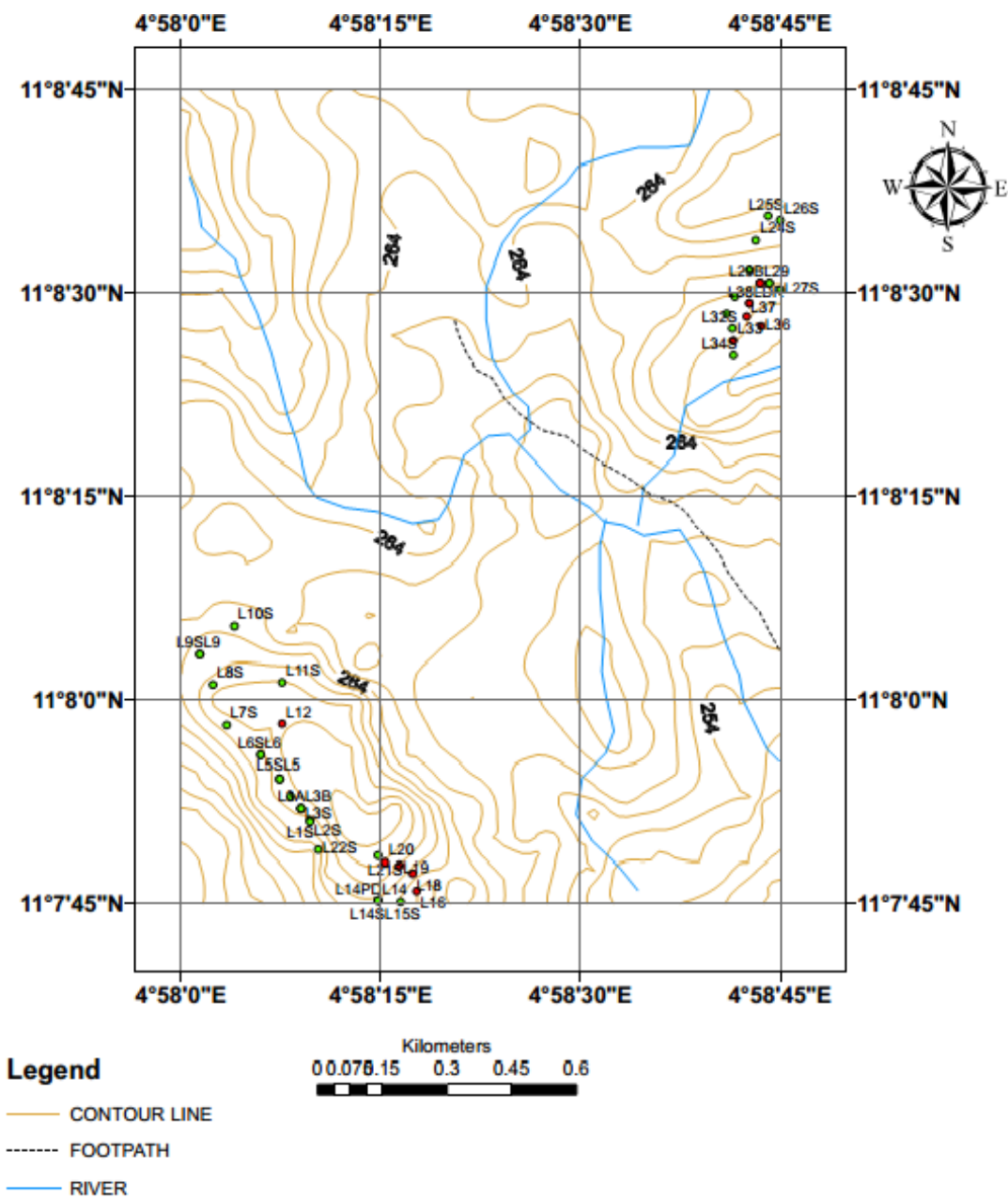


Figure 2. Sample locations map.

4. Conclusion

Preliminary geochemical and geophysical investigations conducted in the area suggest possible gold mineralization in two locations, where positive gold anomalies were identified. Prominent geological structures coupled with interpretation of the geochemical and geophysical data have been used to infer and delineate possible prospective targets. The major structural trend established from interpreting the aeromagnetic data is NE-SW, which is generally known to be associated with mineralization. The

lineaments extracted from the interpreted magnetic data range in length from 46.43m to about 1251.66m. Most of the lineaments extracted from the area are subsurface within the quartz-mica and migmatites, while some of them have surface expressions even though they are not clearly defined. Magnetic lows can also mark non-magnetic, possibly mineralized shear zones or alteration zones. Most of the magnetic lineaments are within a depth of a few meters to 250 meters.

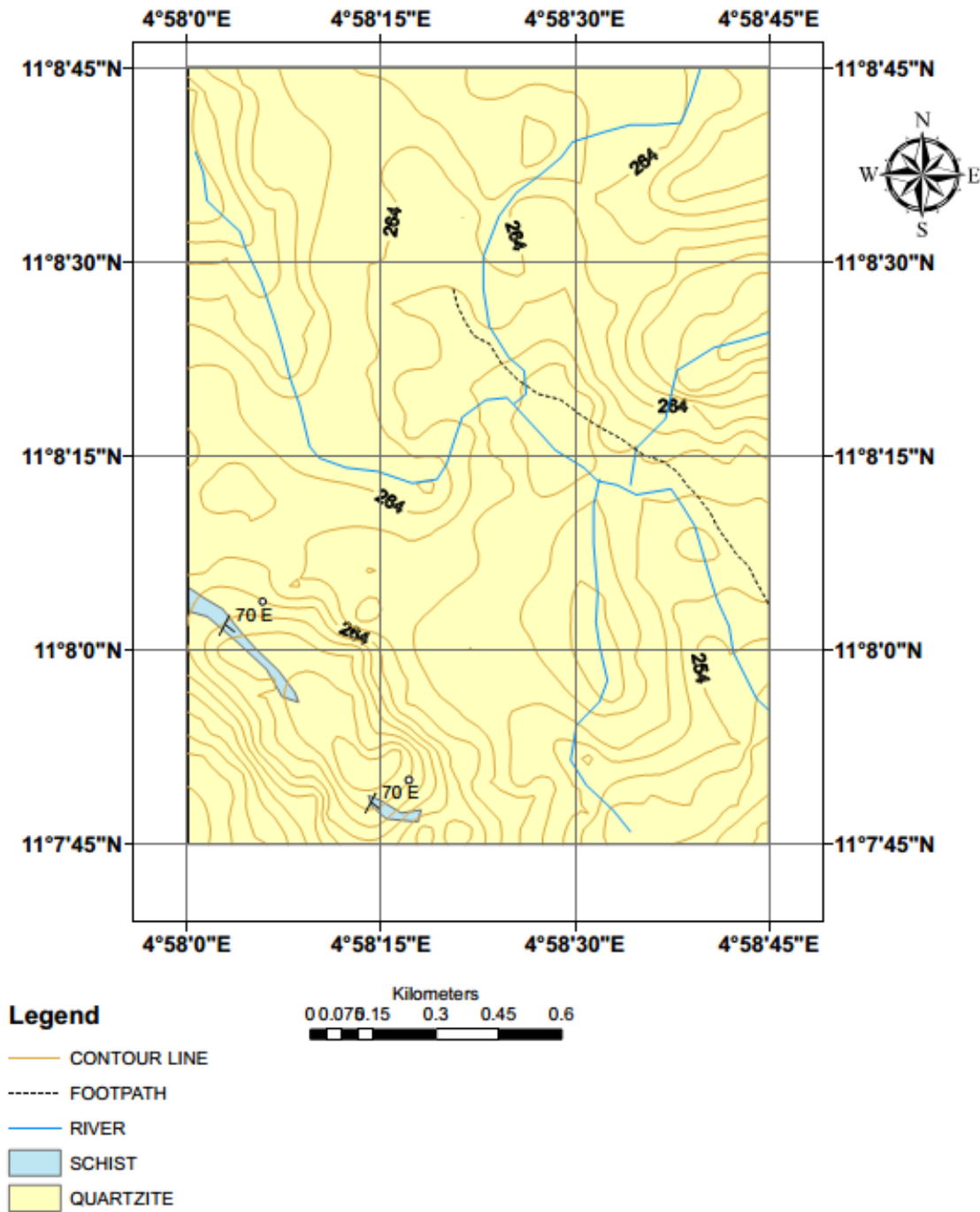


Figure 3. Geological map of the area.

References

- [1] A. C. Ajibade, *Geotectonic evolution of the Zungeru Region, Nigeria*, Unpublished Ph.D. thesis, University of Wales, Aberystwyth 1980.
- [2] A. C. Ajibade *et al.*, "The Zungeru mylonites Nigeria: recognition of a major unit," *Rev. de Geol. Geog. Phys.* 21, 359-363, 1979.

- [3] A. E. O. Ogezi, *Geochemistry and geochronology of basement rocks from north-western Nigeria*, Unpublished Ph.D. Thesis, University of Leeds, 1977.
- [4] D. C. Turner, "Upper proterozoic schist belts in the Nigerian sector of the Pan-African Province of West Africa," *Precambrian Res.* 21, 55–79, 1983.
- [5] D. D. Klemm, *et al.*, "The Precambrian metavolcano-sedimentary sequence east of Ife and Ilesha, SW Nigeria. A Nigerian 'Greenstone belt'?" *J. Afr. Earth Sci.* 2, 161-176, 1984.
- [6] G. Matheis *et al.*, "Rb-Sr isotopic study of rare-metal-bearing and barren pegmatites in the Pan-African reactivation zone of Nigeria," *J. Afr. Earth Sci.* 1, 35-40, 1983.
- [7] I. G. Egbuniwe, *Geotectonic evolution of the Maru Belt, NW Nigeria*. Unpublished Ph.D. Thesis, University of Wales, Aberystwyth, 1982.
- [8] J. F. Truswell *et al.*, "The geology of parts of Niger and Zaria Provinces, Northern Nigeria," *Geol. Survey Nigeria Bull.* 29, 1-104, 1963.
- [9] J. M. Gilbert *et al.*, *The geology of ore deposits*, W. H. Freeman, New York, NY, USA, 1986.
- [10] K. C. Burke *et al.*, "Orogeny in Africa." In: Dessauvage T. F. J., Whiteman A. J. (eds), *African geology*, University of Ibadan Press, Ibadan, 583- 608, 1972.
- [11] M. A. Olade *et al.*, "Petrochemistry of the Ilesha amphibolite and Precambrian crustal evolution in the Pan-African domain of SW Nigeria," *Precambrian Res.* 8, 303–318, 1979.
- [12] M. A. Rahaman, "Recent advances in the study of the basement complex of Nigeria," Abstract, 1st Symposium on the Precambrian geology of Nigeria, 1981.
- [13] M. O. Oyawoye, "The basement complex of Nigeria." In: Dessauvage T. F. J., Whiteman A. J. (eds.) *African geology*, University of Ibadan Press, 66–102, 1972.
- [14] N. K. Grant, "Structural distinction between a metasedimentary cover and an underlying basement in the 600 my old Pan-African domain of North-western Nigeria," *Geol. Soc. Am. Bull.* 89, 50–58, 1978.
- [15] R. Jacobson, *et al.*, "The Pegmatite of central Nigeria," *Geol. Survey of Nigeria Bulletin* No. 17S, 1946.
- [16] R. W. Holt, *The geotectonic evolution of the Anka Belt in the precambrian basement complex of N.W. Nigeria*, Unpublished Ph.D. Thesis, the Open University, 1982.
- [17] T. R. Ajayi, "On the geochemistry and origin of the amphibolite in Ife-Ilesha area, SW, Nigeria," *Niger. J. Min. Geol.* 17, 179–196, 1980.
- [18] P. McCurry, "The geology of the Precambrian to lower Palaeozoic rocks of Northern Nigeria – A Review." In: Kogbe C. A. (ed.) *Geology of Nigeria*, Elizabethan Publishers, Lagos, 15–39, 1976.

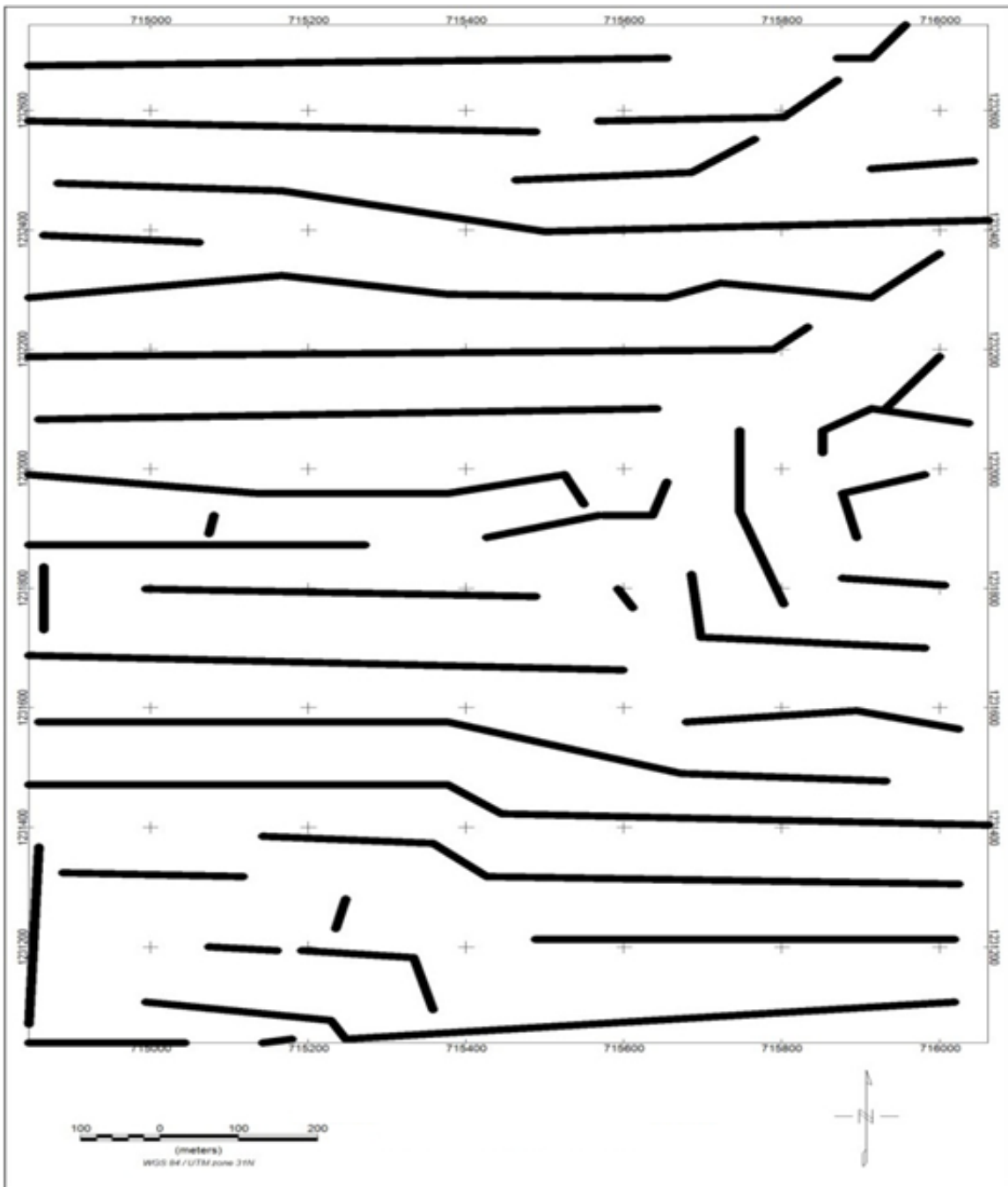


Figure 4. Lineament map of the study area.

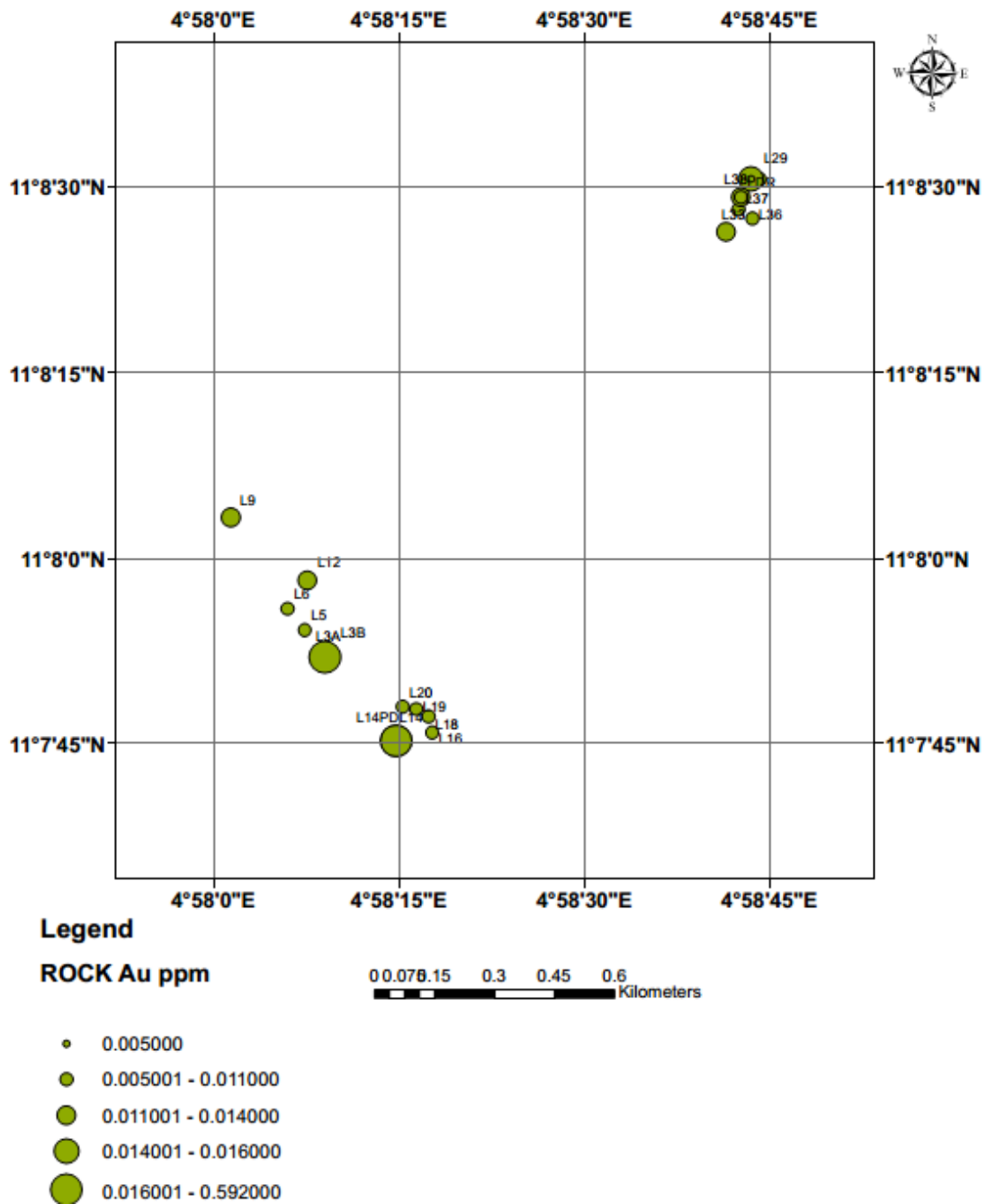
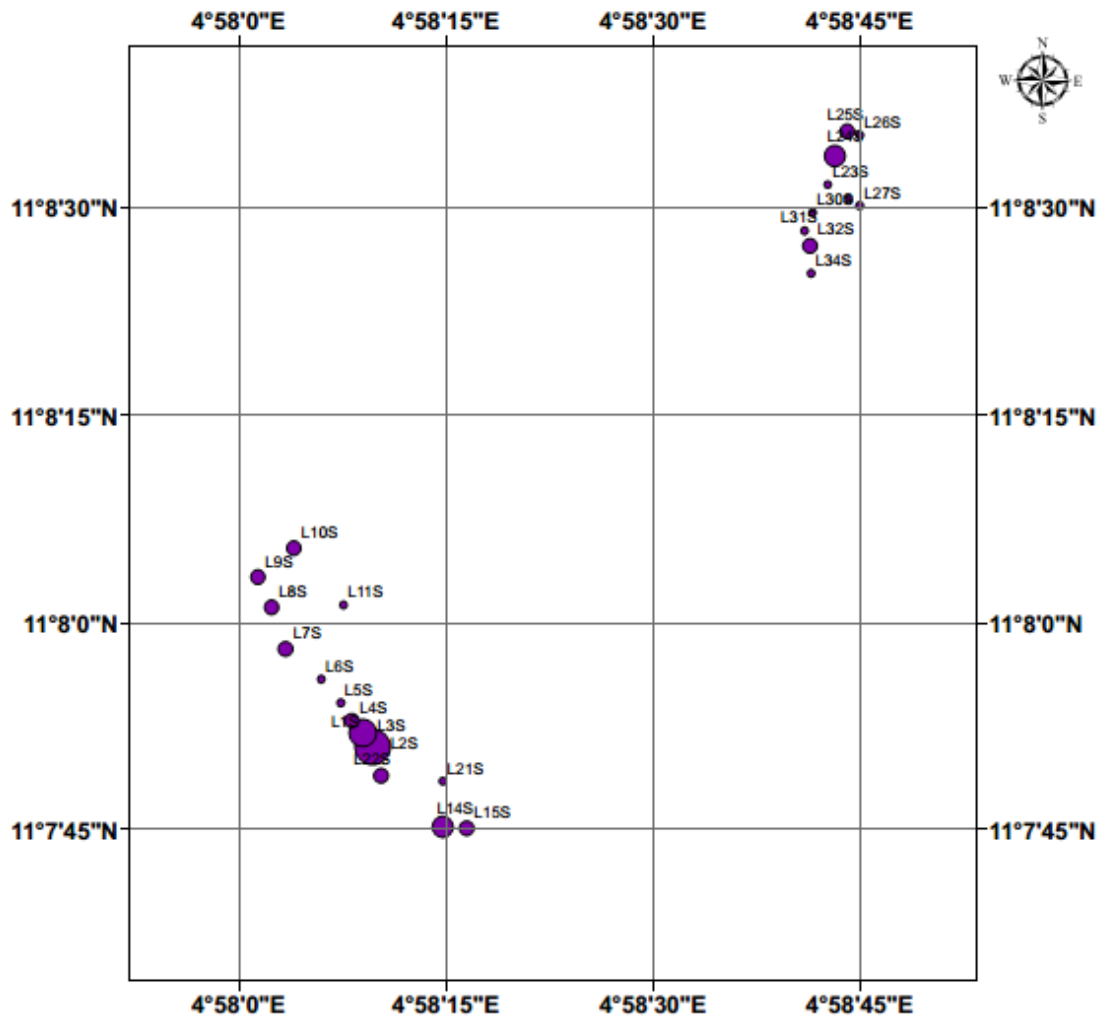
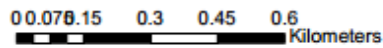


Figure 5. Gold (Au) concentrations in the rock samples collected in the area.



Legend



- 0.007000 - 0.012000
- 0.012001 - 0.022000
- 0.022001 - 0.036000
- 0.036001 - 0.071000
- 0.071001 - 0.160000

Figure 6. Gold (Au) concentrations in the sediments samples collected in the area.

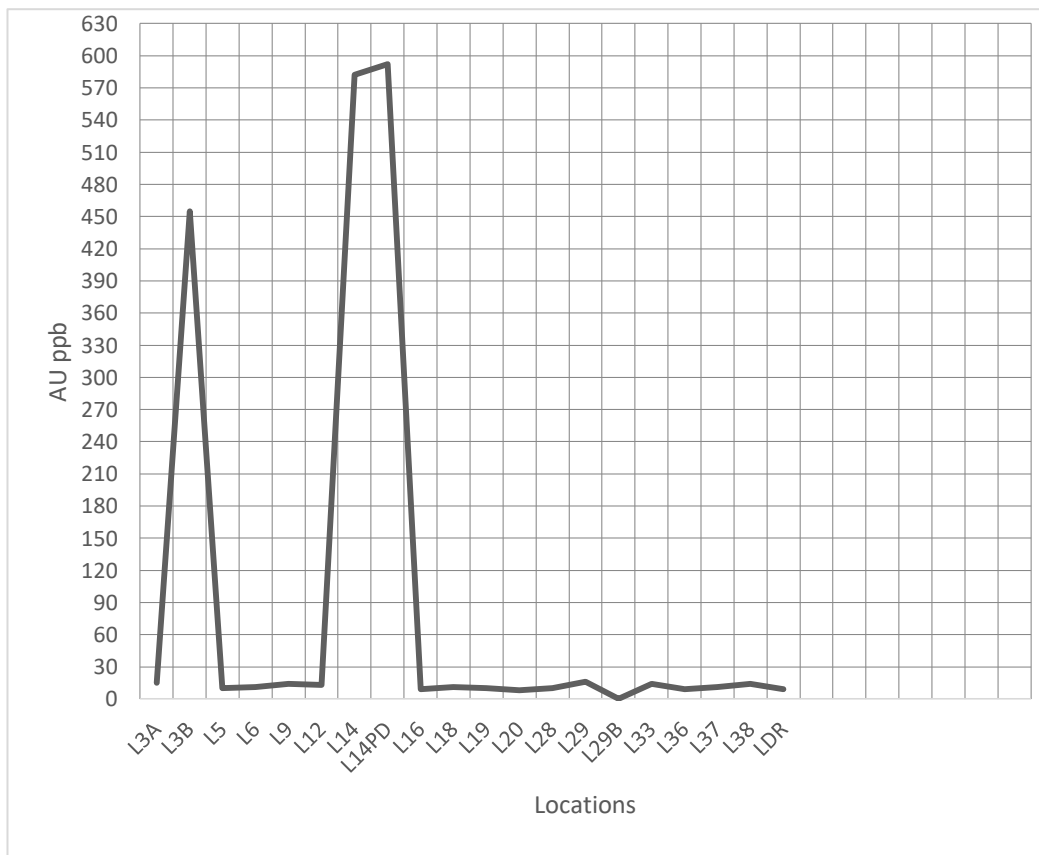


Figure 7. Concentration of Au in Rocks samples at Iri.

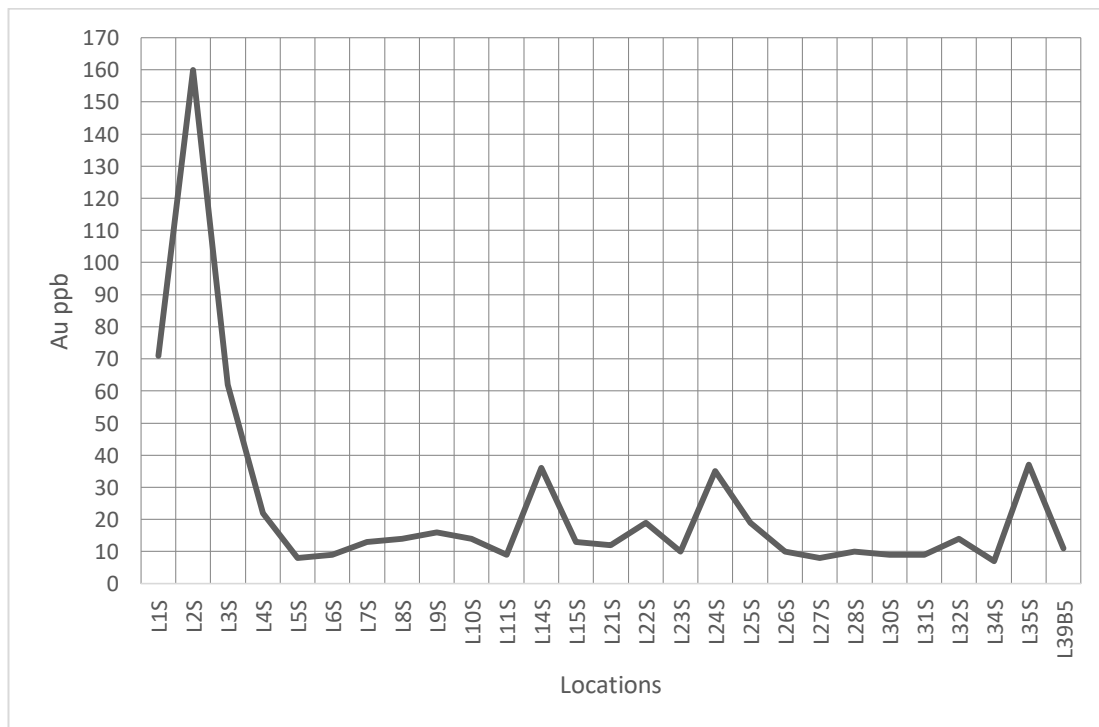


Figure 8. Concentration of Au in the soils samples at Iri.

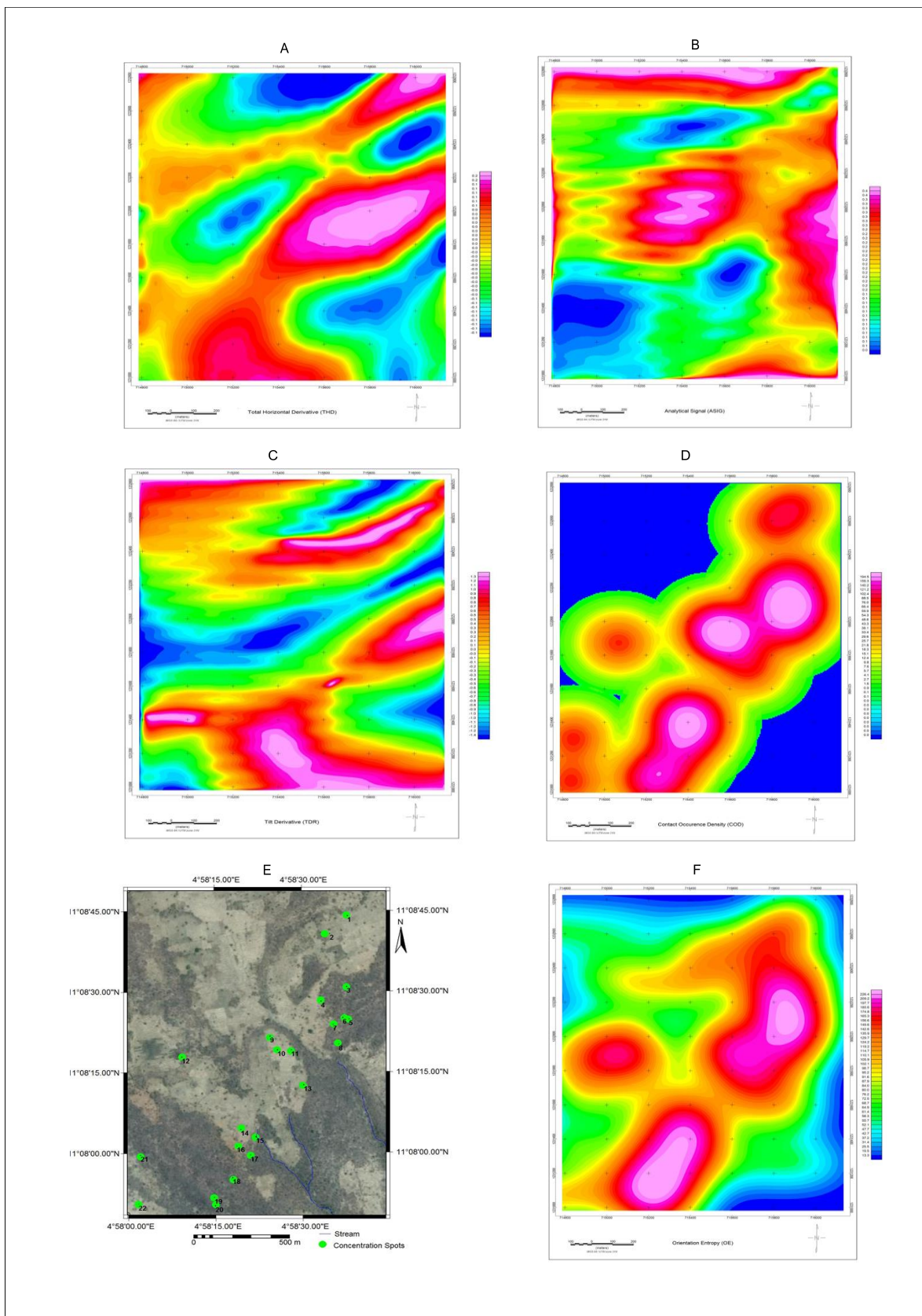


Figure 9. Interpreted aeromagnetic data. (A) First vertical derivative, (B) Analytical signal derivative, (C) Tilt derivative grid, (D) Contact occurrence density, (E) Mineral potential map, (F) Entropy map with line of potential mineralization.

Table 1. Rock sample location coordinates and description.

Location	Rock Types/ Description	Location	Rock Types/ Description
L3A. N11° 51' 51.61" E004° 58' 09.7" Elevation 258m	Existing mining pit. Sample was collected at the foot of the hill. Rock type is Quartz vein, shattered, fine grained and milky white colour.	L18 N11° 07' 47.2" E004° 58' 17.4" Elevation 259m	Quartz vein intrusion in schist, the schist dips at 70°E with noticeable shattering, probably shear zone.
L3B. N11° 07' 51.3" E004° 58' 09.7" Elevation 258m	Rock name = Quartz vein. Texture = massive appearance. Sampling was done 1.6 meter depth of an existing mining pit.	L19 N11° 07' 47.8" E004° 58' 16.4" Elevation 269m	Quartz boulder sampled, the colour is whitish and the texture is fine grained.
L5. N11° 07' 54.2" E004° 58' 07.4" Elevation 256m	Quartz intrusion with massive appearance and whitish colour. Brownish stains of iron oxidation were observed.	L20 N11° 07' 48.0" E004° 58' 15.3" Elevation 268m	Phyllite Schist. Color is dark grey with platy cleavage. Dips at 70°E.
L6. N11° 07' 55.9" E004° 58' 06.0" Elevation 256m	Floated boulder of Quartz was sampled. The texture is fine grained, colour is whitish.	L28 N11° 08' 30.7" E004° 58' 44.2" Elevation 263m	Quartz vein with fine grained texture was sampled. Colour is whitish grey.
L9. N11° 08' 03.3" E004° 58' 01.4" Elevation 259m	Rock name = schist, color is dark grey, texture is fine grained	L29 N11° 08' 30.7" E004° 58' 43.5" Elevation 259m	Quartz vein with fine grained texture was sampled. Colour is whitish grey.
L12 N11° 07' 58.2" E004° 58' 07.6" Elevation 258m	Quartz vein sampled. Color is white to dark grey, fine-grained	L36 N11° 08' 27.5" E004° 58' 43.6" Elevation 264m	Quartz, sampled from boulders mechanically fractured. Color is whitish, texture is fine grained.
L14 N11° 07' 45.2" E004° 58' 14.8" Elevation 262m	Sampling was done at abandoned mines. Rock name = Quartz vein, texture is fine grained and color is whitish grey.	L38 N11° 08' 29.2" E004° 58' 42.7" Elevation 258m	Quartz, sampled from boulders mechanically fractured. Color is whitish, texture is fine grained.
L16 N11° 07' 45.9" E004° 58' 17.7" Elevation 261m	Shattered quartz vein with brown iron oxidation stains. Color is whitish and texture is fine grained.		

Partitioning of iron and zinc in the catchment alluvial sediments of the River Gbako flood plains around Baddegi, central Bida basin, Nigeria

Sidi Aliyu Ahmed^{1*}, Nuhu Musa Waziri², Hadiza Liman Mohammad³,
Mohammed Abubakar Mohammed⁴

¹Department of Geology and Mining, Ibrahim Badamasi Babangida University, Lapai

²Department of Geology, Federal University of Technology, Minna, Nigeria

³Department of Geography, Ibrahim Badamasi Babangida University, Lapai, Nigeria

⁴Division of Graduate Studies and Research, Khazar University, Azerbaijan

*corresponding author email: saakusogi@gmail.com, aasidi@ibbu.edu.ng

Abstract

Partitioning of iron and zinc were studied in the alluvial sediments of the River Gbako floodplains around Baddegi using empirical formulas. The samples were cored from three pits (TR-1, TR-2, and TR-3). A study of the particle size distribution and geochemical analysis were performed. The particle size distribution results indicate that the sediments are sand dominated, having more than 50% sand with smaller percentages of clay and silt. Average partition coefficient values of Fe in the sediments are 1.02, 0.83, and 0.88, and for Zn 1.02, 0.95, and 0.83, for the TR-1, TR-2 and TR-3 sites, respectively. The average velocities of Fe mobilization in the sediments are 0.08 m/day, 0.07 m/day and 0.09 m/day for TR-1, TR-2 and TR-3, respectively, and for Zn mobilization are 0.07 m/day, 0.07 m/day and 0.09 m/day, for TR-1, TR-2 and TR-3, respectively. The metals are more preferentially partitioned in the sediments than the water percolating through them, which has an average hydraulic conductivity (K) of 4.2 m/day. The partition behavior of the metals is used to explain contaminant transportation in the alluvial sediments of the River Gbako floodplains around Baddegi and also explains the attenuation of pollutants and the process of natural groundwater purification within the shallow alluvial aquifers of these floodplains.

Index Terms: partition coefficient, hydraulic conductivity, alluvial sediments, floodplain, Nigeria

1. Introduction

1.1 The importance of trace metals

Trace metals occur naturally, and are important for characterizing both rocks and sediments. Certain anthropogenic factors may increase the concentration levels of trace metals, causing the sediments and/or groundwater to become toxic. The form and behavior of these metals in sediments can affect the geochemical processes of water/sediment interaction. Trace metals constitute an ill-defined group of inorganic chemical hazards, and those most commonly found at contaminated sites are lead (Pb), chromium (Cr), arsenic (As), zinc (Zn), cadmium (Cd), copper (Cu), mercury (Hg), and nickel

(Ni).³ Factors that may influence the form, concentration, and distribution of metal contaminants include sediment and groundwater chemistry, as well as local transport mechanisms.³ Some plants have a significant influence in retarding the mobility of metals introduced into sediments, and the idea of using metal-accumulating plants to remove heavy metals and other compounds was first introduced in 1983, but the concept has actually been implemented for the past 300 years on wastewater discharges.^{9,10}

It is important to know the partition behaviour of metals, as this determines their availability and biodiversity. Sediments are the major sink for

heavy metals released into the environment by either anthropogenic or lithogenic processes.⁴ Heavy metal contamination of sediments may pose risks and hazards to humans and the ecosystem through: direct ingestion or contact with contaminated sediments, the food chain (sediments-plants-humans or sediments-plants-animals-humans), drinking of contaminated groundwater, reduction in food quality (safety and marketability) via phytotoxicity, reduction in the suitability of land for agricultural production leading to food insecurity, and land tenure problems.^{2,10} When sediments become contaminated with trace elements, the groundwater becomes a reservoir for them. Sediment/water interactions remain the only significant way of explaining the geochemical processes that determine if trace metals are mobile or immobile. Depending on their chemical properties, trace metals can be conservative and find their way into the groundwater system. Fertilizer application is one of the ways sediments can be enriched with trace elements. The application of such compounds enriches the sediments with potassium, calcium, chloride, nitrate and phosphate.¹² When applied in excessive amounts on fields or improperly stored in stockpiles, inorganic fertilisers may lead to unacceptable or even toxic concentrations of chemical constituents in local, regional and even national groundwater systems.¹⁵ The aim of this research is to study the mobilization pattern of Fe and Zn in the alluvial sediments of the River Gbako floodplains around Baddegi, in Nigeria.

1.2 The study area

The study area is mainly low lying, and slopes towards the banks of the River Gbako. The flood plain of the river is extensive, with on average a uniform elevation across the study area. The average elevation in the area is 55 m above sea level, as calculated from a topographical map of the area. The area is mainly drained by the River Gbako, which is tributary to the River Kaduna. The temperature in this area is relatively high, between 33C and 34C throughout the season, which affects the rate of evaporation; in addition, intensive agricultural activities contribute to the evaporation.

2. Materials and methods

2.1 Sediment sampling and description

Samples were cored from three pits (TR-1: 0.3m deep, TR-2: 2.0m, and TR-3: 1.4m). The sediment samples were collected and macroscopically described at 0.1m intervals (TR-1) and 0.2m intervals (TR-2 and TR-3) from the surface to the bottom depth for each pit. All the samples were stored in polythene bags. Chemical analysis was done after the samples were processed.

2.1.2 Sieve analysis

Twenty (21) sediment samples were subjected to mechanical sieve analysis following the standard procedures.⁴

2.2 Estimation of hydraulic conductivity, K

The hydraulic conductivity (K) was estimated from the sediment particle size distribution graph using an empirical formula.¹ This formula is:

$$K = C (d_{10})^2 \quad (1)$$

where K is the hydraulic conductivity in cm/sec, C is a constant with units of $(\text{cm} \cdot \text{sec})^{-1}$, and d_{10} is the grain diameter in centimetres, so that grains this size or smaller represent 10% of the sample mass. C varies from about 40 to 150 for most sands. C is at the low end of this range for fine, widely graded sands, and C is near the high end of the range for coarse, narrowly graded sands.³

2.3 Chemical analysis of sediments and groundwater

The collected samples as well as groundwater samples were subjected to laboratory chemical analysis. The sediments were processed by grinding in a mortar after drying them at room temperature for 48 hours. The samples were then digested and analysed with AAS for Fe and Zn. All the groundwater samples were analysed for major and minor elements and trace elements (Fe and Zn).

2.4 Partition coefficient values of Fe and Zn

An empirical formula was used to calculate partition coefficients of Fe and Zn. This

calculation involves dividing the concentration of the metals in the sediment samples cored from the three pits by the concentration of such metals in the groundwater samples from the pits. Thus, the partition coefficient is represented the following formula:⁷

$$D_i = \frac{C_i^{solid}}{C_i^{liquid}} \quad (2)$$

where D_i is the partition coefficient, C_i^{solid} is the concentration of the element in sediment samples, and C_i^{liquid} is the concentration of the element in groundwater samples. The velocity of Fe and Zn in the sediments was also determined using the equation below:

$$V = \frac{n}{n+(1-n)\frac{C_i^{solid}}{C_i^{liquid}}} V_{liquid} \quad (3)$$

where V is velocity of the metals in the solid (sediment or soil), n is the porosity of the sediment, and V_{liquid} is velocity of the water (the hydraulic conductivity).

3. Results and discussion

The results concerning the partition behaviour of Fe and Zn in the sediment samples are presented in **Figures 1, 2** and **3**, while the mobility of Fe and Zn in the sediments samples is illustrated in **Figures 4, 5**, and **6**.

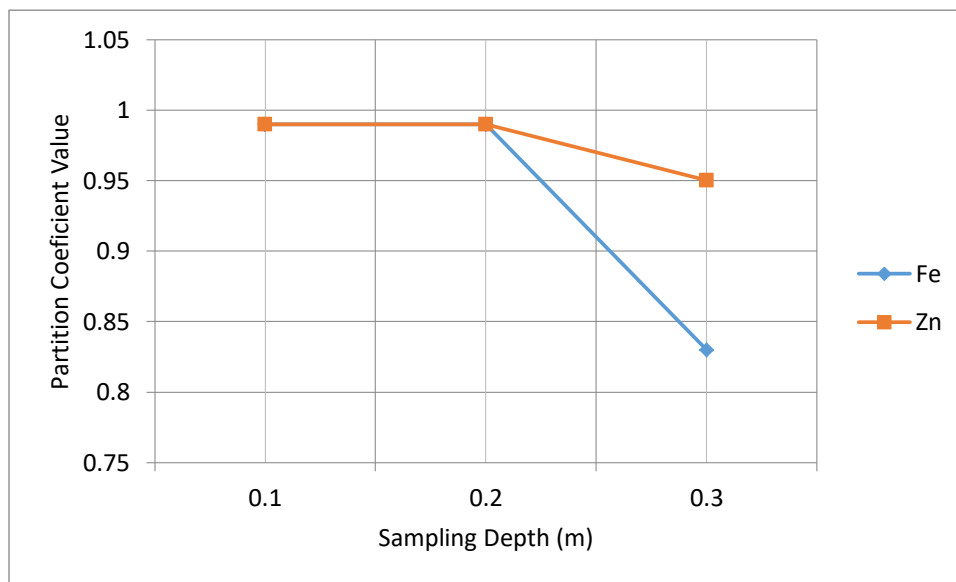


Figure 1. Partition behavior of Fe and Zn in sediment samples cored at TR-1.

According to Raymond *et al.*³ sediments may become contaminated by the accumulation of heavy metals and metalloids through emissions from rapidly expanding industrial areas, mine tailings, disposal of high metal wastes, leaded gasoline and paints, application of fertilisers, animal manures, sewage sludge, pesticides, wastewater irrigation, coal combustion residues, spillage of petrochemicals, and atmospheric deposition. Trace metals like Fe and Zn can be concentrated in sediments through adsorption and ion exchange processes.

The characteristic curves for the two metals (Fe, Zn,) with depth shows a similarity in the pattern

of mobility through the sediment horizons. Heavy metals in the sediments due to anthropogenic sources tend to be more mobile, hence more bioavailable, than pedogenic or lithogenic ones.^{11,12} In TR-1, Fe and Zn partition similarly in the first two sampling intervals. However, at a depth of 0.3m the partition behaviours of Fe and Zn become inconsistent and varied. Zn can interrupt the activity in sediments, as it influences negatively the activity of microorganisms and earthworms, thus retarding the breakdown of organic matter.¹³ Zinc occurs naturally in sediments (about 70 mg kg⁻¹ in crustal rocks).⁷ Fe shows a lower partition coefficient value, indicating a possible decrease in the reactivity of

Fe with the sediments due to a change in the characteristic particle size of the sediments, which allows Fe to attain almost conservative status.

the complex nature of the characteristic grain sizes of the sediments cored from the pits. Zn is less reactive at shallower depths of 0-1m, while Fe becomes less reactive at the deeper depth of 1.2m. This condition can explain the level of remixing in sediments within the active floodplains.

In TR-2, the pattern is quite irregular, providing a different pattern for the elements. The irregularities in the partition pattern may indicate

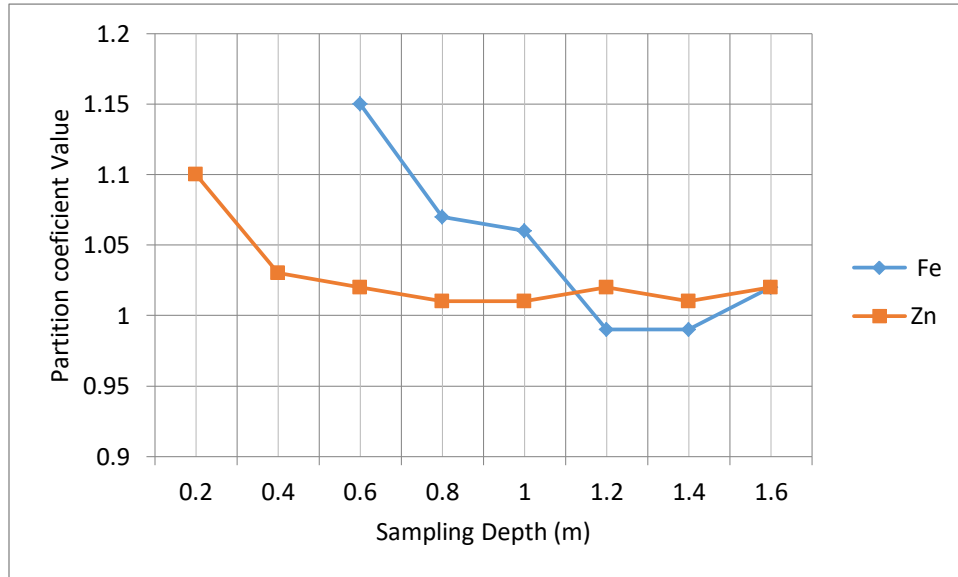


Figure 2. Partition behavior of Fe and Zn in sediment samples cored at TR-2.

In TR-3, Fe has stable mobility behavior, maintaining the same partition coefficient values, in contrast with Zn which exhibits a sharp drop in

the first horizon before stabilising to maintain a similar pattern.

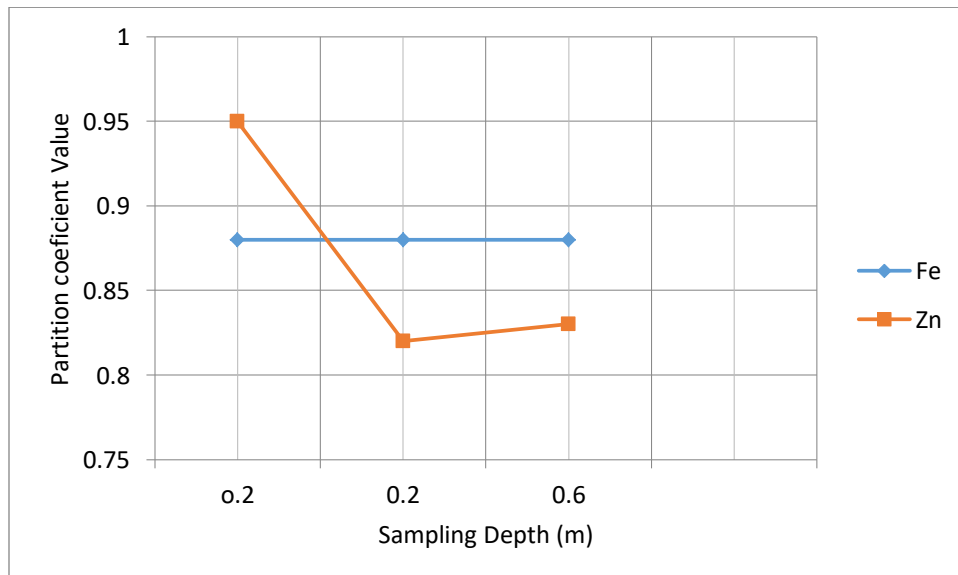


Figure 3. Partition behavior of Fe and Zn in sediment samples cored at TR-3.

Fe and Zn mobilities in the sediments (see **Figures 4, 5** and **6**) are uniform, except in a few situations. In TR-1, a uniform mobility of Fe and Zn at 0.06m/sec is observed between 0.2-0.6m. The mobilities increase to 0.07m/sec and continue steadily at that level, showing preferential attachment to the sediments. In TR-2, Fe maintains a consistent mobility of 0.08m/sec

throughout the sampling horizon, while Zn exhibits a slower mobility in the upper horizon before attaining the same rate as Fe at a depth of 0.4m. In TR-3, both Fe and Zn have the same mobility of 0.09m/sec throughout the sediments, which may be explained by the uniformity in the sediments' grain sizes.

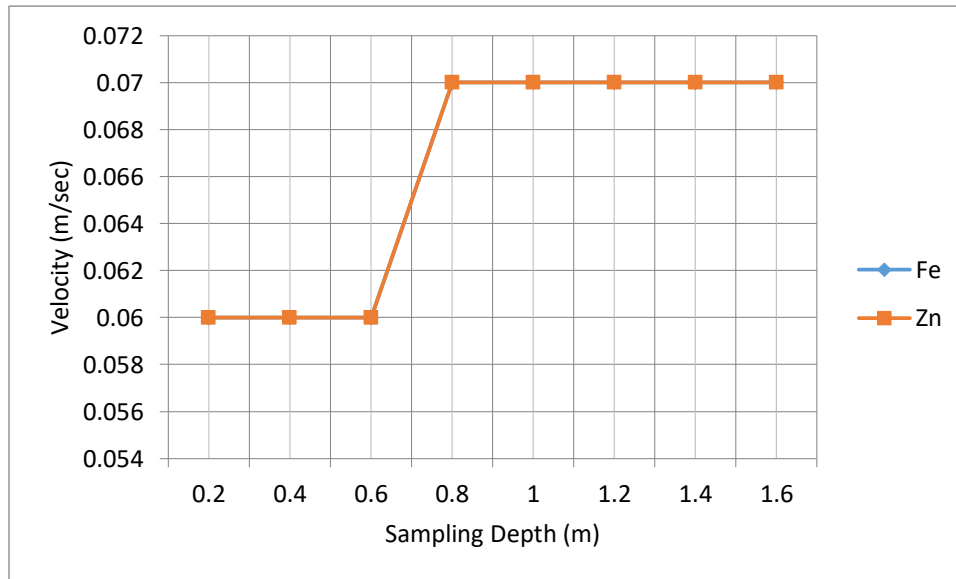


Figure 4. Velocity of Fe and Zn in sediment samples cored in TR-1.

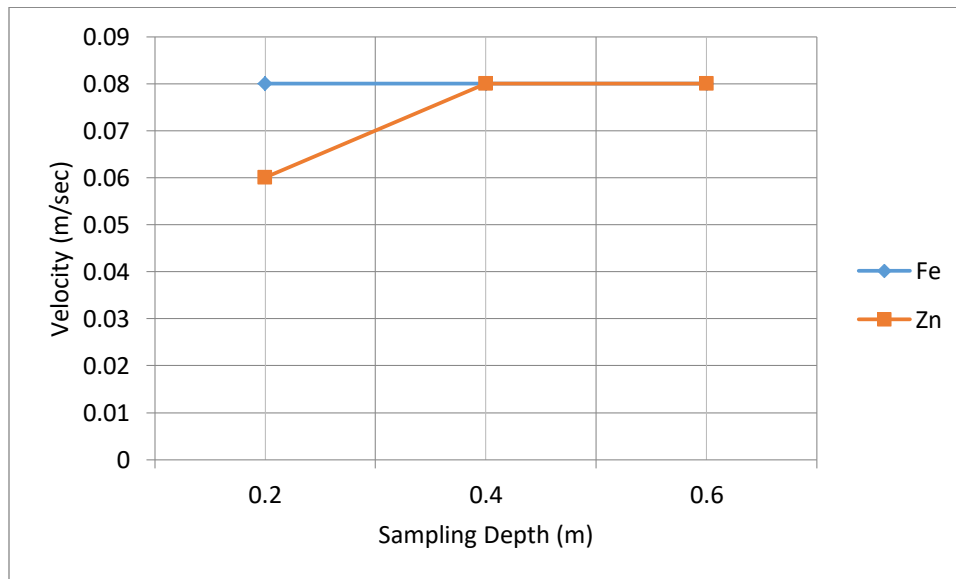


Figure 5. Velocity of Fe and Zn in sediment samples cored in TR-2.

Generally, the influence of the grain size on the mobility of metals in the sediment horizons is significant, as revealed by the patterns of concentration levels of the trace metals with depth in the sediment horizons (see **Figures 7, 8**

and **9**). The principal factors controlling the mobility of the elements in the sediment horizons in the area are the particle size fractions, grain geometry, absorptive capacity and reactivity of the metals in the sediment. Under certain

conditions, metals added to sediments through the application of biosolids can leach downwards through the sediment profile, and can have the potential to contaminate groundwater.¹³ Sediments need to be protected from heavy metal contamination, and phytostabilization is advantageous because the disposal of hazardous

material/biomass is not required, and it is very effective when rapid immobilization is needed to preserve the ground and surface waters.¹⁹ Phytostabilization, also referred to as in-place inactivation, is primarily concerned with the use of certain plants to immobilize soil, sediment and sludges.¹⁹

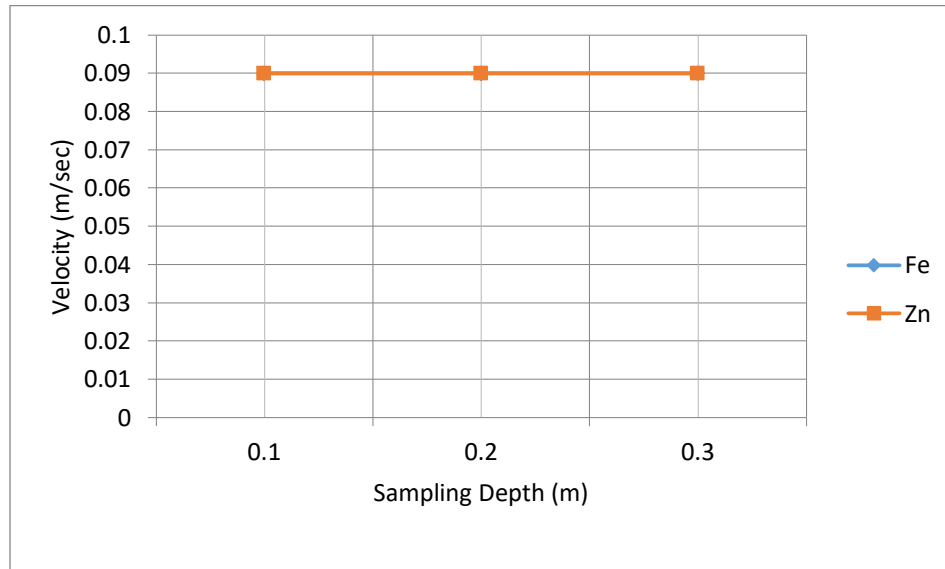


Figure 6. Velocity of Fe and Zn in sediment samples cored in TR-3.

4. Conclusion

The partition behaviour of Fe and Zn in the floodplain sediments of the River Gbako have been studied to investigate their mobility and transport mechanisms. The transport of a heavy metal in soil depends significantly on the chemical form and speciation of the metal. Once in the soil, heavy metals are initially adsorbed by fast reactions, followed by slow adsorption reactions, and are therefore redistributed into different chemical forms with varying bioavailability, mobility, and toxicity. This distribution is believed to be controlled by reactions of heavy metals in soils such as mineral precipitation and dissolution, ion exchange, adsorption, and desorption, aqueous complexation, biological immobilization and mobilization.

References

- [1] A. Hazen, "Discussion: Dams on sand foundations," *Transactions American Society of Civil Engineers* 73, 199, 1911.
- [2] A. Kabata-Pendias *et al*, *Trace Metals in Soils and Plants*, Boca Raton, Fla, USA CRC Press 2001.
- [3] A. Raymond *et al*, "Heavy metals in contaminated soils: A review of sources, chemistry, risks and best available strategies for remediation," *International Scholarly Research Notices* ID 402647, 2011.
- [4] American Society for Testing and Materials, *ASTM Standard Test method for Sieve Analysis of Fine and Coarse Aggregates*, ASTM International, West Conshohoken, PA, 2019.
- [5] C. Garbisu *et al*, "Phytoextraction: a cost-effective plant-based technology for the removal of metals from the environment," *Bioresource Technology* 77(3), 229-236, 2001.
- [6] C. Keller *et al*, "Trace metal leaching through a soil-grassland system after sewage sludge application," *Journal of Environmental Quality* 31, 1550–1560, 2002.
- [7] F. Albarede, *Geochemistry: An Introduction*, Cambridge University Press, UK.

- [8] K. M Greany, *An assessment of heavy metal contamination in the marine sediments of Las Perlas Archipelago, Gulf of Panama*, Unpublished M.S. thesis, School of Life Sciences, Heriot-Watt University, Edinburgh, Scotland, 2005.
- [9] L. Candela, *et al*, *Agricultural threats to groundwater quality*, IHP-UNESCO, International Centre for Advanced Mediterranean Agronomic Studies (CIHEAM) and Technical University of Catalonia, Zaragoza, Spain, 251, 1998.
- [10] M. J McLaughlin *et al*, “Review: a bioavailability-based rationale for controlling metal and metalloid contamination of agricultural land in Australia and New Zealand,” *Australian Journal of Soil Research* 38, 1037-1086, 2000.
- [11] M. Kaasalainen *et al*, Use of sequential extraction to assess metal partitioning in soils. *Environmental Pollution* 126, 225-233, 2003.
- [12] N. T. J. Basta. *et al.*, “Trace element chemistry in residual-treated soil: key concepts and metal bioavailability,” *Journal of Environmental Quality* 34, 49-63, 2005.
- [13] P. G. C. Campbell, “Cadmium - A priority pollutant,” *Environmental Chemistry* 3(6), 387-388, 2006.
- [14] R. A. Wuana *et al*, *Heavy Metals in “Contaminated Soils: A Review of Sources, Chemistry, Risks and Best Available Strategies for Remediation,” International Scholarly Research Notices* ID 402647, 2011.
- [15] R. F. Charles, *Groundwater Science*, New York, Academia Press, 2002.
- [16] R. J. Henry, *An overview of the phytoremediation of lead and mercury*, United States Environmental Protection Agency Office of Solid Waste and Emergency Response Technology Innovation office, Washington, DC, USA, 2000.
- [17] T. Kirpichtchikova *et al*, “Speciation and solubility of heavy metals in contaminated soil using X-ray micro fluorescence,” *Geochimica et Cosmochimica Acta* 70, 2163–2190 2006.
- [18] UNESCO, *International Glossary of Hydrology* (Second revised ed.), Paris, France, 1992.
- [19] USEPA, *Introduction to phytoremediation*, Tech. Rep. EPA 600/R-99/107, United States Environmental Protection Agency, Office of Research and Development, Cincinnati, Ohio, USA, 2000.

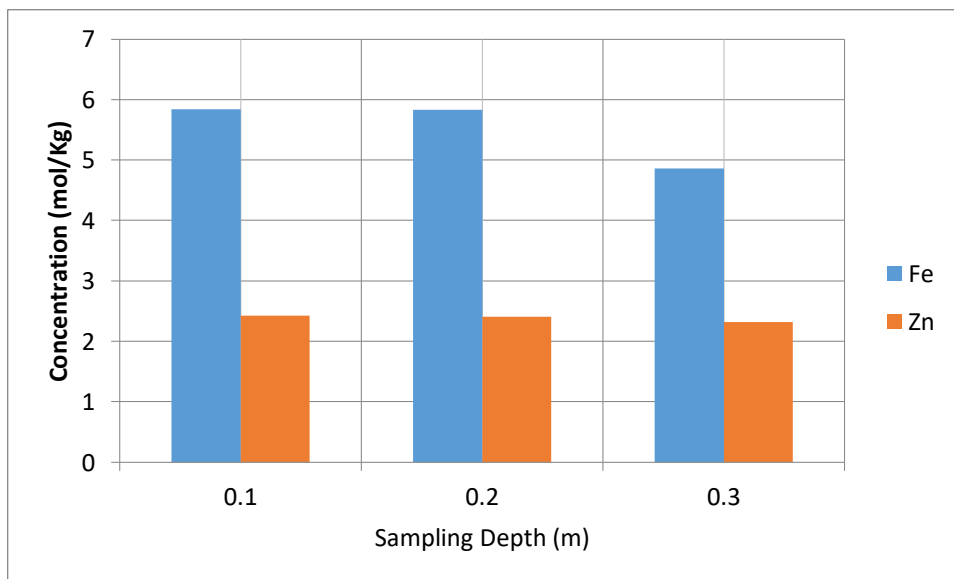


Figure 7. Fe and Zn in sediment samples cored in TR-1.

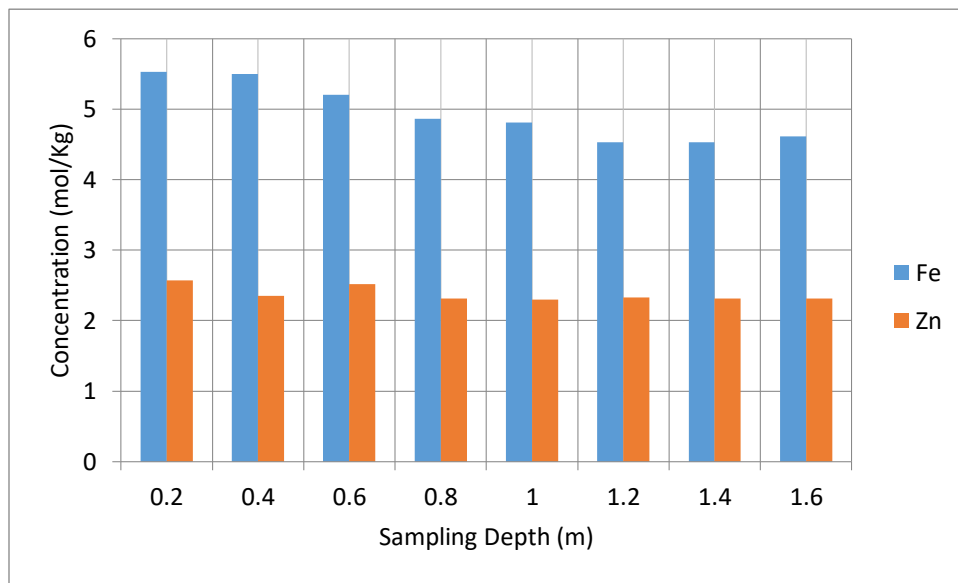


Figure 8. Fe and Zn in sediment samples cored in TR-2.

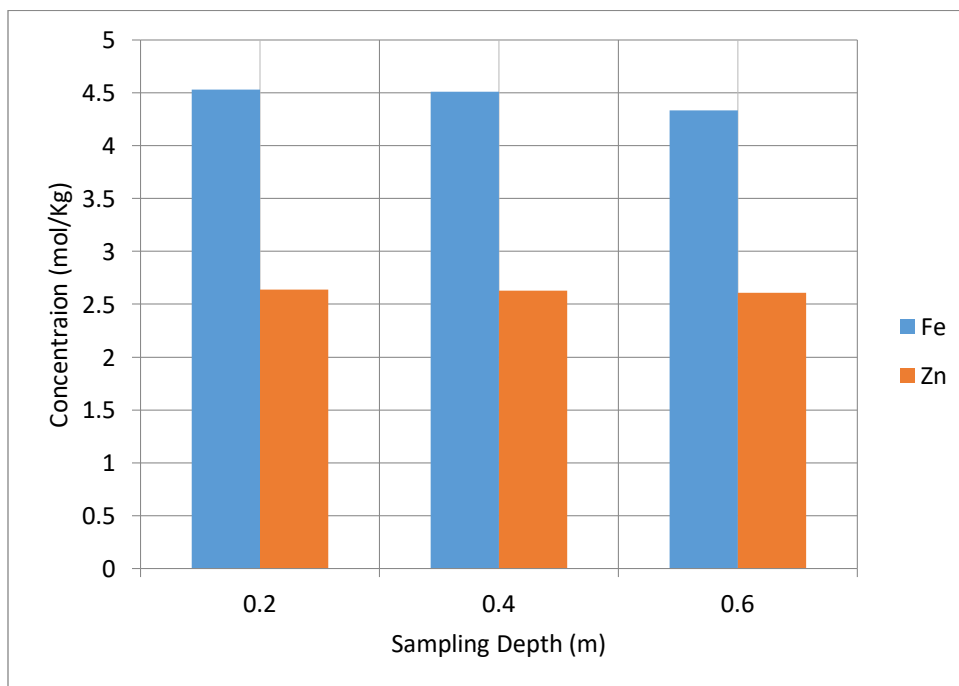


Figure 9. Fe and Zn in sediment samples cored in TR-3.

Different synthetic approaches, designs and applications of metal-organic frameworks with selected organic ligands

Ubaidullah Hj. Mat Yassin¹, Malai Haniti Sheikh Abdul Hamid¹, Zainab Ngaini² and Ai Ling Tan^{1*}

¹Chemical Sciences Programme, Faculty of Science, Universiti Brunei Darussalam,
Jalan Tungku Link, BE 1410, Brunei Darussalam

²Faculty of Resource Science and Technology, Universiti Malaysia Sarawak,
Kota Samarahan, 94300, Malaysia

*corresponding author email: ailing.tan@ubd.edu.bn

Abstract

Metal-organic frameworks (MOFs) bearing organic ligands with various functional groups and substituents give rise to MOFs of unique crystal structures and topologies. A number of potential applications have been considered for these materials in a wide array of scientific fields, such as in the adsorption of industrially-relevant gases, as heterogeneous catalysts for various organic reactions, as photoluminescent materials, and as antibacterial agents. This review highlights the utility of selected groups of organic ligands in the assembly of main group metals, transition metals, lanthanides and actinides, to generate MOFs of diverse structures in the solid-state, with special attention paid to ligands bearing the carboxylate-, pyridyl-, ether-, imine (Schiff base) moieties, as well as mechanically interlocked molecules (MIMs).

Index Terms: carboxylate, coordination polymers, mechanically interlocked molecules, metal-organic frameworks, pyridyl, Schiff bases

1. Introduction

Metal-organic frameworks (MOFs) are a class of hybrid compounds, composed of metal nodes and organic/inorganic linkers oriented in such a way as to bridge metal ions to generate multi-dimensional, extended structures. Although this class of hybrid compounds was present long before its reported discovery, it was not until 1995 that the renowned chemist Omar M. Yaghi pioneered and extended the work on these unique compounds, which were later termed coordination polymers.¹ This term was first coined in 1916; however, probing the crystalline structure of coordination polymers by X-ray diffraction was not yet possible and so the term was not widely used at that time. MOFs are a subclass of coordination polymers that possess two- or three-dimensional network structures with large internal surface area, high porosity, and thermal stability, which contribute to their exceptionally low densities. Due to these unique intrinsic properties, such compounds are specifically included in a

recently established field of chemistry, known as reticular chemistry. Reticular chemistry is broadly defined as “*the chemistry that utilizes strong molecular bonds to stitch molecules together*”. However, Yaghi himself defined it as the chemistry that concerns linking molecular units into predetermined structures in a repeated manner, held by strong interactions.² MOFs are constructed from coordination and intermolecular bonds, such as London dispersion forces, π -electron stacking, and hydrogen bonds. By exploiting these bonds, frameworks can be constructed. The nature of the metals and ligands employed plays a big role in assembling MOFs. The metal’s coordination number, oxidation state, geometry and Lewis acidity, and the ligands’ flexibility/rigidity, functional groups, bulkiness and Lewis basicity dictate the structure of the resulting frameworks. MOFs classified under reticular chemistry, are porous and thermally stable.³ The porosity of a MOF is a consequence of the ligand adopting specific coordination

modes and geometry with respect to the metal centres, and the significance of MOFs is mainly related to the presence of these pores. Since their first introduction into the world of materials science, MOFs have received much attention from materials scientists and synthetic chemists alike across the globe. Diverse applications of the synthesized MOFs have been investigated, particularly in catalysis and molecular magnets. Additionally, MOFs are also utilized in light-emitting diodes (LEDs) and sensors, in supercapacitors, heterogeneous catalysis, rechargeable batteries, gas separation and biomedicine as potential drug carriers.⁴

There are generally four classes of MOFs, distinguished according to their dimensions, which are nanoparticles, 1D, 2D, and 3D.² The simplest of these classes is the nanoparticle, which is an infinitesimal-sized particle having a diameter of 1 to 100 nm. Second, 1D MOFs - which can exist as linear chains, zigzags, helices, ladders, and tubes - are arranged in a unidirectional manner, with the possible pores occupied by modest-sized molecules.⁵ The third class is the 2D MOFs, which are monolayer in nature, and have a structural topology resembling sheets or layered structures arranged in stacks due to weak interactions. Fourth, 3D MOFs are highly porous and thermally stable networks, whose frameworks spread in three dimensions as a result of tri-directional coordination bonds. These 3D MOFs are of major interest in the extensive study of MOFs, since the pores can accommodate diverse types of molecules for a variety of purposes. Theoretically, an infinite number of MOFs can be prepared simply by varying the combinations and permutations of the metal nodes and ligands used. Inorganic and organic ligands both play a crucial role in building MOFs with specified intrinsic properties, and often, by incorporating a mixture of different metals or ligands in one pot, MOFs of unprecedented characteristics can be tailored.

2. Methods of MOF synthesis

A variety of MOFs can be synthesized by employing different synthetic approaches, and the choice of method generally influences the nature of the MOF formed. The development of

alternative synthetic routes in place of the conventional heating method has enabled the formation of MOFs with interesting network topologies and porosities. Five main synthetic routes have been explored, and these methods include 1) conventional heating and room temperature synthesis, 2) electrochemical synthesis, 3) microwave-assisted heating synthesis, 4) mechanochemical synthesis, and 5) sonochemical synthesis. The choice of methods determines the reaction time, yield, size and morphology of the particles formed. The different synthetic routes mentioned above are summarized below.

2.1 Conventional method

The term conventional method is typically ascribed to the use of electric heating to drive a chemical reaction at temperatures ranging from below to above the boiling point of the solvent used. Reactions above the boiling point of the solvent are called solvothermal reactions, since they occur at elevated temperatures in a closed vessel, enabling a rise in autogenous pressure within the reaction system. Non-solvothermal, or ubiquitously named 'conventional', reactions occur at temperatures below or at the boiling point of the solvent. Room temperature reactions are also classed under the conventional method. The assembly of MOFs can be accomplished even at room temperature, simply by direct precipitation, and by the layering of reactant solutions, followed by slow diffusion or evaporation of the solvent. The conventional method is a good approach for growing single crystals of compounds that do not precipitate instantaneously upon mixing, or that can be recrystallized. Several previously determined MOFs, such as MOF-5 and MOF-177,^{6,7} have been synthesized at room temperature in order to compare the crystallinity, as well as the thermal and chemical stabilities, of the MOFs formed *via* different methods. The room temperature synthesis of MOF-5 is shown in *Figure 1*.

2.2 Electrochemical method

MOF synthesis by the electrochemical method was initially pursued for the purpose of introducing metal ions *via* anodic dissolution to

the reaction medium without including the anions, since it was beneficial in the context of large-scale manufacturing processes. Additionally, this method permits the process to run continuously with higher solid content as compared to typical reactions. The method has been used for the synthesis of a number of prominent MOFs, such

as HKUST-1⁸ and several Cu- and Zn-carboxylates and imidazolates.⁶ **Figure 2** illustrates the reaction conditions for the synthesis of HKUST-1 *via* the electrochemical method using copper metal plates as the electrodes. The crystal structure of HKUST-1 is shown in **Figure 3**.⁹

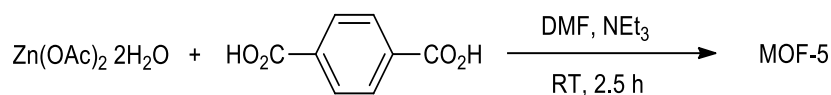


Figure 1. Room temperature synthesis of MOF-5.⁷

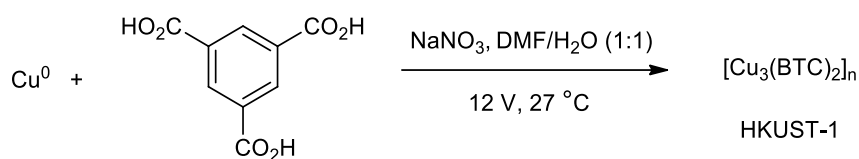


Figure 2. Electrochemical synthesis of HKUST-1.⁸

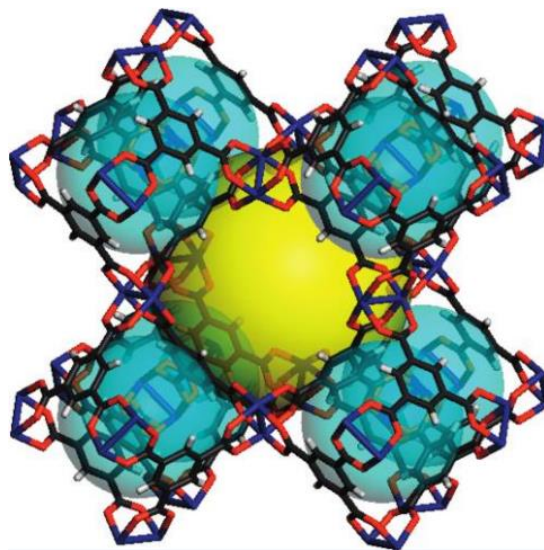


Figure 3. Crystal structure of HKUST-1, depicting the formation of a three-dimensional framework and the presence of major (yellow sphere) and minor (blue spheres) pores. Reproduced with permission from Feldblyum *et al.*⁹ Copyright 2011 American Chemical Society.

2.3 Microwave-assisted synthesis

Synthesis using the microwave-assisted approach is quite a novel method in the field of MOF chemistry, as its utility has been established mainly in organic chemistry. Microwave-assisted synthesis utilizes the coupling interaction between photons in the microwave region of the electromagnetic spectrum and mobile electric

charges. These include metal ions and polar solvent molecules present in the reaction system. Since heating *via* microwave irradiation involves direct interaction between the microwave and the ions or polar molecules (dielectric heating), this method offers a very energy-efficient alternative to the conventional method. The choice of solvent plays a critical role because different solvents

possess different dielectric constants, and thus interact differently with microwave radiation. Similarly to the conventional method, the microwave-assisted method can take place at temperatures below the boiling point of the solvent, as well as under solvothermal conditions.

In MOF chemistry, the microwave-assisted method is commonly employed for the purpose of accelerating the rate of reaction and crystallization of the MOF product, for forming nanosized materials, for improving the purity of the product, for better selectivity, and also for synthesizing desired polymorphs. The past few years have seen a rapid rise in MOF synthesis *via* the microwave-assisted method. Some of these MOFs are Cr-MIL-100, Co-MOF-74¹⁰ and [Ln(Hpmd)(OH)₂] (where Ln³⁺ = Eu³⁺, Gd³⁺ and Tb³⁺; H₄hpmd = 1,4-phenylenebis(methylene)diphosphonic acid).¹¹ The synthesis of Co-MOF-74 using the microwave-assisted method is depicted in **Figure 4**.

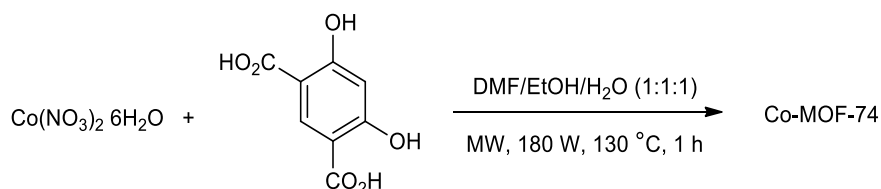


Figure 4. Microwave-assisted synthesis of Co-MOF-74.¹⁰

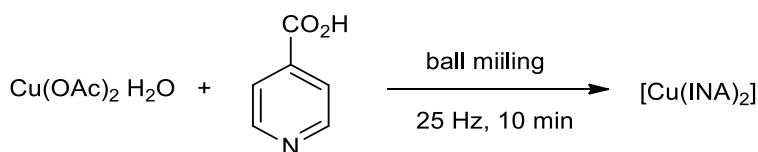


Figure 5. Mechanochemical synthesis of [Cu(INA)₂].¹³

2.4 Sonochemical method

Sonochemical synthesis utilizes high-energy ultrasound to initiate the reaction. Ultrasonic waves generated by the source interact with the liquid medium, forming regions of alternating pressures, which are referred to as compression (high pressure) and rarefaction (low pressure) zones. Since the wavelength of the ultrasonic waves is much longer than the size of the molecules, these waves do not interact directly with the reactant molecular species.

2.4 Mechanochemical method

Mechanochemistry makes use of mechanical force to drive a chemical reaction, which occurs following the dissociation of intramolecular bonds due to mechanical breakage. There are several ways in which mechanochemical synthesis can be carried out, including ball mill grinding, neat grinding, as well as liquid-assisted grinding. The mechanochemical method features a process which is either solvent-free or makes minimal use of solvents, and is considered a green alternative to chemical synthesis. In addition to the neatness of the process, mechanochemical synthesis may prove to be the most suitable method for the bulk preparation of industrially-relevant MOFs, due to the comparatively shorter reaction times needed to obtain high quantitative yields. HKUST-1, MIL-78, MOF-2, MOF-3,¹² and [Cu(INA)₂]¹³ are several examples of MOFs that have been prepared by this method. For example, the mechanochemical synthesis of the MOF [Cu(INA)₂] (where INA = isonicotinate) by ball milling is illustrated in **Figure 5**.

Consequently, cavities are formed, and eventually collapse upon reaching a maximum size. This process leads to the formation of hotspots within the medium that can reach up to 5000 K and 1000 bar for a short time, which is sufficient to drive chemical reactions. Due to its tendency to form nanocrystalline particles, coupled with its environmentally friendly and energy-efficient nature, sonochemical synthesis has been applied for synthesizing many MOF materials, such as IRMOF-9, IRMOF-10, Fe-MIL-53, MOF-5 and

MOF-177.^{6,9} The reaction conditions used in the sonochemical synthesis of MOF-5 are indicated in **Figure 6**.

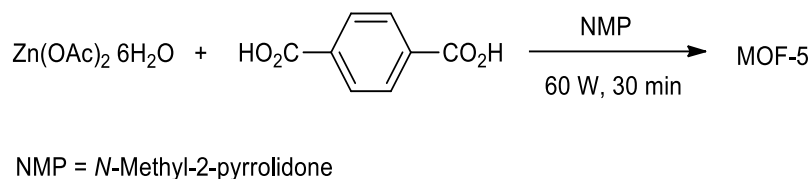


Figure 6. Sonochemical synthesis of MOF-5.¹⁰

3. Linkers in MOF construction

In MOF chemistry, the term *ligand* is often alternatively referred to as a *linker* or *strut*. Organic ligands constitute the majority of the reported MOFs. An array of ligands bearing diverse types of moieties have been introduced as linkers, such as O-, N-, S- and P-based molecules. O- and N-bearing molecules form the majority of the MOF linkers, particularly rigid benzene-*n*-carboxylic acid derivatives, ether and pyridyl derivatives. Additionally, other N-bearing aromatic compounds, *e.g.* pyrazine-containing compounds, Schiff bases, and amines,¹⁴⁻¹⁷ also contribute to a large percentage of the MOFs reported in the literature. The use of sulfonates,¹⁸⁻²⁰ phosphonates,²¹⁻²⁴ and their derivatives as ligands has received attention recently for the diversity of framework structures they form. A group of novel MOFs constructed from complex, highly strained molecules, called mechanically interlocked molecules, have also been reported.²⁵⁻²⁷ Highly stable MOFs based on azolates and mixed donor linkers displaying acid- and base-resistance have also been studied.²⁸ In this review, we summarize the utility of carboxylates, pyridyl and ether derivatives, Schiff bases, as well as mechanically interlocked molecules, as ligands in the assembly of various MOFs (refer to **Table 1**).

3.1 Carboxylate derivatives

The use of rigid *n*-carboxylates as ligands has been well documented in the literature, including di-, tri-, and tetra-carboxylates. A novel cluster-based 3D MOF constructed from the rigid carboxylate ligand 4-(4-carboxyphenyl)-1,2,4-triazole (HCPT) was reported by Zhao *et al.*²⁹ This MOF exhibits two main unique features - the presence

of Ho₈Na and Cu₈I core clusters in a heterometallic framework, as well as its previously unknown 6,12-connected topology. Chang *et al.*³⁰ employed a dicarboxylic acid derivative, 5-(4'-methylphenyl)isophthalic acid, and four N-donor ligands in constructing four low-dimensional Co(II)-based coordination polymers. Another dicarboxylic acid derivative, 3,5-pyridinedicarboxylate (pydc), has also been employed for the synthesis of 1D and 2D Co(II)-MOFs.³¹ The first MOF [Co(pydc)(H₂O)₂]_n consists of honeycomb-like voids, with each of the pydc ligand linked to three Co(II) ions, forming an infinite 2D layer. The second MOF [Co(pydc)(H₂O)₄]_n(H₂O)_n consists of pydc acting as the bidentate ligand, joining two Co(II) ions to give rise to a 1D zigzag chain, with guest water molecules occupying the voids between the polymeric chains. Both MOFs exhibit chemotropism following 2D-1D structural phase transformation upon water exposure, and exhibited reversible phase change between the dehydrated and hydrated forms. Dicarboxylate-MOFs based on lanthanides and actinides have also been studied, such as a series of multifunctional lanthanide-MOFs (Ln-MOFs) from 5-methyl-2-pyrazine carboxylic acid (Hmpca),³² and uranyl-MOFs derived from pyrazine-2,3-dicarboxylic acid (H₂PZDC)³³ and 1,4-naphthalene dicarboxylic acid (H₂NDC)³⁴. The reaction between Ln(NO₃)₃·6H₂O, Hmpca, and K₄[Mo(CN)₈]·H₂O at 1:2:1 molar ratio *via* slow diffusion method yielded photoluminescent Ln-MOFs with a general formula of [Ln(mpca)₂(CH₃OH)₂Ln(H₂O)₆Mo(CN)₈]_n·8H₂O (where Ln³⁺ = Nd³⁺, Eu³⁺, Gd³⁺, Tb³⁺ and Er³⁺).³² The presence of hard base carboxylates, as well as

cyanide as linkers, endowed these permanently porous MOF structures with good thermal stability overall, and efficient emission in the visible region for the Eu(III)- and Tb(III)-MOFs. Hydrothermal synthesis of uranyl-MOFs based on H₂PZDC and H₂NDC generated 1D to 3D MOFs with unique coordination spheres.^{33,34} Different formulae of uranyl-MOFs, such as [UO₂(PZDC)(H₂O)₂], [UO₂(PZDC)(H₂O)] and [(UO₂)₂Cs(PZDC)₂(OH)(H₂O)], were observed upon using NMe₄OH, pyridine, or CsOH as bases, whereas the MOF (H₃O)₂[(UO₂)₂(NDC)₃]·H₂O displayed polycatenation that emerged from the 2D honeycomb grid network established by the H₂NDC ligand. Three MOFs derived from a lactam-dicarboxylate ligand, whose network structures were individually linked by different Mⁿ⁺ ions (where M = Cu²⁺, La³⁺, Pr³⁺), have also been studied.³⁵ Waitschat *et al.*³⁶ utilized hydrothermal treatment for the synthesis of a novel Zr-MOF (CAU-22; where CAU = Christian-Albrechts-Universität) bearing 2,5-pyrazinedicarboxylic acid as the ligand. This hydrophilic MOF comprises hexanuclear clusters of {[Zr₆(μ₃-O)₄(μ₃-OH)₄]} *via* edge-sharing, and offers permanent porosity towards H₂O and N₂. Optimization studies were performed on this MOF using various Zr(IV) salts, as well as by varying the formic acid to H₂O ratio. The authors discovered that optimal conditions for the highest crystallinity MOFs were achieved only when ZrCl₄ and ZrOCl₂ were used in equimolar metal-to-ligand ratio, and at 70:30 and 50:50 formic acid : water ratio, respectively.

The tricarboxylic acid derivative, benzene-1,3,5-tricarboxylic acid (BTC), along with its geometrically similar triazine-cored pyridyl analogue, 2,4,6-tris(4-pyridyl)-1,3,5-triazine (TPT), were exploited in the assembly of Cu(II)- and Ni(II)-MOFs.^{37,38} The Ni(II)-MOF, {[Ni₃(OH)(BTC)₂(TPT)][NH(CH₃)₂]}_n, exists as a two-fold interpenetrated 3D MOF derived from a Ni₃(OH)(COO)₆ trinuclear unit. The combination of these two linkers gave rise to the formation of a new (3,8)-connected 3D net. Similarly, the Cu(II)-MOF with the structural formula [Cu₂(TPT)₂(BTC)Cl]·(solvent)_x, possesses BTC linkers linked to the Cu(II) ions to

form a 2D layered structure, which is further extended by TPT to generate a 3D network. Interestingly, the Cu(II)-MOF exhibits a magnetic long-range ordering at 5 K, demonstrating the strongly frustrated nature of this magnetic MOF.

Tetracarboxylic acid derivatives, such as benzene-1,2,4,5-tetracarboxylic acid (H₄btec), 3,6-dibromobenzene-1,2,4,5-tetracarboxylic acid (H₄dbtec), pyrazine-2,3,5,6-tetracarboxylic acid (H₄pztc), and 2,6-di(2',5'-dicarboxylphenyl)pyridine (H₄L), are known tetratopic linkers for designing MOFs.³⁹⁻⁴¹ Zhang *et al.*⁴¹ reported the synthesis of three isostructural alkali-lanthanide MOFs, with a formula of [K₃Ln₅(pztc)₅(H₂O)₁₉]·7H₂O (where Ln = Dy, Ho, and Yb), derived from H₄pztc. Each of these 3D open frameworks consists of metal ions bridged by the pztc⁴⁻ linkers in a ladder-like square column architecture, whose assembly leads to the formation of an uncommon (4,8)-connected net (refer to **Figure 7**). With the alkaline earth metals Ba(II) and Ca(II), the linkers H₄btec and H₄dbtec yielded pillar-layered 3D MOFs and 3D supramolecular frameworks.³⁹ While the 3D bimodal framework in [Ba₂(dbtec)(H₂O)₂]_n is stabilised by axial Br···π supramolecular interactions, the framework network in [Ca₂(dbtec)(H₂O)₈]_n is held by prominent intra- and intermolecular H-bonding interactions with water ligands. In {[Ba₂(H₂btec)·H₂O]·0.5H₂O}_n and [Ca(H₂btec)·H₂O]_n, a 3D 3-nodal network and a 2D-double layer were observed, respectively. Another interesting study by Siman *et al.*⁴² demonstrated the formation of two rare, porous Na(I)-MOFs based on two tetratopic carboxylate linkers, H₄BDA and H₄BPDA. These Na(I)-MOFs, namely [Na₄(BDA)(CH₃OH)(H₂O)] and [Na₄(BPDA)(H₂O)₂], consist of 2D sodium oxide sheets connected by their respective linkers. Both MOFs crystallize in the monoclinic P2₁ space group with the infinite 2D Na₂O sheets extending in the [010] and [100] directions.

Metal-biomolecule frameworks (MBioFs) have also been designed and synthesized owing to the biocompatibility of the biomolecules incorporated as the organic ligands, such as amino acids, proteins and nucleotides. Imaz *et al.*⁴³ describe the

three main types of amino acid (AA)-based MBioFs. These MBioFs are generally constructed from metal ions with (i) natural AAs; (ii) natural AAs, bridging anions and polydentate ligands; and (iii) chemically-altered natural AAs. Four AA-based MBioFs were synthesized, using the four AAs - aspartic acid (Asp), glutamic acid (Glu), methionine (Met) and histidine (His). These ligands were selected due to their high chelating ability and polydentate nature. Nucleotide- and saccharide-based MBioFs were also crystallographically studied for their potential roles in gas storage, catalysis and biomedicine. Over the past decade, the meticulous exploration of MOFs by the world's leading research groups has had a big impact on the exploitation of MOFs as functional materials. For example, Yaghi and co-workers have been developing complex MOF

systems of unprecedented properties and topologies, by utilizing their profound knowledge of the concept of secondary building units.⁴⁴ One such achievement is in the successful construction of a hierarchical MOF system, known as MOF-500, *via* a one-pot synthetic strategy, comprising a mixed-ligand system - 4,4'-biphenyldicarboxylic acid and 1,2-bis-4-pyridylethane.⁴⁵ An interesting feature of this MOF is its synthetic accessibility using the one-pot approach, which would otherwise be unachievable by stepwise reaction, due to hindrance by the formation of an insoluble intermediate IRMOP-51. In addition, the MOF-500 exhibited a fourfold enhancement of argon sorption capacity, having a specific area of 2274 m² g⁻¹, compared to 544 m² g⁻¹ for its IRMOP-51 precursor.

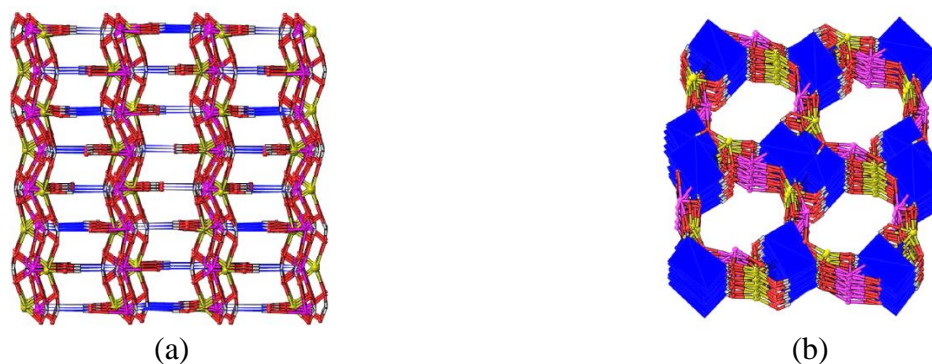


Figure 7. Crystal structure of $[K_5Dy_5(pztc)_5(H_2O)_{19}] \cdot 7H_2O$ as a 3D framework, as viewed (a) along the *c* axis, and (b) along the *b* axis (of the 1D channels).

The pyrazine rings are depicted as planes, and H₂O molecules are excluded for clarity. Reproduced with permission from Zhang *et al.*⁴¹ Copyright 2014 American Chemical Society.

Multivariate (MTV) MOFs, whose structures comprise a number of different organic ligands, were first introduced into the literature by functionalizing MOF-5, and studies on these materials have recently been extended to incorporate mixed metals (*e.g.* MOF-74). MOF-74 is a suitable candidate for expanding the scope of MTV MOFs owing to its infinite rod components linked by 2,5-dioxidoterephthalate ions (**Figure 7**).⁴⁶ Five phase-pure mixed-metal MOFs (each containing 2, 4, 6, 8 and 10 metals per structure) have been successfully synthesized *via* a one-pot solvothermal synthesis.⁴⁷ These MOFs, each abbreviated as MnM-MOF-74 (where *n* = 2, 4, 6, 8 or 10), contain a mixture of

Group II M²⁺ (M = Mg, Ca, Sr, Ba) and divalent transition metal (Mn, Fe, Co, Ni, Zn, Cd) ions. Based on energy-dispersive X-ray spectroscopy and scanning electron microscopy analyses, the crystalline particles of the MOFs were observed to have all metals distributed within their surfaces, with each crystal comprised of a non-linear distribution of the different metals. In one study,⁴⁸ the framework structure of a mechanically unstable Al-based MOF-520, prepared with 1,3,5-benzenetricarboxylate as ligands, was modified with 4,4'-biphenyldicarboxylate (see **Figure 8**), resulting in an exceptional enhancement to its mechanical adaptability, achieved through a process called *retrofitting*. Here, the 4,4'-

biphenyldicarboxylate linkers behave as “girders”, providing a form of mechanical support by linking together two adjacent octametall

SBUs in the MOF. As a result, ultrahigh deformation of the MOF does not occur until the pressure reaches 5.5 GPa.

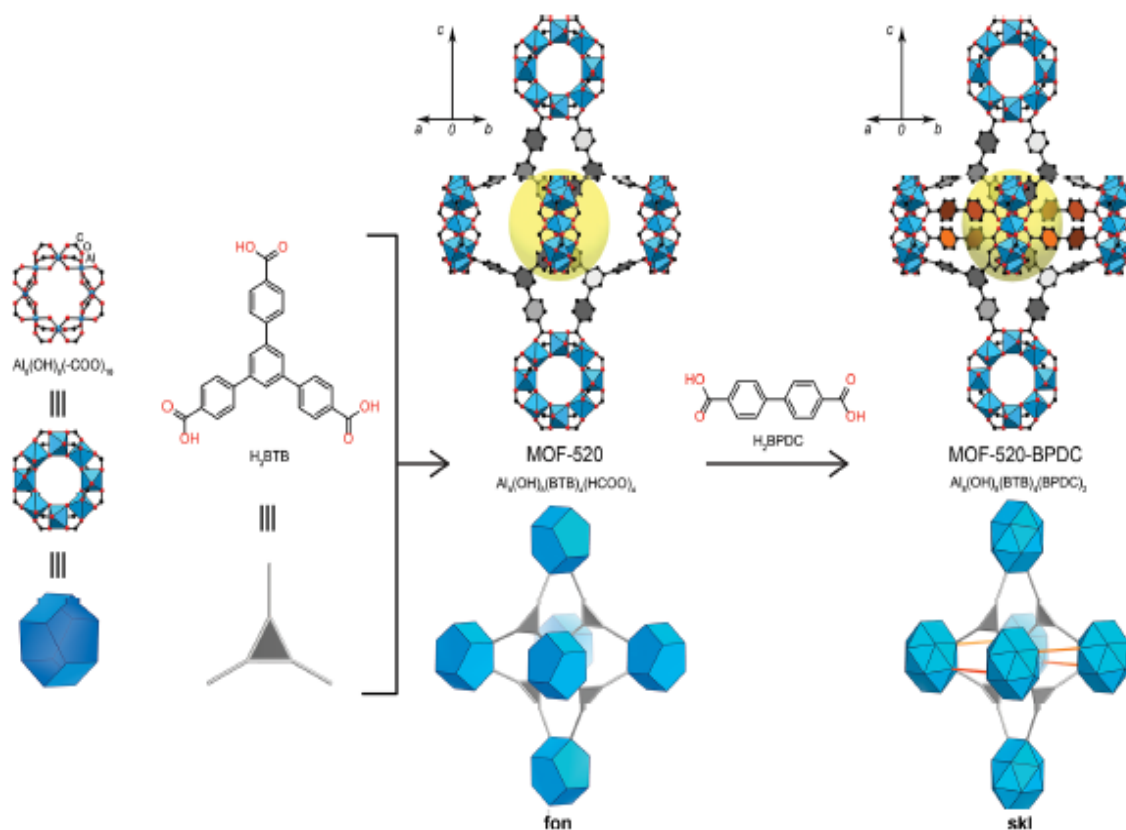


Figure 8. Retrofitting in promoting mechanical stabilisation to MOF-520 via linking two neighbouring SBUs by the 4,4'-biphenyldicarboxylate ligand. The precursor MOF-520 is represented by the dark blue octahedron. Reproduced with permission from Kapustin *et al.*⁴⁸ Copyright 2017 American Chemical Society.

3.2 Pyridyl and ether derivatives

MOFs may be constructed by first preparing discrete units of metalloligands from one metal species at a certain proportion, followed by the addition of ions of the second metal to the solution of former metalloligands. Such an approach was employed previously in the preparation of five mixed-metal organic frameworks (MMOFs) based on two dipyriddy β -diketonates. In their work, Burrows *et al.*⁴⁹ used two analogous ligands, 1,3-di(4-pyridyl)propane-1,3-dione (Hdppd) and 1,3-di(3-pyridyl)propane-1,3-dione (Hdmpdd) to prepare the MMOFs and discovered that the crystal structures of the coordination polymers generated in this way are dictated by the nature of the counteranions used. Two analogous macrocycles prepared from biphenyl - 2,2'-bis(3-pyridylmethylenoxy)-1,1'-biphenylene (3,3'-

bpp) and 2,2'-bis(4-pyridylmethylenoxy)-1,1'-biphenylene (4,4'-bpp) - have been utilized to make MOFs with unusual structural motifs by virtue of the distorted biphenyl spacer.⁵⁰

MOFs with interestingly divergent structural topologies have been constructed from these two macrocyclic ligands with various Zn^{II} , Co^{II} , and Cd^{II} salts as revealed by analyses of their single crystals (**Figure 9**). Although $[\text{Zn}_2(3,3'\text{-bpp})_2\text{Cl}_4]$ and $[\text{Zn}_2(3,3'\text{-bpp})_2\text{Br}_4]$ exist as dinuclear metallomacrocycles stabilised by π - π stacking, and $[\text{Zn}(4,4'\text{-bpp})\text{Cl}_2]_n$ and $[\text{Zn}(4,4'\text{-bpp})\text{Br}_2]_n$ as 3D structures emerged from the cooperative effects of the 1D polymeric chains, $[\text{Co}(4,4'\text{-bpp})_2(\text{SCN})_2]_n$, $[\{\text{Cd}(4,4'\text{-bpp})_2(\text{SCN})_2\} \cdot 2\text{H}_2\text{O}]_n$ and $[\text{Cd}(4,4'\text{-bpp})(\text{dca})_2]_n$ (dca = dicyanamide) on the other hand adopt complex topologies. In the

solid state, $[\text{Co}(4,4'\text{-bpp})_2(\text{SCN})_2]_n$ and $[\{\text{Cd}(4,4'\text{-bpp})_2(\text{SCN})_2\} \cdot 2\text{H}_2\text{O}]_n$ both form 2D polymers, except that $[\text{Co}(4,4'\text{-bpp})_2(\text{SCN})_2]_n$ folds into zigzag chains and rectangular boxes, whereas $[\{\text{Cd}(4,4'\text{-bpp})_2(\text{SCN})_2\} \cdot 2\text{H}_2\text{O}]_n$ consists of interpenetrated layers assembled from alternating left-hand and right-hand cylindrical 2_1 helices. A similar feature was also noted for

$[\text{Cd}(4,4'\text{-bpp})(\text{dca})_2]_n$ as in $[\{\text{Cd}(4,4'\text{-bpp})_2(\text{SCN})_2\} \cdot 2\text{H}_2\text{O}]_n$, but with a formation of 2D Cd^{II} layers made with the coordinating dicyanamide anions. Another Cd^{II} -dipyridyl-MOF displaying reversible adsorption of monohalobenzenes at room temperature has also been reported.⁵¹

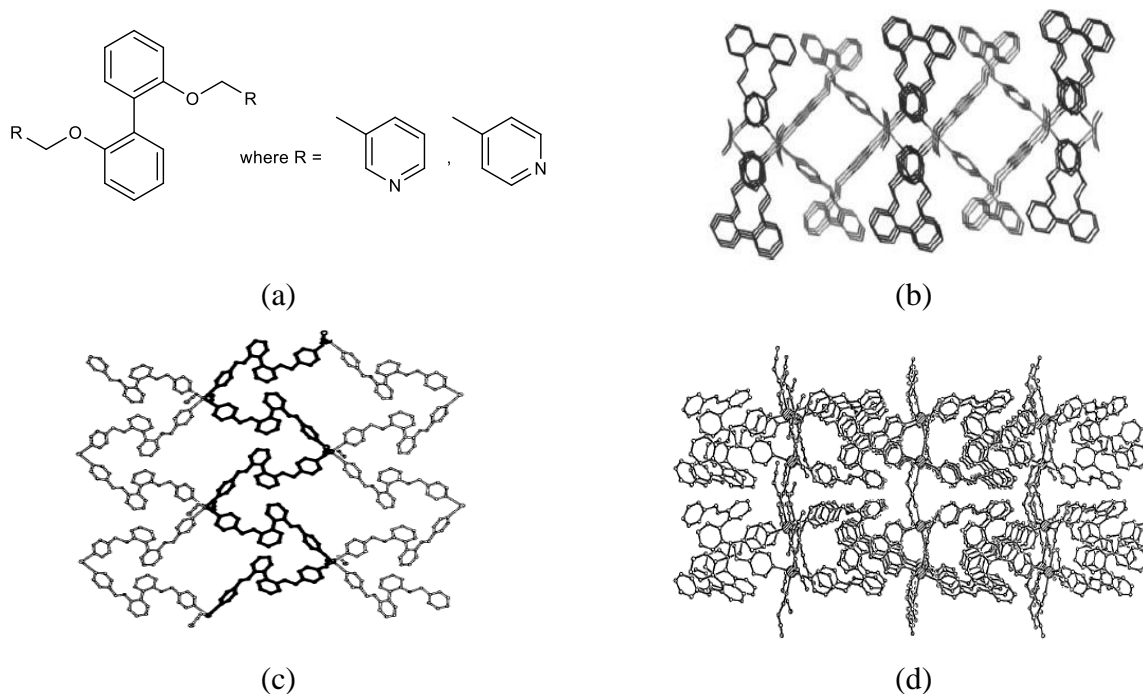


Figure 9. Molecular structure of dipyridyl-based macrocycles used in MOF synthesis as depicted by (a) the crystal structures revealing the packing in (b) $[\text{Co}(4,4'\text{-bpp})_2(\text{SCN})_2]_n$ (along the b axis), (c) $[\{\text{Cd}(4,4'\text{-bpp})_2(\text{SCN})_2\} \cdot 2\text{H}_2\text{O}]_n$ excluding uncoordinated water molecules (along the c axis), and (d) $[\text{Cd}(4,4'\text{-bpp})(\text{dca})_2]_n$ (along the a axis).

Reproduced with permission from Wang *et al.*⁵⁰ Copyright 2004 Wiley-VCH.

The flexible nature of the dipyridyl ligands implies that conformational diversity is anticipated to occur in the MOFs, and as such, can lead to the formation of active sites that are useful as catalytic centres. Liu *et al.*^{52,53} exploited a series of short, isomeric bis(pyridine- n -ylmethoxy)benzene ligands to construct structurally diverse $\text{Cd}(\text{II})$ -MOFs *via* hydrothermal synthesis. By varying the positions of the oxygen atoms on the substituted phenolic rings and those of nitrogen atoms relative to the alkyl chains (either *ortho*-, *meta*-, or *para*-substituted), the topological architecture of the MOFs produced can be diversified. Furthermore, the versatile coordination nature of the Cd^{II} ions can result in different geometries about the metal

centres, as observed in the five MOFs. Three distinct coordination geometries (pyramidal, distorted octahedral, and bipyramidal) were made accessible simply by altering the positions of the donor nitrogen atoms, despite these ligands being positional isomers. Interestingly, these MOFs were discovered to serve as convenient, room temperature photocatalysts for degrading methylene blue, a typical organic dye used in the manufacture of textiles, when irradiated by UV light. Among the five studied MOFs, $[\text{Cd}(1,4\text{-BDC})(\text{bpmp})(\text{H}_2\text{O})_n]$ (1,4-BDC = 1,4-benzenedicarboxylate; bpmp = 1,3-bis(pyridine-3-ylmethoxy)benzene) exhibited the best photocatalytic performance, with a 98.0% degradation ratio of the methylene blue after 120

min. In another study by Wang *et al.*⁵⁴, an ether derivative of benzoic acid, 4,4'-oxybis(benzoic acid) (H₂oba), was exploited in the hydrothermal synthesis of two sodium-lanthanide MOFs based on Eu(III) and Sm(III). The isolated MOFs were isostructural and isomorphous in nature, with a general formula of [NaLn(oba)(ox)(H₂O)] (where Ln³⁺ = Eu³⁺ and Sm³⁺; ox = oxalate). These 3D MOFs consist of distorted tricapped trigonal LnO₉ units, as well as distorted octahedron NaO₆ units, along with the oba and ox ligands. Furthermore, coordination was established by oba and ox ligands to the Ln and Na ions, which generated a 3D network from the 2D inorganic sheets.

Enantiomeric Zn-based MOFs [(*SS*)- and (*RR*)-MOF-1020] having precisely ordered chiral recognition sites have been synthesized *via* the solvothermal method in DMF.⁵⁵ These highly designed MOFs each possess an axially chiral bisbinaphthyl[22]crown-6 moiety as a part of a dicarboxylic acid-terminated ligand (abbreviated as *SS*-2 and *RR*-2). The enantiomeric ligands were prepared by a series of steps, with a terminal reaction involving the palladium(II)-catalysed Suzuki coupling reaction, followed by subsequent hydrolysis of the ester functionality to generate the desired dicarboxylic acid-based ligands. The voids that span the crown ether moiety result in chiral active domains that offer stereoselective recognition of chiral molecules. This feature would permit further development of an array of highly engineered optically active stationary phases to be used in high-performance liquid chromatography, in particular.

A series of pyridyl/triazolyl-MOFs based on Co(II), Cu(II) and Cd(II) ions, and N-heterocyclic auxiliary ligands have been reported by Chen *et al.*⁵⁶ In this work, the authors incorporated camphoric acid to induce racemisation in three of the assembled MOFs under solvothermal conditions. The prepared MOFs adopted a variety of polymeric structures, ranging from a 1D ladder and helical chain, to 3D networks. Among these structures, the three Cd(II)-MOFs, [Cd(SO₄)(4-abpt)(H₂O)]_n·3nH₂O, [Cd(D-cam)(2-PyBIm)(H₂O)]_n, and [Cd(D-cam)(btmb)]_n (where

4-abpt = 4-amino-3,5-bis(4-pyridyl)-1,2,4-triazole; D-H₂cam = D-camphoric acid; 2-PyBIm = 2-(2-pyridyl)benzimidazole; btmb = 1,4-bis(1,2,4-triazol-1-ylmethyl)benzene), exhibited luminescence in the violet region of the visible spectrum, and were second-harmonic generation active, with positive or negative Cotton effects. Their emission spectra displayed similar luminescent behaviour, implying that such an emission originated from ligand-centred emission. In another study,⁵⁷ the ligand 1,2,4,5-tetra(4-pyridyl)benzene (TPB) was exploited for the assembly of a 3D cationic Ag(I)-MOF with the formula of {[AgTPB]·SbF₆}_n. This MOF consists of SbF₆⁻ anions incorporated within its pores, which, upon activation, selectively adsorbs CO₂ and H₂O over CH₄ and EtOH, respectively. A rapid exchange of the dichromate Cr₂O₇²⁻ anion in aqueous media is readily observed at room temperature. The use of MOFs with reactive metal sites bearing Pd-diphosphine pincer complexes has been studied, in the course of which a Zr-MOF was subject to surface modification.⁵⁸ The conversion involved the transformation of the PdI sites, coordinated to a diaminopyridine ligand, into PdBF₄ *via* oxidative I/BF₄⁻ ligand exchange. The modified MOF displayed enhanced selective catalysis towards intramolecular hydroamination involving 2-ethynylaniline over a self-dimerisation process, as well as towards carbonylene cyclisation of citronellal.

3.3 Schiff bases

Schiff bases are a class of organic compounds that possess the RR¹C=NR² moiety, while those bearing R = H, are specifically known as azomethines (HC=N). They are prepared from the condensation reaction between a carbonyl compound and a primary amine, *via* an S_N2 reaction which proceeds through an iminium intermediate.⁵⁹ Generally, aldehydes react relatively faster with the primary amines, compared to their analogous ketones. Diverse types of Schiff bases have been synthesized, ranging from alkyl to aryl side groups, and from acyclic to cyclic molecules. Schiff bases harbouring aryl functional groups tend to be more kinetically stable than alkyl ones owing to the conjugation of the aromatic ring.⁶⁰ Over the years,

a number of synthetic approaches have been employed for the synthesis of Schiff bases, such as the conventional,⁶¹ mechanochemical⁶² and green⁶³ methods. Conventional synthesis is a common method utilized for Schiff base synthesis. It employs an inert organic solvent, such as methanol, as the reaction medium. The reaction can be performed either at room temperature, or with refluxing at elevated temperatures. The alternative green approach to synthesis has received considerable attention in the field of synthetic chemistry due to its minimal wastage of solvent and also the exclusion of hazardous solvents during the reaction. Schiff bases cover a diverse range of applications in multidisciplinary fields - in medicine as prodrugs⁶⁴ and bioactive compounds,^{65,66} in inorganic chemistry as heterogeneous catalysts⁶⁷, as sensors for heavy metal ions in aqueous media,⁶⁸ as water chain stabilisers in a metal host,⁶⁹ as liquid crystals⁷⁰ and in designing thermo-/photochromic materials.^{71,72}

Alkyl (e.g. dichloromethane and chloroform) and aryl halides (e.g. bromobenzene) are two classes of closely related halogenated organic compounds that are known to pose detrimental effects (e.g. respiratory irritation, liver necrosis) to both

humans and the environment, in general. Thus, synthetic materials that can 'trap' these irritant gases are highly sought after, and in recent years, this function has been accomplished by certain porous MOFs. Wang *et al.*⁷³ have reported the first ternary heterometallic organic framework (HMOF) constructed from three metal centres - Fe(III), Ba(II) and Na(I) - and the Schiff base 1,2-cyclohexanediamino-*N,N'*-bis(3-methyl-5-carboxysalicylidene) (see **Figure 10**). This unique HMOF exhibits photocatalytic activity towards the three isomers of chlorophenols (*n*-chlorophenols, *n* = 2, 3 or 4) in the visible region. In another report, a Cd^{II}-MOF based on a novel dipyridyl Schiff base (see **Figure 11**) was synthesized by Xiao *et al.*⁷⁴, revealing selective adsorption of dichloromethane over chloroform under mild conditions (see **Figure 12**). Structurally, this particular MOF comprises two μ -SCN⁻ anions bridging the Cd^{II} centres to generate a rhombus-channeled 3D framework. Each of the Cd^{II} metal nodes possesses a distorted octahedral coordination sphere, in which two N atoms from the ligand, as well as two S and two N atoms from the thiocyanate anions, are coordinated to it. The thiocyanate anions act as the bridging ligands, linking adjacent Cd^{II} metal ions to form a metal-thiocyanate inorganic polymer chain.

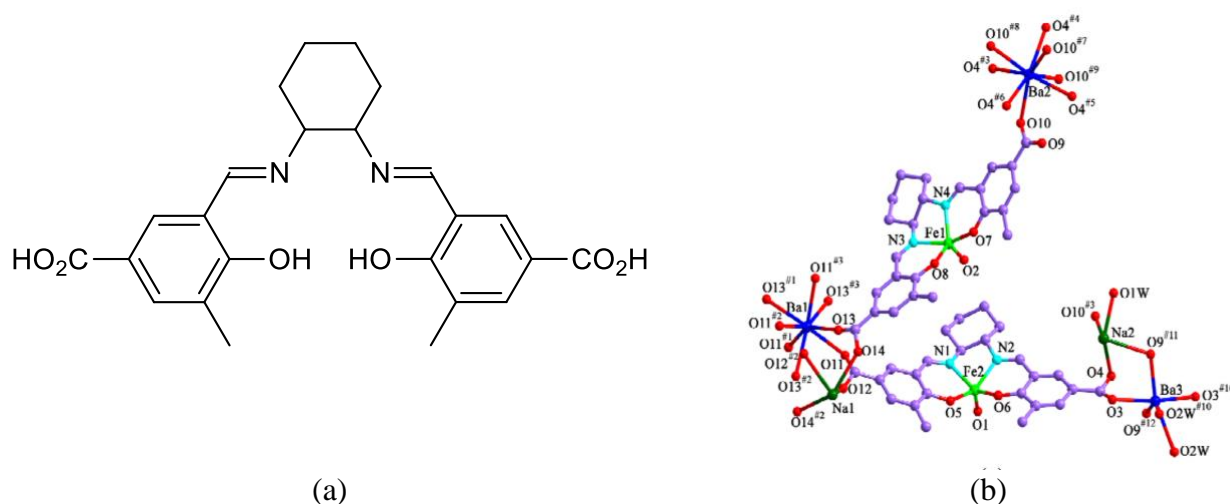


Figure 10. (a) Molecular structure of 1,2-cyclohexanediamino-*N,N'*-bis(3-methyl-5-carboxysalicylidene).

(b) Crystal structure showing the coordination environment of the HMOF.

Reproduced with permission from Wang *et al.*⁷³ Copyright 2015 American Chemical Society.

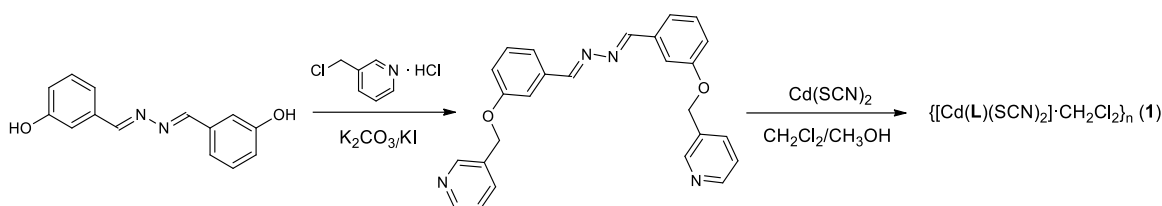


Figure 11. Synthesis of 3-(aryl ether)pyridyl azine derivative and its Cd^{II}-MOF.⁷⁴

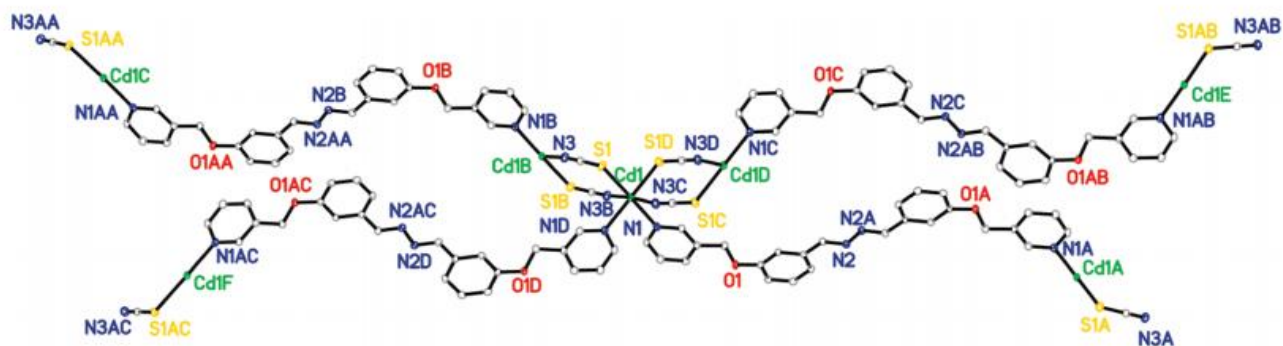


Figure 12. ORTEP representation of the coordination environment of the Cd^{II}-MOF, showing its polymeric chain structure. Reproduced with permission from Xiao *et al.*⁷⁴ Copyright 2011 American Chemical Society.

A highly thermally stable, porous Ag(I)-based MOF, reported by Cheng *et al.*,⁷⁵ and derived from the Schiff base 3,6-bis[2-(4-oxide-quinoxaline-yl)-4,5-diaza-3,5-octadiene], has been shown to effectively isolate benzene from its six-membered organic analogues. Zhang *et al.*⁷⁶ reported the solvothermal synthesis of four 2D network coordination polymers based on Zn(II) and Cd(II). These polymers were found to exhibit greatly enhanced electrochemical luminescence (ECL) with ECL yields of 0.56-0.72. According to the authors, this intensified ECL emission is attributed to the enhanced spin-orbit coupling effect exerted by the incorporation of Zn ions. In another study,⁷⁷ the authors demonstrated the self-assembly of two Co(II)-MOFs, [Co₆(SO₄)₂(BTEC)(OH)₄·3H₂O]_n (1) and [Co₂(BTEC)(4-bpdb)(H₂O)₂·4H₂O]_n (2), under hydrothermal conditions by incorporating a mixture of 1,2,4,5-benzenetetracarboxylic acid (H₄BTEC) and 4,4'-dipyridylamine (dpa) or 1,4-bis(4-pyridyl-2,3-diaza-1,3-butadiene(4-bpdb)). In MOF 1, coordination was achieved by SO₄²⁻ instead of the dpa ligand, owing to steric hindrance imposed by BTEC⁴⁻, which prevents the participation of the shorter length of dpa in the coordination. Another Co(II)-MOF derived from the Schiff base 4,4'-[benzene-1,4-

diylbis(methylylidenenitrilo)]dibenzoic acid (H₂bdda), having an empirical formula of Co₂(bdda)_{1.5}(OAc)·5H₂O (abbreviated as UoB-3), was synthesized ultrasonically at room temperature.⁷⁸ Based on catalytic studies, the authors discovered that UoB-3 showed a good performance as a heterogeneous catalyst for the oxidation of various primary and secondary alcohols (75-95% yields, 65°C, ≤75 min), as well as the Henry reaction (62-88%, 70°C, 24 h). Two asymmetric vanillin-derived Schiff base ligands, namely 4-hydroxy-3-methoxybenzaldehyde nicotinoylhydrazone (L₁) and 4-hydroxy-3-methoxybenzaldehyde salicyloylhydrazone (L₂), were employed for the assembly of five coordination polymers based on Pb^{II}, Cu^{II} and Co^{II}.⁷⁹ A notable feature was observed in the reaction between Pb^{II} salts and L₁ after changing the anion present in the Pb^{II} salt used, namely that the presence of acetate ions in the reaction mixture promotes the formation of a 1D structure with formula Pb₂(L₁)₂(OAc)₂(H₂O)₂, whereas a 3D diamondoid structure [Pb₂(L₁)₂(NO₃)₂]·3H₂O is obtained when a nitrate ion is present (refer to **Figure 13**). Similarly, while the reaction between Co(NO₃)₂ and L₂ in MeOH/CH₂Cl₂ and pyridine favours the formation of a discrete complex with

the formula $[\text{Co}^{2+}(\text{L}_2)_2(\text{py})_2] \cdot 2\text{CH}_3\text{OH} \cdot \text{H}_2\text{O}$, using $\text{Co}(\text{ClO}_4)_2$ instead gives rise to a 1D extended complex structure, namely $[\text{Co}^{3+}(\text{L}_2)_2(\text{py})_2] \cdot \text{ClO}_4$.

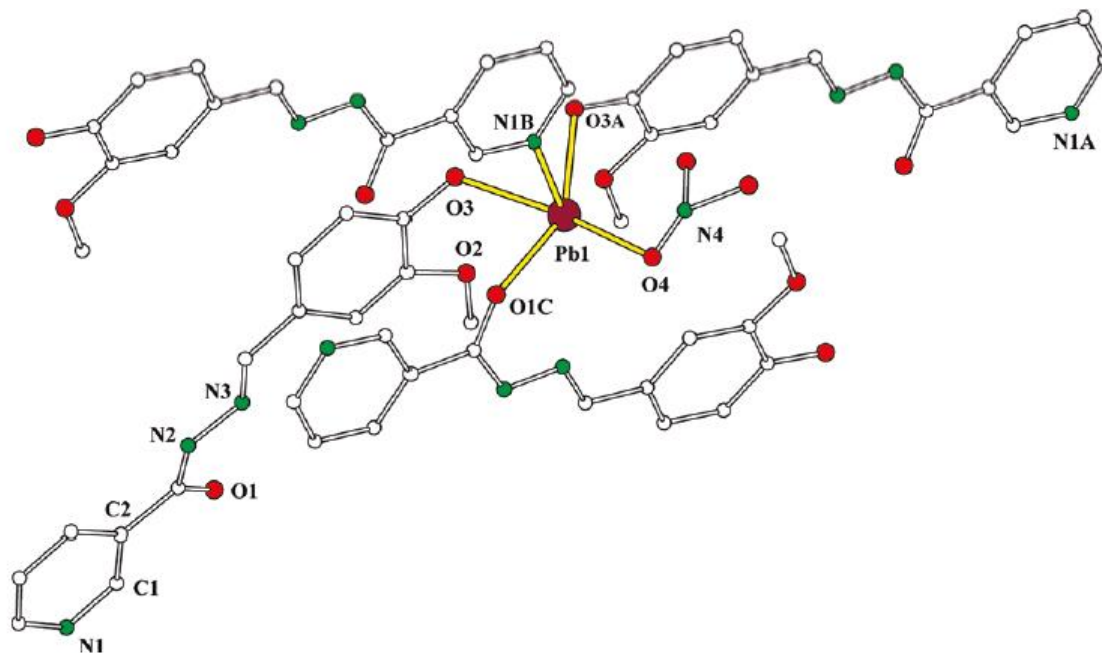


Figure 13. The crystal structure of the polymeric $[\text{Pb}_2(\text{L}_1)_2(\text{NO}_3)_2] \cdot 3\text{H}_2\text{O}$, illustrating the coordination environment around the Pb^{II} ion.

Reproduced with permission from Li *et al.*⁷⁹ Copyright 2010 American Chemical Society.

3.4 Mechanically interlocked molecules

Mechanically interlocked molecules (MIMs) are topologically linked molecules that are not connected by conventional bonds. They consist of two or more organic molecules that are assembled in a stable, ring-like manner, which display interlocked components arranged perpendicular to each other. [2]Rotaxanes, cucurbit[6]uril, dibenzo[24]crown-8 ether wheels, and [2]catenanes are several examples of these intricate MIMs that have been incorporated as MOF linkers.⁸⁰ They are of paramount importance for developing molecular shuttles and switches for functional ultrahigh-density electronics. Interestingly, MIMs in several reported MOFs are the most complicated ligands ever employed in MOF synthesis. In two related reports,^{81,82} two analogous catenane units of MIMs derived from cyclophanes and polyether rings were incorporated into MOFs to give two previously unknown MOFs, namely MOF-1011 and MOF-1030. The shorter and longer MIM ligands recorded remarkable lengths of 19.3 and 32.9 Å, respectively, with the 'linear' part of the ligand

benz as a result of the strain imposed by the vast conjugated π -system. Covalently attaching the MIMs as MOFs enhances the performance of the MIMs by strongly restricting the translational motion of the molecules, since their performance is optimal when highly ordered and coherent. MOF-1011 assembles as a 2D MOF, whose framework consists of trigonal Cu(I) units and ligand backbones, generating high density layered structures. This accomplishment is another stepping stone in MOF chemistry, since the field of catenane-MOFs is relatively new, and single crystals of catenane-MOFs have not been well studied, as a consequence of the bulkiness and lack of symmetry, coupled with the rigid yet dynamic behaviour of the catenanes.

A Zn-MOF based on a hexacarboxylate-[2]rotaxane MIM linker, with the formula $\{[\text{NH}_2\text{Me}_2]_2[\text{Zn}_2(\text{H}_2\text{O})_2(\text{L})](\text{H}_2\text{O})_{1.25}\}$ (L = MIM linker), has been reported by Gholami *et al.*²⁵ The repeating unit of the resulting MOF is made of all six of the carboxylate groups on L coordinated to a Zn ion of a secondary building unit. The six

negative charges on the anionic framework are counterbalanced by two dimethylammonium ions, generated from the thermal decomposition of the DMF solvent during the solvothermal treatment. Each of the two independent Zn centres adopts tetrahedral geometry with the three different carboxylate ends of the linker coordinated to it. Variable-temperature powder X-ray diffraction in a temperature range 25-200 °C revealed that the crystalline structure had been preserved, indicating the robustness of the material owing to the highly restricted motion of the framework. MIMs bearing amide²⁶ and amine²⁷ moieties have also been explored, and utilized in the synthesis of an Ag(I)-isophthalamide [2]catenane, and a Cu(II)-[2]rotaxane MOF, respectively. The Cu(II)-[2]rotaxane MOF has a formula of $[\text{Cu}_2(\text{MIM})(\text{H}_2\text{O})_2] \cdot 3\text{H}_2\text{O}$, adopting an unusual β -phase of NbO topology with lattice water occupancy of 11% in the pores. Interestingly, upon the activation of the Cu(II)-MOF by the removal of the water, the structural integrity of the framework was retained and remained unaffected after a further activation-deactivation process. On the other hand, the Ag(I)-isophthalamide [2]catenane was found to exist as a 1D coordination polymer, with the formula $\{[\text{Ag}(\text{MIM})](\text{OTf})\}$, and the asymmetric unit consists of one catenane molecule, one Ag(I) ion and OTf^- anion, as well as disordered solvent molecules. The pyridine units of the macrocycles from neighbouring catenanes coordinate to the Ag(I) ions, adopting a distorted linear geometry. Further, the 2D lattice formed is stabilised by the π -stacking between the chain dimers.

Several transition metal- and lanthanide-based MOFs bearing MIMs have been studied, including the Texas-sized molecular box (TSMB) MIMs. These TSMB MIMs are essentially [2]pseudorotaxanes linkers designed from tetraimidazolium macrocycle and typical dicarboxylates.⁸⁰ One TSMB, derived from 2,6-naphthalene-dicarboxylate (L^{2-}) formed an Ag(I) MOF with formula $[\text{Ag}_2(\text{L} \subset \text{TSMB})(\text{L})][\text{L}]$ giving rise to a framework structure comprising each Ag(I) centre coordinated to two carboxylate groups in a *trans* geometry, with Ag-Ag distances

of 13.5 and 13.8 Å, as well as the incorporation of non-coordinated charged L and water molecules within the pores. However, for its Zn(II) analogue $[\text{Zn}_2(\text{L} \subset \text{TSMB})(\text{L})_3] \cdot (\text{H}_2\text{O})_6$, the tetrahedral Zn(II) centres are ligated by four carboxylate moieties, forming an interpenetrated diamondoid topology, with the pores occupied by interpenetration from the adjacent framework and water molecules. A 1,4-benzene-dicarboxylate derived TSMB (L^{2-}) was also employed as a ligand for constructing Ln(III)-based MOFs (Ln = Nd, Eu, Sm, and Tb). With Nd(III), a MOF with the formula $[\text{Nd}_2(\text{L} \subset \text{TSMB})_{4.5}(\text{H}_2\text{O})_4(\text{L}2)_{0.5}]$ was obtained, which exists as a poly-cationic three-periodic framework. Meanwhile, neutral three-periodic frameworks with the formula $[\text{M}_2(\text{L} \subset \text{TSMB})(\text{H}_2\text{O})_2(\text{L}2)_4]$ were obtained when M = Eu, Sm, and Tb. In the latter, the axle dicarboxylate linkers of the MIM molecules join the polymer into a 3D structure.

4. Applications of MOFs

MOFs have been studied for their potential applications in a variety of fields, such as catalysis, photoluminescent devices, gas storage and separation, and as antibacterial agents. N-rich ligands (triazines, tetrazoles, and hydrazines) have potential applications as high-energy MOFs.⁸³ Additionally, MOFs bearing superacidic sites useful for Brønsted acid catalysis for various organic transformations also open up a number of new possibilities in catalytic chemistry.⁸⁴ **Table 2** summarizes several applications in which MOFs have been extensively studied.

4.1 MOFs as heterogeneous catalysts

Post-synthetic modifications (PSMs) involve chemically modifying the organic functional groups that form the exterior regions of pores of the MOF surface. These chemically altered sites now exhibit an increase in reactivity that permits the activated surfaces to participate in various chemical or physical processes, such as organic catalysis, electrocatalysis and proton conduction. The activated surfaces provide an enhanced specific surface area for selective catalytic reactions, which are highly dependent on the pore size, as well as the geometry and dimensions of

the potential substrate molecules. MOFs with free amine groups can be easily converted into an azomethine group so that new functionalities can be introduced into the previously short surface ligands for complexation with metals for the desired catalysis.

In one study, an isorecticular MOF (IRMOF-3) was post-synthetically modified to incorporate Au(III) to generate a new Au(III)-based IRMOF, designated as IRMOF-3-SI-Au. The modified version had the highest turnover frequency of 52 h, followed by its Au-Schiff base complex analog, Au/ZrO₂ and AuCl₃, being 40, 12, and 3 h⁻¹, respectively. The unreacted amine group in the IRMOF-3 was initially reacted with salicylaldehyde to form its imine analog, and then followed by complexation with the tetrachloridoaurate(III) ion.⁸⁵ PSM has enabled the design of an efficient catalytic system with the catalytically active molybdenyl acetylacetonate site supported on a UiO-66-NH₂ MOF, effective for the epoxidation of both cyclic and aliphatic alkenes.⁸⁶ In this study, the Schiff bases salicylaldehyde (SA) and thiophene-2-carbaldehyde (TC) were reacted with the free aminated MOF surface, to give SA-Mo and TC-Mo analogs of the same MOF. Meanwhile, hydrogen peroxide, sodium iodate(VII) and *tert*-butyl hydroperoxide (TBHP) were preferentially selected as the oxidants, with TBHP giving the highest epoxide yield of 94% and 97% at the refluxing temperature of 1,2-dichloroethane for the SA-Mo and TC-Mo versions, respectively. In a recent study,⁸⁷ a Pd(II)-pyridylsalicylimine complex was successfully anchored hydrothermally onto the voids of a MOF, Cu(BDC), resulting in efficient, better recyclability, and a more selective catalyst for the Mizoroki-Heck coupling reaction.

4.2 MOFs as photoactive devices

Similar to discrete metal complexes, hybrid compounds such as MOFs have been studied for their potential utility as sensing devices due to their photoluminescent properties. Matthes *et al.*⁸⁸ have utilized the solvent-free synthetic strategy to construct intralanthanide MOFs, comprising Eu³⁺, Tb³⁺, and Gd³⁺ at various ratios with 4,4-

bipyridine as the linkers, for the purpose of tuning the emission colour of the resultant MOFs. Since Eu³⁺, Tb³⁺ and Gd³⁺ have statistically identical ionic radii (115, 112, 114 pm, respectively, when the coordination number = 7) as well as close proximity in both chemical characteristics and oxidation states, such a mixed crystal can be experimentally accomplished. Emission colours of red, orange, yellow and green were generated simply by varying the relative ratios of the lanthanides. Pure Eu³⁺ and Tb³⁺ ions have characteristic emissions in the red ($\lambda = 702$ nm) and green ($\lambda = 488, 546$ nm) regions, respectively. By mixing the two ions in selected proportions, different emission colours and intensities can be produced. Interestingly, the incorporation of Gd³⁺ into the framework only effectively mitigated the number of luminescence centres by quenching, and did not directly participate in the tuning process. In addition, the N₂ sorption behaviour of these lanthanide MOFs was investigated, and it was discovered that they possess microporosity as well as mesoporosity in the range 0.6-1.8 nm, with a maximum adsorptivity of 172 cm³ g⁻¹ at 315 °C, and a BET surface area of 660 m² g⁻¹.

Among the critical factors for the successful construction of MOFs (such as the method of synthesis, nature of the solvent used, reaction time and temperature, nature of anions present, pH and concentration of the starting materials, coordination numbers of the metal ions, as well as the flexibility or rigidity of the organic ligands used), the metal to ligand (M:L) molar ratio has been widely investigated, as it has been demonstrated that beyond a particular ratio the framework disintegrates and forms individual metal complexes instead.⁸⁹ A novel, rigid, dumbbell-shaped ditopic (two binding pockets) pybox ligand with six potential coordinating atoms formed a highly emissive coordination polymer with Eu(III) ions as the metal nodes. Absorbance measurements under Job plot conditions revealed that the optimum M:L ratio for MOF formation was 1.5:1, which was also correctly predicted based on the fact that Eu(III) possesses a maximum coordination number of 9, and the pybox ligand is 6-coordinating in nature, and thus $9/6 = 1.5/1$. Importantly, this Eu(III)-

based coordination polymer's dynamic behaviour in solution against other lanthanides (Tb(III) and Sm(III)) has been investigated, in addition to spectroscopic analyses that revealed the observed intense red emission, with remarkable quantum yields reaching up to 73%. These two properties of the coordination polymer would enable its equipment in photomaterials, and also in polymetallic emitting materials.

Beziau *et al.*⁹⁰ utilized α,β -unsubstituted dipyrin ligands (dpm) for the construction of a series of Cd(II) complexes with a general formula of [Cd(dpm)₂]. Among these complexes, complex 5 exists as a discrete structure in a tetrahedral environment, while complexes 7·MeOH, 7, and 8 form 1D, 2D and 3D coordination polymers, -9 were obtained as the cis-9 and trans-9, each consisting of Cd(II) centres chelated by two dpm ligands and two monodentate pyridine ligands, existing in the octahedral coordination geometry. Although solid-state luminescence studies revealed the quantum yield to be less than 1%, these Cd(II) complexes were the first series of crystalline coordination polymers bearing mono-dpm as ligands reported to possess luminescence behaviour.

4.3 Liquid and gas storage and separation

MOFs have been thoroughly explored for their practical utility in adsorption of industrially relevant liquids and gases, particularly H₂, which has been a challenge due to its lower density than air, and its inherently explosive nature. In addition, MOFs offer liquid and gas separation as well as storage that can be achieved by engineering the van der Waals radius or diameter of the open cavities. Pores, voids, or cavities play a pivotal role enabling entrapment of molecules of specific dimensions (termed guest molecules), and may possess catalytic sites. These guest molecules can be exposed to the unsaturated metal centres for reactions such as oxidation to take place. A CdL₂-MOF was reported to display selective adsorption towards six analogous six-membered ring substrates under mild conditions, with selectivity in decreasing order: 1,4-dioxane > cyclohexane > cyclohexene and benzene > cyclohexanone > cyclohexanol.⁹¹ Another interesting feature of this

Cd(II)-MOF is its intense green-yellow luminescence when completely evacuated, which can enable it to be applied as a sensor for detecting the six organic substrates in the environment.

Chun *et al.*⁹² studied the adsorption capacity of three Group IV-MOFs derived from 2,5-dihydroxyterephthalic acid (H₄dobdc). The Ti(IV)-MOF, abbreviated as Ti-dobdc, was shown to exhibit relatively high isosteric heats of adsorption toward H₂ and CO₂ at 6.6 and 29.4 kJ mol⁻¹, signifying the reversible adsorption of these gases within the linear 1D channels within the pores of the MOF. On the other hand, the isostructural Zr- and Hf-dobdc MOFs, having a general formula of (H₃O)_x[M(dobdc)(bz)_x] (where bz = benzoate), possess a nonoxo-trinuclear building unit that gives rise to a 6-connected topology polyhedral network. The N₂ adsorption isotherms of Fe-porphyrin-MOFs were studied by Fateeva *et al.*⁹³, utilizing tetrakis(4-carboxyphenyl)porphyrin (H₂TCPP) as the ligand, yielding crystalline Fe-MOFs synthesized solvothermally under basic conditions. For the MOF MIL-141(Fe), a value of 0.19 cm³ g⁻¹ was obtained for its pore volume, and its BET surface area was measured, giving a good agreement between the experimental and calculated values of 420 and 468 m² g⁻¹, respectively. In addition, the second Fe(III)-MOF, FepzTCPP(FeOH)₂ (where pz = pyrazine), possesses a pore volume of 0.33 cm³ g⁻¹, and the value of the experimental BET surface area was measured to be lower – 760 m² g⁻¹ – than the calculated value of 1460 m² g⁻¹. For the Fe(II)-MOF, FeTCPP(Febpy)₂ (where bpy = 4,4'-bipyridine), a BET surface area of 900 m² g⁻¹ was obtained, which was, again, lower than the theoretical value (2900 m² g⁻¹). This discrepancy was attributed to a possible structural collapse upon activation.

An efficient methane and carbon dioxide adsorption capacity has been reported for the Al-MOFs known as MOF-519 and MOF-520,⁹⁴ and MOFs based on γ -cyclodextrin (CD-MOF-2).⁹⁵ The permanently porous MOF-519 and MOF-520 displayed excellent volumetric capacities towards carbon dioxide at 200 and 162 cm³ cm⁻³ at 35 bar,

273 K.⁹⁴ Enhanced capacities of 279 and 231 cm³ cm⁻³ for MOF-519 and MOF-520, respectively, were recorded at the same temperature but at a higher pressure (80 bar). Adsorption studies using the green CD-MOF-2 revealed its highly CO₂-selective nature even at low pressures.⁹⁵ In addition, this nanoporous MOF was shown to undergo reversible carbon fixation and decomposition even at room temperature, as indicated by solid-state ¹³C-NMR spectroscopy and colorimetric studies. The action of certain MOFs in aqueous media for adsorbing selectively harmful organic substances, such as dyes, aromatics from spilled oil, and herbicides, has also been documented by Hasan *et al.*⁹⁶

4.4 MOFs as antibacterial agents

Careful selection of the inorganic and organic building blocks can generate MOFs with high bactericidal activity as well as biocompatibility. Numerous MOFs have been studied for their antibacterial activities against various bacterial species, with many reports focusing on *E. coli* and *S. aureus*. Among these, the Ag(I)-MOFs have long been well known for their antibacterial activity, particularly the Ag(I)-carboxylate MOFs,⁹⁷ as has the role of their structure-activity relationship in their bioactivity.⁹⁸

The Ag(I)-MOFs [Ag₂(O-IPA)(H₂O)·H₃O] and [Ag₅(PYDC)₂(OH)] (where HO-H₂IPA = 5-hydroxyisophthalic acid and H₂PYDC = pyridine-3,5-dicarboxylic acid) exhibited excellent antibacterial activity with minimum inhibitory concentrations in the ranges 5-10 ppm and 10-15 ppm against *E. coli*, and 10-15 ppm and 15-20 ppm against *S. aureus*, respectively. Interestingly, the antibacterial activity of these MOFs is much improved over that of the Ag-nanoparticles. Based on their study, the authors concluded that the MOFs exerted their bactericidal effect by the release of Ag(I) ions, which then interact with thiol groups of proteins, resulting in overall bacterial disintegration.

Other transition metal-based MOFs, such as Co(II)- and Cu(II)-MOFs, also possess some level of antibacterial activity. For example, a Co(II)-MOF assembled from 4,4'-[benzene-1,4-

diylbis(methylylidenenitrilo)]dibenzoic acid (H₂bdda), Co₂(bdda)_{1.5}(OAc)·5H₂O, has been subject to antibacterial studies using the agar well diffusion method against *E. coli* and *B. cereus*.⁷⁸ This Co(II)-MOF was discovered to possess a slight antibacterial effect, with the diameters of the inhibition zones being 2.3 ± 1 cm and 3.5 ± 1 cm, respectively. Jo *et al.*⁹⁹ reported the synthesis of four glutarate-derived Cu(II)-MOFs based on different pyridyl derivatives – 4,4'-bipyridine (bpy), 1,2-bis(4-pyridyl)ethane (bpa), 1,2-bis(4-pyridyl)ethylene (bpe), and 1,2-bis(4-pyridyl)propane (bpp). Studies of their minimal bactericidal concentrations (MBCs) against *E. coli*, *S. aureus*, *K. pneumonia*, *P. aeruginosa*, and MRSA indicated that all four MOFs displayed 99.9% bactericidal effectiveness with MBCs of 20 µg ml⁻¹. As to the activity of each individual component of the MOFs, Cu(II) ions were the most active species, followed by bpe, bpp, glutarate, bpy, and bpa. The authors argued that the bactericidal property of the four Cu(II)-MOFs was controlled predominantly by physical properties such as the surface area, porosities, and size of the particles, rather than by the leaching of Cu(II) ions from the framework structure. These studies illustrate the richness, as well as the complex antibacterial mechanisms, associated with different MOF materials.

5. Conclusion

MOFs are a class of hybrid compounds that have numerous applications in various fields, such as in catalysis, as sensors, in gas adsorption and separation, and as potential antibacterial agents. A diverse array of crystal structures for these MOFs can be obtained by varying the functional groups or substituents incorporated in the organic ligands used, and they are partly affected also by the nature of the counterions present. While carboxylate-based ligands are commonly employed, Schiff bases and pyridyl-derived ligands are of equal importance in the crystal engineering of MOF structures for a wide scope of applications. Although the exploration of the potential of MOFs has been ongoing for more than two decades now, more in-depth studies are needed to fully explore the realm of possibilities that MOFs can offer.

Conflict of interest

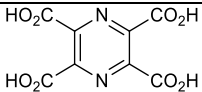
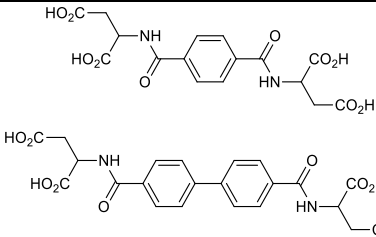
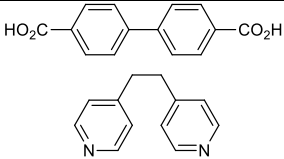
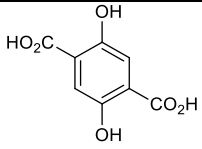
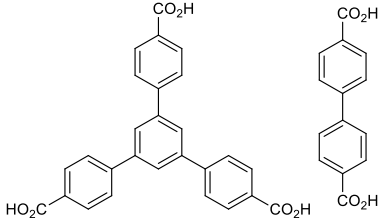
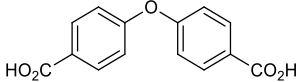
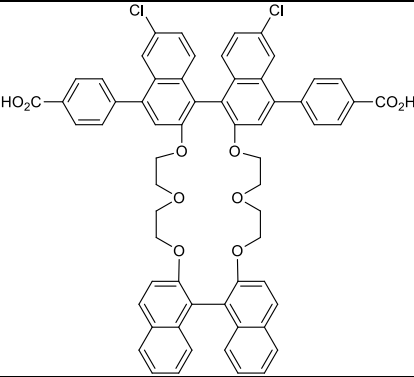
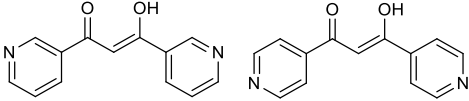
The authors have no conflicts of interest to declare.

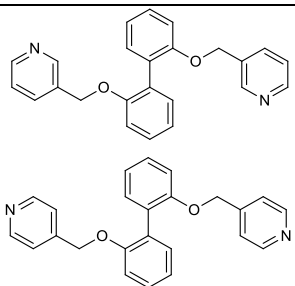
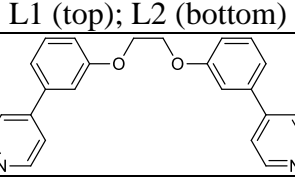
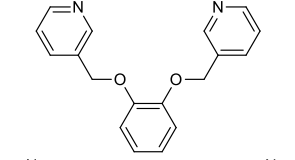
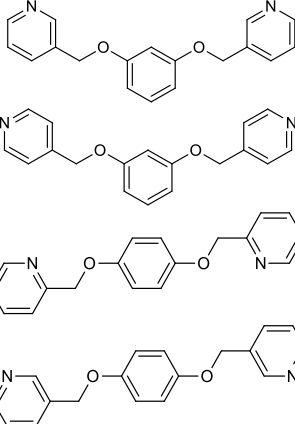
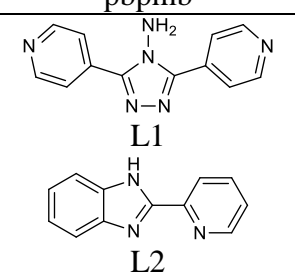
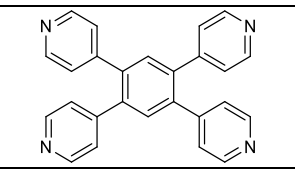
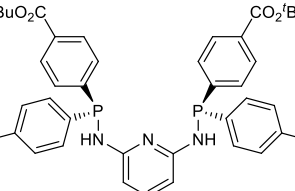
Acknowledgements

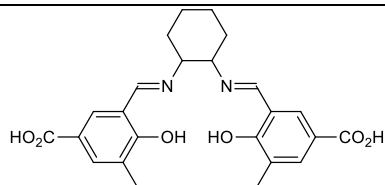
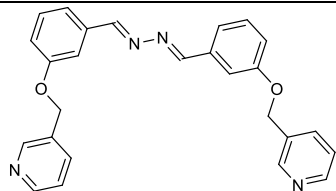
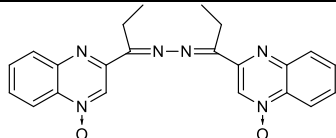
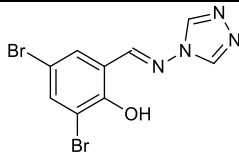
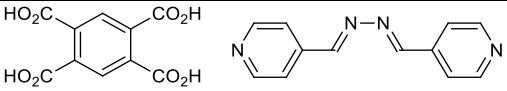
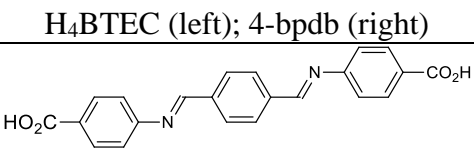
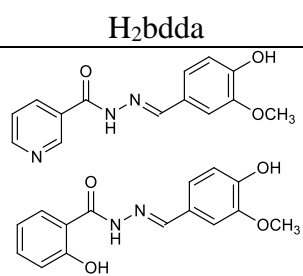
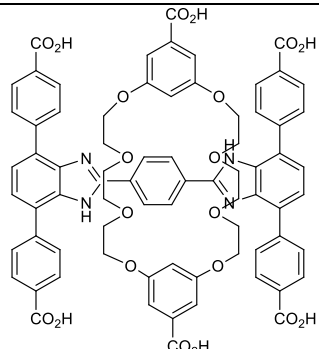
The work was supported by the Universiti Brunei Darussalam Graduate Scholarship.

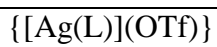
Table 1 Overview of organic ligands used in the construction of various MOFs.

MOF Formula	Metal ion	Ligand	Reference
Carboxylate derivatives			
$\{[\text{Ho}_8\text{Na}(\text{OH})_6\text{Cu}_{16}\text{I}_2(\text{L})_{24}](\text{NO}_3)_9(\text{H}_2\text{O})_6(\text{MeCN})_{18}\}_n$	Mixed metals		[29]
$\{[\text{Co}(\text{L})(\text{bpe})_{0.5}(\text{H}_2\text{O})]\cdot\text{H}_2\text{O}\}_n$ or $\{[\text{Co}(\text{L})(\text{bip})]\cdot 2\text{H}_2\text{O}\}_n$ (bpe = 1,2-bis(4-pyridyl)ethane; bip = 1,5-bis(imidazol)pentane)	Co^{II}		[30]
$[\text{Co}(\text{L})(\text{H}_2\text{O})_2]_n$ or $[\text{Co}(\text{L})(\text{H}_2\text{O})_4]_n(\text{H}_2\text{O})_n$	Co^{II}		[31]
$[\text{Ln}(\text{L})_2(\text{MeOH})_2\text{Ln}(\text{H}_2\text{O})_6\text{Mo}(\text{CN})_8]\cdot 8\text{H}_2\text{O}$ (Ln^{III} = Nd, Eu, Gd, Tb, or Er)	Ln^{III}		[32]
$[\text{UO}_2(\text{L})(\text{H}_2\text{O})_n]$ or $[(\text{UO}_2)_2\text{Cs}(\text{L})_2(\text{OH})(\text{H}_2\text{O})]$ ($n = 1, 2$)	UO_2^{2+}		[33]
$(\text{H}_3\text{O})_2[(\text{UO}_2)_2(\text{L})_3]\cdot\text{H}_2\text{O}$	UO_2^{2+}		[34]
$[\text{Zr}_6(\mu_3\text{-O})_4(\mu_3\text{-OH})_4(\mu\text{-OH})_2(\text{OH})_2(\text{H}_2\text{O})_2(\text{HCOO})_2(\text{L})_3]\cdot 10\text{H}_2\text{O}$	Zr^{IV}		[36]
$[\text{Cu}_2(\text{L}1)_2(\text{L}2)\text{Cl}]\cdot(\text{solvent})_x$ or $\{[\text{Ni}_3(\text{OH})(\text{L}2)_2(\text{L}1)[\text{NHMe}_2]]\}_n$	Cu^{II} or Ni^{II}		[37], [38]
$[\text{Ca}_2(\text{L})(\text{H}_2\text{O})_8]_n$ or $[\text{Ba}_2(\text{L})(\text{H}_2\text{O})_2]_n$	Ca^{II} or Ba^{II}		[39]
$[\text{Co}_3(\text{L})(\text{OH})_2(\text{H}_2\text{O})_4]\cdot\text{NMP}\cdot 3\text{H}_2\text{O}$ (NMP = 1-Methyl-2-pyrrolidinone)	Co^{II}		[40]

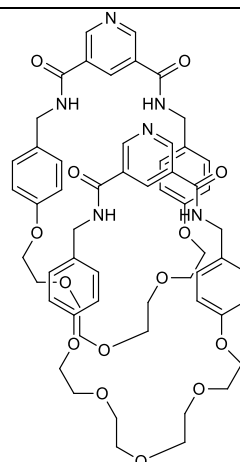
$[\text{K}_5\text{Ln}_5(\text{L})_5(\text{H}_2\text{O})_{19}] \cdot 7\text{H}_2\text{O}$ ($\text{Ln}^{\text{III}} = \text{Dy}, \text{Ho}, \text{or Yb}$)	$\text{K}^{\text{I}}\text{-Ln}^{\text{III}}$		[41]
$[\text{Na}_4(\text{L1})(\text{MeOH})(\text{H}_2\text{O})]$ or $[\text{Na}_4(\text{L2})(\text{H}_2\text{O})_2]$	Na^{I}		[42]
$[(\text{Fe}_3\text{O})_4(\text{SO}_4)_{12}(\text{BPDC})_6(\text{BPE})_6]^{8-}$ $\cdot 8[\text{NH}_2\text{Me}_2]^+ \cdot 13\text{H}_2\text{O} \cdot 8\text{DMF}$	Fe^{III}		[45]
$\text{Mg}_{0.269}\text{Ca}_{0.022}\text{Sr}_{0.030}\text{Ba}_{0.075}\text{Mn}_{0.234}\text{Fe}_{0.422}\text{Co}_{0.272}\text{Ni}_{0.282}\text{Zn}_{0.199}\text{Cd}_{0.196}(\text{DOT}) \cdot (\text{H}_2\text{O})_{7.8}$	Mixed transition metals		[46], [47]
$\text{Al}_8(\text{OH})_8(\text{BTB})_4(\text{BPDC})_2$	Al^{III}		[48]
$[\text{NaLn}(\text{L})(\text{ox})(\text{H}_2\text{O})]$ ($\text{Ln}^{\text{III}} = \text{Eu}, \text{or Sm}; \text{ox} = \text{oxalate}$)	$\text{Na}^{\text{I}}\text{-Ln}^{\text{III}}$		[54]
$[\text{Zn}_4\text{O}(\text{L})_3]$	Zn^{II}		[55]
Pyridyl and ether derivatives			
$[\text{AgFe}(\text{dppd})_3]\text{BF}_4 \cdot 2\text{DMSO} \cdot 2\text{H}_2\text{O}$ or $[\text{Ag}_2\text{Fe}(\text{dmppd})_3(\text{ONO}_2)]\text{NO}_3 \cdot \text{MeC N} \cdot \text{CH}_2\text{Cl}_2$	$\text{Ag}^{\text{I}}\text{-Fe}^{\text{III}}$		[49]

$[\text{Zn}_2(\text{L1})_2\text{Cl}_4]$ or $[\text{Zn}(\text{L2})\text{Cl}_2]_n$	Zn^{II}		[50]
$[\text{Cd}(\text{L})_2(\text{OTs})_2] \cdot 2(\text{solvent})$ (solvent = THF, PhF, PhBr)	Cd^{II}		[51]
$[\text{Cd}_2\text{Cl}_2(\text{L})(3\text{-obpmb})_2]_n$	Cd^{II}		[52], [53]
$\{[\text{Cd}_2(\text{L})_2(3\text{-mbpmb})_3] \cdot 2.5\text{H}_2\text{O}\}_n$			
$\{[\text{CdL}(4\text{-mbpmb})_2] \cdot \text{MeOH}\}_n$			
$[\text{Cd}_2(\text{L})_2(2\text{-pbpmb})]_n$			
$[\text{Cd}_2(\text{L})_2(3\text{-pbpmb})]_n$			
			
		(From top to bottom): 3-obpmb, 3-mbpmb, 4-mbpmb, 2-pbpmb, 3-pbpmb	
$[\text{Cd}(\text{SO}_4)(\text{L1})(\text{H}_2\text{O})]_n \cdot 3n\text{H}_2\text{O}$ or $[\text{Cd}(\text{D-cam})(\text{L2})(\text{H}_2\text{O})]_n$ (D-cam = D-camphorate)	Cd^{II}		[56]
$\{[\text{Ag}(\text{L})] \cdot \text{SbF}_6\}_n$	Ag^{I}		[57]
$[\text{Zr}_6\text{O}_4(\text{OH})_4(\text{OAc})_{2.4}\{(\text{P}^{\text{N}}\text{N}^{\text{N}}\text{P})\text{Pd}(\text{MeCN})\}_{2.4}(\text{BF}_4)_{2.4}$ ($\text{P}^{\text{N}}\text{N}^{\text{N}}\text{P}$ = 2,6-(HNPAr ₂) ₂ C ₅ H ₃ N; Ar = <i>p</i> -C ₆ H ₄ CO ₂ ⁻)	Zr^{IV}		[58]

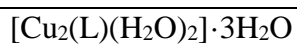
Schiff bases		
$[\text{BaNa}(\text{FeL})_2(\mu_2\text{-OH})(\text{H}_2\text{O})] \cdot \text{DMF} \cdot 2\text{H}_2\text{O}$	Mixed metals	 [73]
$\{[\text{Cd}(\text{L})(\text{SCN})_2] \cdot \text{CH}_2\text{Cl}_2\}_n$	Cd^{II}	 [74]
$\text{Ag}_3(\text{L})_2(\text{SbF}_6)_3 \cdot (\text{CHCl}_3) \cdot (\text{H}_2\text{O})$	Ag^{I}	 [75]
$[\text{M}(\text{L})_2]_n$ ($\text{M}^{\text{II}} = \text{Zn}, \text{Cd}$)	Zn^{II} or Cd^{II}	 [76]
$[\text{Co}_2(\text{BTEC})(4\text{-bpdb})(\text{H}_2\text{O})_2 \cdot 4\text{H}_2\text{O}]_n$	Co^{II}	 [77]
$\text{Co}_2(\text{bdda})_{1.5}(\text{OAc}) \cdot 5\text{H}_2\text{O}$	Co^{II}	 [78] H ₄ BTEC (left); 4-bpdb (right)
$[\text{Pb}_2(\text{L}_1)_2(\text{NO}_3)_2] \cdot 3\text{H}_2\text{O}$ or $[\text{Co}(\text{L}_2)_2(\text{py})_2] \cdot \text{ClO}_4$	Pb^{II} or Co^{III}	 [79] H ₂ bdda L ₁ (top); L ₂ (bottom)
Mechanically interlocked molecules		
$[\text{NH}_2\text{Me}_2]_2\{\text{Zn}_2\{\text{H}_2\text{O}\}_2(\text{L})\}$	Zn^{II}	 [25]



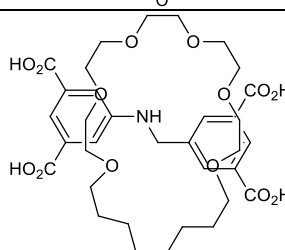
Ag^I



[26]



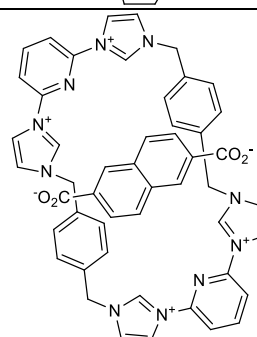
Cu^{II}



[27]

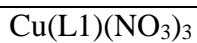


Ag^I or
Zn^{II}

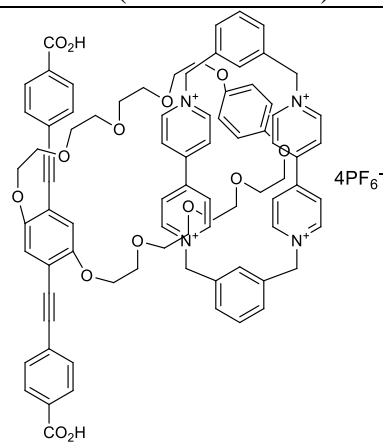


[80]

L = (NDC ⊂ TSMB)



Cu^{II}



[82]

4PF₆⁻

H₂L1

Table 2. Overview of applications of some MOFs.

MOF formula	Description	Reference
IRMOF-3-SI-Au	Post synthetic modification-induced catalysis	[85]
Mo(acac) ₂ -UiO-66-NH ₂ MOF	Epoxidation of cyclic and aliphatic alkenes	[86]
Pd-pySal-Cu(BDC)	Mizoroki-Heck coupling reaction	[87]
Ln(4,4'-bipy)	Luminescence tuning by variation of Eu ^{III} /Tb ^{III} /Gd ^{III} ratio Presence of microporosity and mesoporosity (0.6-1.8 nm) BET surface area = 660 m ² g ⁻¹	[88]
Eu _{1.5} (L)	Exhibits intense red luminescence ($\phi = 73\%$)	[89]
[Cd(dpm) ₂]	First series of luminescent Cd-MOFs bearing mono-dpm ligands	[90]
Cd(L) ₂ -MOF	Selective adsorption of 6-membered ring substrates at mild conditions Exhibits intense green-yellow luminescence of evacuated MOF	[91]
(H ₃ O) _x (M(dobdc)(bz) _x) (M = Zr, Hf)	Reversible adsorption of H ₂ and CO ₂	[92]
FeTCPP(Febpy) ₂ and FepzTCPP(FeOH) ₂	Adsorption studies of N ₂ BET surface area = 900 and 760 m ² g ⁻¹	[93]
MOF-519 and MOF-520	Excellent CO ₂ volumetric capacities of 200 and 162 cm ³ cm ⁻³ at 273 K, 35 bar	[94]
CD-MOF-2	High selective adsorption of CO ₂ at low pressures Reversible carbon fixation and decomposition at room temperature	[95]
[Ag ₂ (O-IPA)(H ₂ O)·H ₃ O)] and [Ag ₅ (PYDC) ₂ (OH)]	Antibacterial active against <i>E. coli</i> and <i>S. aureus</i> with MIC values of 5-20 ppm	[97]
Co ₂ (bdda) _{1.5} (OAc)·5H ₂ O	Exhibits antibacterial property against <i>E. coli</i> and <i>B. cereus</i> with MIC values of 2.3 ± 1 cm and 3.5 ± 1 cm, respectively	[78]
[Cu ₂ (Glu) ₂ (X)]·nH ₂ O (X = bpy, bpa, bpe, bpp)	MBC value of 20 µg ml ⁻¹ against <i>E. coli</i> , <i>S. aureus</i> , <i>K. pneumonia</i> , <i>P. aeruginosa</i> and MRSA	[99]

References

- [1] O. M. Yaghi, G. Li, and H. Li, "Selective Binding and Removal of Guests in a Microporous Metal-Organic Framework," *Nature*, vol. 378, no. 6558, p. 703, 1995.
- [2] O. M. Yaghi and Q. Li, "Reticular Chemistry and Metal-Organic Frameworks for Clean Energy," *MRS Bull.*, vol. 34, no. 9, pp. 682-690, 2009.
- [3] Y. Dong, M. D. Smith, R. C. Layland, and H. Loye, "A Novel Noninterpenetrating Polycyclohexane Network: A New Inorganic/Organic Coordination Polymer Structural Motif Generated by Self-Assembly of 'T-Shaped' Moieties," *Chem. Mater.*, vol. 12, no. 4, pp. 1156-1161, 2000.
- [4] K. K. Gangu, S. Maddila, S. B. Mukkamala, and S. B. Jonnalagadda, "A Review on Contemporary Metal-Organic Framework Materials," *Inorganica Chim. Acta*, vol. 446, pp. 61-74, 2016.
- [5] I. Imaz and D. Maspoch, "Self-Assembly of Coordination Chains and Helices," in *Supramolecular Chemistry: From Molecules to Nanomaterials*, 1st ed., vol. 5, P. A. Gale and J. W. Steed, Eds. West Sussex: John Wiley & Sons, Ltd, 2012, pp. 2045-2069.

- [6] N. Stock and S. Biswas, "Synthesis of Metal-Organic Frameworks (MOFs): Routes to Various MOF Topologies, Morphologies, and Composites," *Chem. Rev.*, vol. 112, no. 2, pp. 933-969, 2012.
- [7] D. J. Tranchemontagne, J. R. Hunt, and O. M. Yaghi, "Room Temperature Synthesis of Metal-Organic Frameworks: MOF-5, MOF-74, MOF-177, MOF-199, and IRMOF-0," *Tetrahedron*, vol. 64, pp. 8553-8557, 2008.
- [8] G. G. da Silva, F. L. A. Machado, S. A. Junior, and E. Padrón-Hernández, "Metal-Organic Framework: Structure and Magnetic Properties of $[\text{Cu}_3(\text{BTC})_2(\text{L})_x(\text{CuO})_y]_n$ ($\text{L}=\text{H}_2\text{O}$, DMF)," *J. Solid State Chem.*, vol. 253, pp. 1-5, Sep. 2017.
- [9] J. I. Feldblyum, M. Liu, D. W. Gidley, and A. J. Matzger, "Reconciling the discrepancies between crystallographic porosity and guest access as exemplified by Zn-HKUST-1," *J. Am. Chem. Soc.*, vol. 133, no. 45, pp. 18257-18263, Nov. 2011.
- [10] Y. R. Lee, J. Kim, and W. S. Ahn, "Synthesis of Metal-Organic Frameworks: A Mini Review," *Korean J. Chem. Eng.*, vol. 30, no. 9, pp. 1667-1680, 2013.
- [11] R. González-Prieto, S. Herrero, R. Jiménez-Aparicio, and 4 others, "Microwave-Assisted Solvothermal Synthesis of Inorganic Compounds (Molecular and Non Molecular)," *Microw. Chem.*, no. February 2018, pp. 225-247, 2017.
- [12] D. Chen, J. Zhao, P. Zhang, and S. Dai, "Mechanochemical Synthesis of Metal-Organic Frameworks," *Polyhedron*, vol. 162, pp. 59-64, 2019.
- [13] A. Pichon, A. Lazuen-Garay, and S. L. James, "Solvent-Free Synthesis of a Microporous Metal-Organic Framework," *CrystEngComm*, vol. 8, no. 3, pp. 211-214, 2006.
- [14] M. G. Campbell, D. Sheberla, S. F. Liu, T. M. Swager, and M. Dincă, "Cu₃(hexaiminotriphenylene)₂: An Electrically Conductive 2D Metal-Organic Framework for Chemiresistive Sensing," *Angew. Chemie - Int. Ed.*, vol. 54, no. 14, pp. 4349-4352, 2015.
- [15] C.-S. Liu, Z. Chang, J.-J. Wang, L.-F. Yan, X.-H. Bu, and S. R. Batten, "A Photoluminescent 3D Silver(I) Coordination Polymer with Mixed Ligands Anthracene-9,10-dicarboxylate and Hexamethylenetetramine, Showing Binodal 4-Connected (43·63)₂(42·62·82)₃ Topology," *Inorg. Chem. Commun.*, vol. 11, no. 8, pp. 889-892, Aug. 2008.
- [16] D. Sheberla, L. Sun, M. Blood-Forsythe and 5 others, "High Electrical Conductivity in Ni₃(2,3,6,7,10,11-hexaiminotriphenylene)₂, a Semiconducting Metal-Organic Graphene Analogue," *J. Am. Chem. Soc.*, vol. 136, pp. 8859-8862, 2014.
- [17] F.-L. Liu, Z.-H. Xu, X.-Y. Zhang, X.-P. Wang, and D. Sun, "Unusual N-H Activation of 2-Aminopyrimidine: Supramolecular Assembly into an AgI Metal-Organic Framework," *Chem. - An Asian J.*, vol. 9, no. 2, pp. 452-456, Feb. 2014.
- [18] P. Li, S. Regati, H. C. Huang, H. D. Arman, B. L. Chen, and J. C. G. Zhao, "A Sulfonate-Based Cu(I) Metal-Organic Framework as a Highly Efficient and Reusable Catalyst for the Synthesis of Propargylamines Under Solvent-Free Conditions," *Chinese Chem. Lett.*, vol. 26, no. 1, pp. 6-10, 2015.
- [19] X. L. Zhang, G. M. Tang, and Y. T. Wang, "Tunable Luminescent Behaviors of Ag-Containing Metal Coordination Polymers with N-Heterocyclic and Sulfonate Group," *Polyhedron*, vol. 147, pp. 26-35, 2018.
- [20] X. L. Zhang, G. M. Tang, and Y. T. Wang, "A Set of Ag-Based Metal Coordination Polymers with Sulfonate Group: Syntheses, Crystal Structures and Luminescent Behaviors," *Polyhedron*, vol. 148, pp. 55-69, 2018.
- [21] M. Bazaga-García, R. M. P. Colodrero, M. Papadaki and 9 others, "Guest Molecule-Responsive Functional Calcium Phosphonate Frameworks for Tuned Proton Conductivity," *J. Am. Chem. Soc.*, vol. 136, no. 15, pp. 5731-5739, 2014.
- [22] P. Deria, W. Bury, I. Hod and 4 others,

- “MOF Functionalization via Solvent-Assisted Ligand Incorporation: Phosphonates vs Carboxylates,” *Inorg. Chem.*, vol. 54, no. 5, pp. 2185-2192, 2015.
- [23] Z. H. Fard, Y. Kalinovsky, D. M. Spasyuk, B. A. Blight, and G. K. H. Shimizu, “Alkaline-Earth Phosphonate MOFs with Reversible Hydration-Dependent Fluorescence,” *Chem. Commun.*, vol. 52, no. 87, pp. 12865-12868, 2016.
- [24] K. J. Gagnon, H. P. Perry, and A. Clearfield, “Conventional and Unconventional Metal-Organic Frameworks Based on Phosphonate Ligands: MOFs and UMOFs,” *Chem. Rev.*, vol. 112, no. 2, pp. 1034-1054, 2012.
- [25] G. Gholami, K. Zhu, J. S. Ward, P. E. Kruger, and S. J. Loeb, “Formation of a Polythreaded, Metal-Organic Framework Utilizing an Interlocked Hexadentate, Carboxylate Linker,” *Eur. J. Inorg. Chem.*, vol. 2016, no. 27, pp. 4524-4529, 2016.
- [26] J. E. M. Lewis, “Self-Templated Synthesis of Amide Catenanes and Formation of a Catenane Coordination Polymer,” *Org. Biomol. Chem.*, vol. 17, no. 9, pp. 2442-2447, 2019.
- [27] V. N. Vukotic, K. J. Harris, K. Zhu, R. W. Schurko, and S. J. Loeb, “Metal-Organic Frameworks with Dynamic Interlocked Components,” *Nat. Chem.*, vol. 4, no. 6, pp. 456-460, 2012.
- [28] S. Yuan, L. Feng, K. Wang and 14 others, “Stable Metal-Organic Frameworks: Design, Synthesis, and Applications,” *Adv. Mater.*, vol. 30, no. 37, p. 1704303, Sep. 2018.
- [29] M. Zhao, S. Chen, Y. Huang, and Y. Dan, “An Unusual 2p-3d-4f Heterometallic Coordination Polymer Featuring Ln₈Na and Cu₈I Clusters as Nodes,” *J. Mol. Struct.*, vol. 1128, pp. 123-126, 2017.
- [30] X.-H. Chang, L.-F. Ma, G. Hui, and L.-Y. Wang, “Four Low-Dimensional Cobalt(II) Coordination Polymers Based on a New Isophthalic Acid Derivative: Syntheses, Crystal Structures, and Properties,” *Cryst. Growth Des.*, vol. 12, no. 7, pp. 3638-3646, Jul. 2012.
- [31] A. Cheansirisomboon, C. Pakawatchai, and S. Youngme, “2D-1D Structural Phase Transformation of Co(II) 3,5-Pyridinedicarboxylate Frameworks with Chromotropism,” *Dalt. Trans.*, vol. 41, no. 35, pp. 10698-10706, Aug. 2012.
- [32] S. Tanase, M. C. Mittelmeijer-Hazeleger, G. Rothenberg and 4 others, “A Facile Building-Block Synthesis of Multifunctional Lanthanide MOFs,” *J. Mater. Chem.*, vol. 21, no. 39, pp. 15544-15551, Sep. 2011.
- [33] B. Masci and P. Thuéry, “Hydrothermal Synthesis of Uranyl-Organic Frameworks with Pyrazine-2,3-dicarboxylate Linkers,” *CrystEngComm*, vol. 10, no. 8, pp. 1082-1087, Jul. 2008.
- [34] W. Xu, Y.-N. Ren, M. Xie, L.-X. Zhou, and Y.-Q. Zheng, “Six Uranyl-Organic Frameworks with Naphthalene-Dicarboxylic Acid and Bipyridyl-Based Spacers: Syntheses, Structures, and Properties,” *Dalt. Trans.*, vol. 47, no. 12, pp. 4236-4250, Mar. 2018.
- [35] J.-N. Rebilly, J. Bacsá, and M. J. Rosseinsky, “1D Tubular and 2D Metal-Organic Frameworks Based on a Flexible Amino Acid Derived Organic Spacer,” *Chem. - An Asian J.*, vol. 4, no. 6, pp. 892-903, Jun. 2009.
- [36] S. Waitschat, H. Reinsch, and N. Stock, “Water-Based Synthesis and Characterisation of a New Zr-MOF with a Unique Inorganic Building Unit,” *Chem. Commun.*, vol. 52, no. 86, pp. 12698-12701, 2016.
- [37] A. Nath, S. Das, P. Mukharjee, R. Nath, D. Kuznetsov, and S. Mandal, “Frustrated Magnetism in Cu(II) Based Metal-Organic Framework,” *Inorganica Chim. Acta*, vol. 486, no. August 2018, pp. 158-161, 2019.
- [38] J. Y. Tan, J. X. Shi, P. H. Cui and 4 others, “A Ni₃(OH)(COO)₆-Based MOF from C₃ Symmetric Ligands: Structure and Heterogeneous Catalytic Activities in One-Pot Synthesis of Imine,” *Microporous Mesoporous Mater.*, vol. 287, no. March, pp. 152-158, 2019.

- [39] S. Du, C. Ji, X. Xin and 5 others, "Syntheses, Structures and Characteristics of Four Alkaline-Earth Metal-Organic Frameworks (MOFs) Based on Benzene-1,2,4,5-tetracarboxylic Acid and Its Derivative Ligand," *J. Mol. Struct.*, vol. 1130, pp. 565-572, Feb. 2017.
- [40] Y. Wu, S. Cheng, J. Liu, G. Yang, and Y. Y. Wang, "New Porous Co(II)-Based Metal-Organic Framework including 1D Ferromagnetic Chains with Highly Selective Gas Adsorption and Slow Magnetic Relaxation," *J. Solid State Chem.*, vol. 276, no. May, pp. 226-231, 2019.
- [41] F. Zhang, P. Yan, X. Zou, J. Zhang, G. Hou, and G. Li, "Novel 3D Alkali-Lanthanide Heterometal-Organic Frameworks with Pyrazine-2,3,5,6-tetracarboxylic Acid: Synthesis, Structure, and Magnetism," *Cryst. Growth Des.*, vol. 14, no. 4, pp. 2014-2021, Apr. 2014.
- [42] P. Siman, C. A. Trickett, H. Furukawa, and O. M. Yaghi, "1-Aspartate Links for Stable Sodium Metal-Organic Frameworks," *Chem. Commun.*, vol. 51, no. 98, pp. 17463-17466, Nov. 2015.
- [43] I. Imaz, M. Rubio-Martínez, J. An, I. Sole-Font, N. L. Rosi, and D. Maspoch, "Metal-Biomolecule Frameworks (MBioFs)," *Chem. Commun.*, vol. 47, no. 26, pp. 7287-7302, 2011.
- [44] M. Eddaoudi, D. B. Moler, H. Li and 4 others, "Modular Chemistry: Secondary Building Units as a Basis for the Design of Highly Porous and Robust Metal-Organic Carboxylate Frameworks," *Acc. Chem. Res.*, vol. 34, no. 4, pp. 319-330, 2001.
- [45] A. C. Sudik, A. P. Côte, A. G. Wong-foy, M. O. Keeffe, and O. M. Yaghi, "A Metal-Organic Framework with a Hierarchical System of Pores and Tetrahedral Building Blocks," *Angew. Chemie Int. Ed.*, vol. 45, no. 16, pp. 2528-2533, 2006.
- [46] H. Deng, S. Grunder, K. E. Cordova and 12 others, "Large-Pore Apertures in a Series of Metal-Organic Frameworks," *Science (80-.)*, vol. 336, no. 6084, pp. 1018-1023, 2012.
- [47] L. J. Wang, H. Deng, H. Furukawa and 4 others, "Synthesis and Characterization of Metal-Organic Framework-74 Containing 2, 4, 6, 8, and 10 Different Metals," *Inorg. Chem.*, vol. 53, no. 12, pp. 5881-5883, 2014.
- [48] E. A. Kapustin, S. Lee, A. S. Alshammari, and O. M. Yaghi, "Molecular Retrofitting Adapts a Metal-Organic Framework to Extreme Pressure," *ACS Cent. Sci.*, vol. 3, no. 6, pp. 662-667, 2017.
- [49] A. D. Burrows, M. F. Mahon, C. L. Renouf, C. Richardson, A. J. Warren, and J. E. Warren, "Dipyridyl β -Diketonate Complexes and Their Use as Metalloligands in the Formation of Mixed-Metal Coordination Networks," *Dalt. Trans.*, vol. 41, no. 14, pp. 4153-4163, 2012.
- [50] R. Wang, L. Han, L. Xu and 4 others, "Syntheses and Characterizations of Metal-Organic Frameworks with Unusual Topologies Derived from Flexible Dipyridyl Ligands," *Eur. J. Inorg. Chem.*, vol. 2004, no. 18, pp. 3751-3763, 2004.
- [51] L. Wang, Y. Li, F. Yang, Q. Liu, and Y. Dong, "Cd(II)-MOF: Adsorption, Separation, and Guest-Dependent Luminescence for Monohalobenzenes," *Inorg. Chem.*, vol. 53, no. 17, pp. 9087-9094, 2014.
- [52] L. Liu, C. Yu, F. Ma and 4 others, "Structural Diversity and Photocatalytic Properties of Cd (II) Coordination Polymers Constructed by a Flexible V-Shaped Bipyridyl Benzene Ligand and Dicarboxylate Derivatives," *Dalt. Trans.*, vol. 44, no. 4, pp. 1636-1645, 2015.
- [53] L. L. Liu, C. X. Yu, Y. R. Li, J. J. Han, F. J. Ma, and L. F. Ma, "Positional Isomeric Effect on the Structural Variation of Cd (II) Coordination Polymers Based on Flexible Linear/V-Shaped Bipyridyl Benzene Ligands," *CrystEngComm*, vol. 17, no. 3, pp. 653-664, 2015.
- [54] C. Wang, G. Guo, and P. Wang, "Two Sodium and Lanthanide(III) MOFs Based on Oxalate and V-Shaped 4,4'-Oxybis(benzoate) Ligands: Hydrothermal Synthesis, Crystal Structure, and

- Luminescence Properties,” *J. Mol. Struct.*, vol. 1032, pp. 93-99, Jan. 2013.
- [55] C. Valente, E. Choi, M. E. Belowich and 6 others, “Metal-Organic Frameworks with Designed Chiral Recognition Sites,” *Chem. Commun.*, vol. 46, no. 27, pp. 4911-4913, 2010.
- [56] N. Chen, M. X. Li, P. Yang, X. He, M. Shao, and S. R. Zhu, “Chiral Coordination Polymers with SHG-Active and Luminescence: An Unusual Homochiral 3D MOF Constructed from Achiral Components,” *Cryst. Growth Des.*, vol. 13, no. 6, pp. 2650-2660, 2013.
- [57] Y. Sun and H. Han, “A Novel 3D AgI Cationic Metal-Organic Framework Based on 1,2,4,5-Tetra(4-pyridyl)benzene with Selective Adsorption of CO₂ over CH₄, H₂O over C₂H₅OH, and Trapping Cr₂O₇²⁻,” *J. Mol. Struct.*, vol. 1194, pp. 73-77, 2019.
- [58] B. R. Reiner, A. A. Kassie, and C. R. Wade, “Unveiling Reactive Metal Sites in a Pd Pincer MOF: Insights into Lewis Acid and Pore Selective Catalysis,” *Dalt. Trans.*, vol. 48, no. 26, pp. 9588-9595, 2019.
- [59] N. E. Borisova, M. D. Reshetova, and Y. A. Ustynyuk, “Metal-free methods in the synthesis of macrocyclic Schiff bases,” *Chem. Rev.*, vol. 107, no. 1, pp. 46-79, 2007.
- [60] W. Al Zoubi, “Biological Activities of Schiff Bases and Their Complexes: A Review of Recent Works,” *Int. J. Org. Chem.*, vol. 03, no. 03, pp. 73-95, 2013.
- [61] D. Dragancea, A. W. Addison, M. Zeller and 4 others, “Dinuclear Copper(II) Complexes with Bis-Thiocarbohydrazone Ligands,” *Eur. J. Inorg. Chem.*, vol. 2008, no. 16, pp. 2530-2536, 2008.
- [62] V. Stilinović, D. Cinčić, M. Zbačnik, and B. Kaitner, “Controlling Solvate Formation of a Schiff Base by Combining Mechanochemistry with Solution Synthesis,” *Croat. Chem. Acta*, vol. 85, no. 4, pp. 485-493, 2012.
- [63] S. Chigurupati, S. Muralidharan, L. S. Cin, W. Y. Raser, K. Santhi, and K. S. Kesavanarayanan, “Studying Newly Synthesized and Developed 4-Hydroxy-3-Methoxybenzaldehyde Schiff Bases by UV Spectrophotometry and High Performance Liquid Chromatography,” *Pharm. Chem. J.*, vol. 50, no. 12, pp. 851-856, 2017.
- [64] D. H. Jornada, G. F. Dos Santos Fernandes, D. E. Chiba, T. R. F. De Melo, J. L. Dos Santos, and M. C. Chung, “The Prodrug Approach: A Successful Tool for Improving Drug Solubility,” *Molecules*, vol. 21, no. 1, p. 42, 2016.
- [65] S. Prasad and K. Susila, “An Overview on Schiff Bases and Its Medicinal Chemistry Potential for New Antitubercular Drug Molecules Research,” *Rev. Roum. Chim.*, vol. 62, no. 1, pp. 65-79, 2017.
- [66] K. H. M. E. Tehrani, S. Sardari, V. Mashayekhi, M. Esfahani Zadeh, P. Azerang, and F. Kobarfard, “One Pot Synthesis and Biological Activity Evaluation of Novel Schiff Bases Derived from 2-Hydrazinyl-1,3,4-thiadiazole,” *Chem. Pharm. Bull. (Tokyo)*, vol. 61, no. 2, pp. 160-166, 2013.
- [67] C. Vartzouma, E. Evaggellou, Y. Sanakis, N. Hadjiliadis, and M. Louloudi, “Alkene Epoxidation by Homogeneous and Heterogenised Manganese(II) Catalysts with Hydrogen Peroxide,” *J. Mol. Catal. A Chem.*, vol. 263, no. 1-2, pp. 77-85, 2007.
- [68] B. K. Momidi, V. Tekuri, and D. R. Trivedi, “Multi-Signaling Thiocarbohydrazone Based Colorimetric Sensors for the Selective Recognition of Heavy Metal Ions in an Aqueous Medium,” *Spectrochim. Acta Part A Mol. Biomol. Spectrosc.*, vol. 180, pp. 175-182, 2017.
- [69] C. Biswas, M. G. B. Drew, and A. Ghosh, “Stabilization of a Helical Water Chain in a Metal-Organic Host of a Trinuclear Schiff Base Complex,” *Inorg. Chem.*, vol. 47, no. 11, pp. 4513-4519, 2008.
- [70] B. T. Thaker, P. Patel, A. D. Vansadia, and H. G. Patel, “Synthesis, Characterization, and Mesomorphic Properties of New Liquid-Crystalline Compounds Involving Ester-Azomethine Central Linkages, Lateral Substitution, and a Thiazole Ring,” *Mol. Cryst. Liq. Cryst.*, vol. 466, no. 1, pp.

- 13-22, 2007.
- [71] M. Zbačnik, I. Nogalo, D. Cinčić, and B. Kaitner, "Polymorphism Control in the Mechanochemical and Solution-Based Synthesis of a Thermochromic Schiff Base," *CrystEngComm*, vol. 17, no. 41, pp. 7870-7877, 2015.
- [72] M. Zbačnik, K. Pičuljan, J. Parlov-Vuković, P. Novak, and A. Roodt, "Four Thermochromic o-Hydroxy Schiff Bases of α -Aminodiphenylmethane: Solution and Solid State Study," *Crystals*, 2017.
- [73] H. H. Wang, J. Yang, Y. Y. Liu, S. Song, and J. F. Ma, "Heterotrimetallic Organic Framework Assembled with FeIII/BaII/NaI and Schiff Base: Structure and Visible Photocatalytic Degradation of Chlorophenols," *Cryst. Growth Des.*, vol. 15, no. 10, pp. 4986-4992, 2015.
- [74] J. Xiao, C. Chen, Q. Liu, J. Ma, and Y. Dong, "Cd (II)-Schiff-Base Metal-Organic Frameworks: Synthesis, Structure, and Reversible Adsorption and Separation of Volatile Chlorocarbons," *Cryst. Growth Des.*, vol. 11, no. 12, pp. 5696-5701, 2011.
- [75] J. Y. Cheng, P. Wang, J. P. Ma, Q. K. Liu, and Y. B. Dong, "A Nanoporous Ag (I)-MOF Showing Unique Selective Adsorption of Benzene Among its Organic Analogues," *Chem. Commun.*, vol. 50, no. 89, pp. 13672-13675, 2014.
- [76] S. Zhang, J. Wang, H. Zhang, Y. Fan, and Y. Xiao, "Highly Efficient Electrochemiluminescence Based on 4-Amino-1,2,4-triazole Schiff Base Two-Dimensional Zn/Cd Coordination Polymers," *Dalt. Trans.*, vol. 46, no. 2, pp. 410-419, 2017.
- [77] Q. Sun, X. Zhu, N. Zhang, B. Zhang, J. Lu, and H. Liu, "Auxiliary Ligand-Assisted Structural Variation of Two Co (II) Metal-Organic Frameworks: Syntheses, Crystal Structure and Magnetic Properties," *Inorg. Chem. Commun.*, vol. 99, pp. 172-175, 2019.
- [78] S. Aryanejad, G. Bagherzade, and M. Moudi, "Design and Development of Novel Co - MOF Nanostructures as an Excellent Catalyst for Alcohol Oxidation and Henry Reaction, with a Potential Antibacterial Activity," *Appl. Organomet. Chem.*, vol. 33, no. 9, p. e4820, 2019.
- [79] S. Li, S. Gao, S. Liu, and Y. Guo, "Five Metal (II) Coordination Polymers Constructed from Two Vanillin Derivatives: From Discrete Structure to 3D Diamondoid Network," *Cryst. Growth Des.*, vol. 10, no. 2, pp. 495-503, 2010.
- [80] K. Zhu and S. J. Loeb, "Organizing Mechanically Interlocked Molecules to Function Inside Metal-Organic Frameworks," in *Top Current Chemistry*, no. 0000, Springer, 2014, pp. 1-39.
- [81] Q. Li, C.-H. Sue, S. Basu and 7 others, "A Catenated Strut in a Catenated Metal-Organic Framework," *Angew. Chemie Int. Ed.*, vol. 49, no. 38, pp. 6751-6755, 2010.
- [82] Q. Li, W. Zhang, S. Ognjen, J. F. Stoddart, and O. M. Yaghi, "A Metal-Organic Framework Replete with Ordered Donor-Acceptor Catenanes," *Chem. Commun.*, vol. 46, no. 3, pp. 380-382, 2010.
- [83] S. Zhang, Q. Yang, X. Liu and 5 others, "High-Energy Metal-Organic Frameworks (HE-MOFs): Synthesis, Structure and Energetic Performance," *Coord. Chem. Rev.*, vol. 307, pp. 292-312, Jan. 2016.
- [84] J. Jiang and O. M. Yaghi, "Brønsted Acidity in Metal-Organic Frameworks," *Chem. Rev.*, vol. 115, no. 14, pp. 6966-6997, Jul. 2015.
- [85] X. Zhang, F. X. L. Xamena, and A. Corma, "Gold (III)-Metal Organic Framework Bridges the Gap Between Homogeneous and Heterogeneous Gold Catalysts," *J. Catal.*, vol. 265, no. 2, pp. 155-160, 2009.
- [86] R. Kardanpour, S. Tangestaninejad, V. Mirkhani, M. Moghadam, I. Mohammadpoor-Baltork, and F. Zadehahmadi, "Efficient Alkene Epoxidation Catalyzed by Molybdenyl Acetylacetonate Supported on Aminated UiO-66 Metal-Organic Framework," *J. Solid State Chem.*, vol. 226, pp. 262-272, 2015.
- [87] H. Alamgholiloo, S. Rostamnia, A. Hassankhani and 4 others, "Stepwise Post-Modification Immobilization of Palladium

- Schiff- Base Complex on to the OMS- Cu (BDC) Metal-Organic Framework for Mizoroki- Heck Cross- Coupling Reaction,” *Appl. Organomet. Chem.*, vol. 32, no. 11, p. e4539, 2018.
- [88] P. R. Matthes, C. J. Höller, M. Mai and 6 others, “Luminescence Tuning of MOFs via Ligand to Metal and Metal to Metal Energy Transfer by Co-Doping of 2∞ [Gd 2 Cl 6 (bipy) 3]· 2bipy with Europium and Erbium,” *J. Mater. Chem.*, vol. 22, no. 20, pp. 10179-10187, 2012.
- [89] A. Duerrbeck, S. Gorelik, J. Hobley, A. Hor, and N. Long, “Highly Emissive, Solution-Processable and Dynamic Eu (III)-Containing Coordination Polymers,” *Chem. Commun.*, vol. 41, no. 41, pp. 8656-8659, 2015.
- [90] A. Béziau, S. A. Baudron, A. Guenet, and M. W. Hosseini, “Luminescent Coordination Polymers Based on Self-Assembled Cadmium Dipyrrin Complexes,” *Chem. Eur. J.*, vol. 19, no. 9, pp. 3215-3223, 2013.
- [91] L. Duan, Z. Wu, J. Ma, X. Wu, and Y. Dong, “Adsorption and Separation of Organic Six-Membered Ring Analogues on Neutral Cd (II) -MOF Generated from Asymmetric Schiff-Base Ligand,” *Inorg. Chem.*, vol. 49, no. 23, pp. 11164-11173, 2010.
- [92] H. Chun and D. Moon, “Metal–Organic Frameworks from Group 4 Metals and 2,5-Dihydroxyterephthalic Acid: Reinvestigation, New Structure, and Challenges Toward Gas Storage and Separation,” *Cryst. Growth Des.*, vol. 17, no. 4, pp. 2140-2146, 2017.
- [93] A. Fateeva, J. Clarisse, G. Pilet and 9 others, “Iron and Porphyrin Metal–Organic Frameworks: Insight into Structural Diversity, Stability, and Porosity,” *Cryst. Growth Des.*, vol. 15, no. 4, pp. 1819-1826, 2015.
- [94] F. Gándara, H. Furukawa, S. Lee, and O. M. Yaghi, “High Methane Storage Capacity in Aluminum Metal-Organic Frameworks,” *J. Am. Chem. Soc.*, vol. 136, no. 14, pp. 5271-5274, Apr. 2014.
- [95] J. J. Gassensmith, H. Furukawa, R. A. Smaldone and 4 others, “Strong and Reversible Binding of Carbon Dioxide in a Green Metal-Organic Framework,” *J. Am. Chem. Soc.*, vol. 133, no. 39, pp. 15312-15315, Oct. 2011.
- [96] Z. Hasan and S. H. Jung, “Removal of Hazardous Organics from Water Using Metal-Organic Frameworks (MOFs): Plausible Mechanisms for Selective Adsorptions,” *J. Hazard. Mater.*, vol. 283, pp. 329-339, Feb. 2015.
- [97] X. Lu, J. Ye, D. Zhang and 6 others, “Silver Carboxylate Metal-Organic Frameworks with Highly Antibacterial Activity and Biocompatibility,” *J. Inorg. Biochem.*, vol. 138, pp. 114-121, Sep. 2014.
- [98] R. Karimi Alavijeh, S. Beheshti, K. Akhbari, and A. Morsali, “Investigation of Reasons for Metal-Organic Framework’s Antibacterial Activities,” *Polyhedron*, vol. 156, pp. 257-278, Dec. 2018.
- [99] J. H. Jo, H. C. Kim, S. Huh, Y. Kim, and D. N. Lee, “Antibacterial Activities of Cu-MOFs Containing Glutarates and Bipyridyl Ligands,” *Dalt. Trans.*, vol. 48, no. 23, pp. 8084-8093, 2019.